

NUCLEAR REACTIONS WITH HEAVY ION BEAMS

Martin Veselský¹*Institute of Physics, Slovak Academy of Sciences, Dúbravská cesta 9, Bratislava, Slovakia*

Received 31 October 2013, accepted 6 November 2013, in final form 18 November 2013

An introduction into the study of nucleus-nucleus collisions is presented, along with an overview of present status of selected topics. The study of nucleus-nucleus collisions is a diverse field, allowing to address a wide range of fundamental physics. In each domain of beam energies, from the Coulomb barrier to ultrarelativistic energies, characteristic reaction mechanisms contribute and offer possibility to obtain information on the properties of nuclear matter under specific conditions, what allows to determine a global equation of the state and construct a global phase diagram of the strongly interacting nuclear matter. The extracted properties of the nuclear matter can be used for development of theoretical description of the nuclear matter and the underlying theory of the strong interaction, the quantum chromodynamics. The properties of the nuclear matter further allow to make conclusions on various aspects of the nuclear astrophysics and astro-particle physics, from the primordial nucleosynthesis through production of heavy nuclei, properties of neutron stars, supernova explosions, to the physics of the early Universe. The nucleus-nucleus collisions can be also used as a practical tool for production of very exotic neutron-rich nuclei, thus allowing to enter this yet completely unknown domain with the potential for further discoveries of new nuclear phenomena. Further progress in the field will depend on availability of the new experimental facilities with the capabilities greatly exceeding the capabilities of the presently existing experimental facilities.

DOI: 10.2478/apsrt-2013-0001

PACS: 24.10.-i, 24.10.Pa, 25.70.-z, 25.70.Gh

KEYWORDS: Nucleus-nucleus collisions, Heavy-ion beams, Exotic nuclei, Super-heavy nuclei, Complete fusion reactions, Nucleon exchange, Multifragmentation, Liquid-gas phase transition, Nuclear equation of state, Symmetry energy.

¹E-mail address: Martin.Veselsky@savba.sk

Contents

1	Introduction	3
2	Nuclear reactions	5
2.1	Nuclear reactions at low energies close to Coulomb barrier	6
2.2	Nuclear reactions at intermediate energies	14
2.3	Nuclear reactions at relativistic and ultra-relativistic energies	38
3	Production of exotic nuclei	44
3.1	Production of proton-rich nuclei	45
3.2	Production of neutron-rich nuclei	47
3.3	Production of super-heavy nuclei	56
4	Nuclear equation of state	63
4.1	Nuclear matter	63
4.2	Hot nuclei and multifragmentation	64
4.3	Liquid-gas phase transition	69
4.4	Symmetry energy	76
4.5	Quark deconfinement phase transition	89
4.6	Implications for nuclear astrophysics	92
5	Conclusions	96
	References	97

1 Introduction

Since the first nuclear reaction was observed almost a century ago [1], study of nuclear reactions lead to several fundamental discoveries, such as discovery of neutron, discovery of nuclear fission, production of a wide range of chemical elements up to the superheavy nuclei, production of sub-nuclear (elementary) particles, and production of a new state of matter, quark-gluon plasma. Moreover, a practical use of nuclear reactions influenced the daily life of human society through a wide range of applications, most prominently in production of energy and in medicine. Specific role belongs to the nuclear reactions, induced by the beams of heavy ions on heavy target nuclei, named also nucleus-nucleus collisions. The term heavy means usually any nucleus with mass A equal or larger than 20 mass units ($A \geq 20$). Such a distinction is not arbitrary, the lighter nuclei like ^{12}C exhibit a strong cluster structure and only nuclei with 20 or more nucleons can be considered as the homogeneous objects, which can be described using many-body techniques. Since accelerated heavy ion beams carry electrically charged nucleus, much smaller than radius of atomic orbitals, where electrons are normally located, the probability of non-elastic nuclear interaction (nuclear reaction) with a nucleus of a target material is dramatically limited at low beam energies by the presence of the Coulomb barrier, originating from the repulsive electrostatic interaction of the beam and target nucleus. Once the beam energy exceeds the Coulomb barrier, many additional reaction channels open up energetically and a variety of open channels evolves with increasing beam energy.

The basic requirement for the occurrence of nucleus-nucleus collision, kinetic energy of the beam of accelerated heavy ions exceeding the corresponding Coulomb barrier, implies that multiply charged heavy ions must be accelerated and thus a powerful accelerator, equipped with an ion source, capable to provide such ions with multiple electrons stripped from their atomic envelope, must be available. The cyclic accelerators, named cyclotrons, which met such requirements, became available in the late 50-s and early 60-s in the Lawrence Berkeley National Laboratory in Berkeley, California, USA, in the Nobel Institute of Physics, Stockholm, Sweden and in the Flerov Laboratory of Nuclear Physics, Dubna, Soviet Union, and they became a driving force of the new dynamically evolving field of nuclear physics. Instantaneous impact of the new accelerating technique was achieved by producing heavy chemical elements beyond mendelevium in the complete fusion reactions (for a review see e.g. [2]). In the next decades, compound nucleus (complete fusion) reactions close to the Coulomb barrier became a tool of choice for production of extremely proton-rich nuclei up to the limit of stability against instantaneous emission of protons, the so-called proton dripline. Further increase in the beam energy lead to observation of a new, previously unknown type of nuclear reactions, the reactions of deep-inelastic transfer [3] (which use to be called also deep-inelastic collisions, however this term is used also in particle physics for description of a different phenomenon, and thus it is advisable to avoid such redundancy). With increasing beam energy, reactions induced by heavy ion beams lead to observation of various fragmentation phenomena, and provided a possibility to probe the nuclear equation of state at sub-saturation density, where the liquid-gas phase transition, analogous to the phase transition in water, can be addressed. Further increase of beam energy lead to observation of the flow phenomena [4], manifesting the properties of the equation of state of nuclear matter at supra-saturation nuclear densities. Use of such heavy ion beams of relativistic energies lead also to observation of sub-threshold emission of sub-nuclear particles, e.g. pions [5], not achievable in reactions induced by nucleons or other particles. At ultra-relativistic energies, nucleus-nucleus

collisions observed at the Super Proton Synchrotron at CERN, Geneva, at the Relativistic Heavy Ion Collider at Brookhaven National Laboratory and at the Large Hadron Collider at CERN, allowed observation of a new state of matter, predicted by the quantum chromodynamics, the quark-gluon plasma. Besides these discoveries, the nucleus-nucleus collisions can be potentially used as a practical tool, offering a large potential for production of extremely neutron-rich nuclei, not achievable by other methods. Such options, however, need further development in order to reach viable experimental solutions. In general, it is beyond doubt that emergence of the heavy ion accelerators opened a wholly new field of nuclear physics, which is evolving dynamically until today.

Further breakthrough in nuclear physics was achieved by development and construction of facilities, providing the beams of short-living unstable nuclei (unstable heavy ions). First beams of unstable nuclei were obtained at the Niels Bohr Institute at Copenhagen by the ISOL (Isotope Separation On-Line) method [6], allowing to extract, by a thermal transport, the unstable nuclei from the thick target, irradiated by high-energy proton beam, and subsequently ionize them and transfer them to the experimental area as secondary beams. Such method, providing low-energy secondary beams, which can not initiate secondary nuclear reactions, is used now e.g. at the ISOLDE facility at CERN and at the TRIUMF facility in Vancouver, Canada, for a wide range of experiments in nuclear spectroscopy and astrophysics. However, a further necessary step, allowing to use the secondary beams of unstable nuclei for initiation of nuclear reactions, is the post-acceleration of the secondary beam. This was first achieved at the ISOL facility at Cyclotron Laboratory in Louvain-la-Neuve. Post-accelerated ISOL beams are nowadays available also at the REX-ISOLDE LINAC at ISOLDE, at Oak Ridge National Laboratory, and at the TRIUMF facility in Vancouver. Reaction mechanism studies with radioactive beams such as ^{132}Sn have been performed primarily at Oak Ridge facility, focusing mainly to the complete fusion reactions [7]. At the REX-ISOLDE, the maximum beam energy of 3 A MeV, still below the Coulomb barrier, is sufficient to initiate some types of reaction, such as Coulomb excitation and direct (d,p)-transfer. The planned upgrade to HIE-ISOLDE will allow post-acceleration to 10 A MeV and thus a study of nuclear reactions. Another possibility to initiate nuclear reactions using the secondary beams is to use the in-flight method, where primary beam with energies above 50 A MeV hits the target and the secondary fragments are separated using suitable ion-optical device, thus forming a secondary beam, even if of a much worse quality than the post-accelerated beam. Examples of such facilities are FRS at GSI Darmstadt, SPIRAL at GANIL Caen, A-1200 and A-1900 at NSCL, Michigan State University, and RIBF facility at RIKEN in Japan. First fragmentation studies of secondary beam were performed at fragment separator FRS at GSI Darmstadt [8]. Also the in-flight method can be used to provide high-quality post-accelerated beams, in that case the secondary fragments need to be stopped in the gas volume, ionized and re-accelerated. Such facilities are under construction now, e.g. at the NSCL and RIKEN. Future large scale facilities, providing intense secondary beams of unstable nuclei, encompass e.g. the FAIR facility at Darmstadt, Germany, FRIB facility at Michigan State University, and ultimately the planned EURISOL facility. Such facilities will allow large-scale use of secondary beams for initiation of secondary reactions, allowing detailed studies of reaction mechanisms and potentially leading to beams of even more exotic nuclei.

2 Nuclear reactions

Studies of radioactive properties of nuclei in the beginning of 20th century led to observation of the first nuclear reaction initiated by human activity. In 1919 Rutherford observed reactions [1] where alpha-particles from the radioactive source interacted with the stable isotope of nitrogen ^{14}N , resulting in emission of proton and production of unstable nucleus ^{17}O . Nuclear reactions, initiated by alpha-particles, remained the only known type of experimentally observed nuclear reaction until 1932, when Chadwick discovered neutron [9] and Cockcroft and Walton developed first particle accelerator, accelerating protons [10]. Initially, the most frequently used type of reactions, initiated by the beams of heavy ions was the compound nucleus reaction, where statistically equilibrated compound nucleus is formed by fusion of the beam and target nuclei (as explained by Niels Bohr [11]), and the excess of energy is disposed by emission of light particles (mostly neutrons) and γ -rays. In 1934 Fermi reported observation a new type of reaction, induced by neutrons on uranium, and observed new unstable nuclei, which he assigned as transuranium elements [12]. Only in 1939 detailed chemical analysis, performed by Hahn and Strassman, established that the observed activity belongs, among others, to the element of barium in the middle of periodic table [13]. Such observation was explained by Meitner and Frisch [14] as a process of nuclear fission, a first nuclear process where a wide range of unstable nuclei was produced. Another type of nuclear reactions observed in this early era of nuclear physics were the direct reactions, where the reaction such as (d,p)-transfer occurs in single step, as first described in 1935 by Oppenheimer and Phillips [15].

As described above, significant impulse to investigation of nuclear reactions was provided by the use of heavy ion beams, which allowed study of the nucleus-nucleus collisions. While the nuclear reactions, induced by the beams of nucleons or light nuclei such as α -particle, occur at limited range of angular momenta, in the nucleus-nucleus collisions a wide range of angular momenta contributes. Therefore, a limiting value of angular momentum, called grazing angular momentum, must be defined, which corresponds to the collision, where two nuclei barely touch ("graze") each other. The corresponding scattering angle is called grazing angle. Grazing angular momentum can be simply estimated as

$$l_{graz} = k R \sqrt{\frac{E_{cm} - V_{int}(R, l = 0)}{E_{cm}}} \quad (2.1)$$

where k is the norm of the wave vector, $R = R_1 + R_2$ is the interaction radius, where R_1, R_2 are radii of the two nuclei, E_{cm} is the kinetic energy in the center of mass system and $V_{int}(R, l = 0)$ is the height of the interaction barrier. At the angular momenta larger than grazing angular momentum, or correspondingly, at impact parameters larger than the value $b_{graz} = \hbar l_{graz} / p_{cm}$ (where \hbar is the Planck constant, representing the quantum of angular momentum, and p_{cm} is the momentum in the center of mass system), corresponding to touching configuration, elastic scattering is a dominant scenario. Nevertheless, due to extension and thus possible overlap of nucleonic wave function, direct nucleon stripping or pickup reactions are possible even at angular momenta, larger than grazing angular momentum. Other possible inelastic channel, occurring above the grazing angular momentum, is the Coulomb excitation, mediated purely by electromagnetic interaction.

When the initial angular momentum becomes smaller than the grazing angular momentum,

the short-range nuclear interaction turns on and a variety of reaction scenarios becomes possible, depending on the value of angular momentum and on the kinetic energy of relative motion. Several energy regimes are defined in this article and treated in detail separately. The emphasis is put on the properties of the massive reaction products, as survivors of the dynamical evolution during nucleus-nucleus collision. The collisions can be classified by the number of massive remnants as fusion-like collisions (with a single massive remnant), binary collisions (with the projectile- and target-like remnant) and multifragmentation (with many massive remnants). Still, the number of such massive remnants can be influenced by secondary emission from these fragments, and thus also their dynamical properties need to be considered prior to making conclusions concerning the type of collision. As documented below, the definitions of energy domains used here coincide with changes in the typical number of massive fragments, thus reflecting the change of reaction mechanism.

Besides classification by beam energy, the nucleus-nucleus collisions can be usually split into several classes according to their impact parameter (or angular momentum). Especially at low and intermediate energies the peripheral and central collision represent separate classes with different dominant reaction mechanism. Therefore, also the model description differs and it is mostly phenomenological.

Of course, an ultimate goal is to have universal model, able to describe any class of collisions, for now this was achieved with most success at relativistic beam energies. On the other hand, phenomenological models are valuable by their simplicity and allow to think about the reaction mechanism in relatively simple terms, which may be helpful for the readers previously not familiar with the field.

2.1 Nuclear reactions at low energies close to Coulomb barrier

The longest known type of nuclear reaction at low energies close to Coulomb barrier is the compound nucleus or complete fusion reaction [11]. In order for complete fusion reaction to occur in nucleus-nucleus collision, the two nuclei need to overcome the interaction barrier. When the kinetic energy of the heavy ion beam is comparable to the fusion barrier, the probability of fusion depends on the properties of the fusion barrier. The fusion barrier is formed by an interplay of repulsive Coulomb interaction and attractive nuclear interaction. A successful parameterization of nucleus-nucleus potential was formulated using the so-called nuclear proximity potential [16]

$$V_{int}(r, l) = \frac{Z_1 Z_2 e^2}{r} + \frac{\hbar l^2}{2\mathcal{J}} - a_s d \frac{A_1^{1/3} A_2^{1/3}}{R_1 + R_2} e^{-s/d} \quad (2.2)$$

where a_s is the surface energy coefficient, Z_1, Z_2 are the atomic numbers of nuclei, A_1, A_2 are the mass numbers of nuclei, l is the angular momentum, and \mathcal{J} is the momentum of inertia of the system. Such formula obviously leads to the values of the fusion barrier height lower than the pure Coulomb plus centrifugal barrier. The fusion cross section can be then calculated as a sum of contributions of partial l-waves up to some limiting value of angular momentum l_{lim}

$$\sigma_{fus} = \sum_{l=0}^{l_{lim}} (2l+1) T_l \quad (2.3)$$

where the transition probability T_l can be estimated assuming parabolic barrier

$$T_l = \frac{1}{1 + \exp[2\pi(V_{int}(l) - E_{cm})/\hbar\omega_l]} \quad (2.4)$$

with $V_{int}(l)$ being the maximum of $V_{int}(r, l)$ for a given l and $\hbar\omega_l$ being the barrier curvature parameter. Alternatively, the transition probability T_l can be evaluated using the WKB approximation [17] for any shape of fusion barrier. As a reasonable parameterization for evaluation of fusion probabilities in reactions, leading to compound nuclei up to $Z = 104$ at energies in the vicinity of fusion barrier can be assumed the WKB approximation with the barrier diffuseness, used in the statistical code HIVAP [18]. The value of the limiting angular momentum is usually estimated using the formula of Wilczynski [19].

For nuclei with $Z > 104$ and also for some symmetric fusion reactions leading to neutron-deficient isotopes of thorium and uranium [20], additional fusion hindrance due to competition with fast fission mode (quasi-fission) needs to be considered. Also, for detailed description of the sub-barrier fusion phenomena the coupled-channel fusion model [21], reflecting the coupling of fusion process to presence of suitable excited nuclear levels, can be used. Furthermore, below fusion barrier, some direct reactions are possible, mostly a pickup or stripping of a nucleon. Sub-barrier phenomena, despite their low cross sections, are of high importance especially for nuclear astrophysics. These phenomena are beyond the scope of the present article and interested readers can find detailed introduction e.g. in the review [22].

Once the fusion cross section is known, the final cross sections of individual reaction channels (represented by a specific evaporation residue) can be calculated using the statistical model of nuclear deexcitation, as implemented e.g. in the statistical code HIVAP [18]. This code is widely used for the calculations of evaporation residue (ER) cross sections in the region of heavy fissile nuclei at the excitation energies up to 100 MeV. It is based on the statistical model of compound nucleus deexcitation. The production cross section of a given evaporation residue is given as

$$\sigma_{ER} = \sum_{l=0}^{l_{lim}} (2l+1) T_l P_{ER}(l) \quad (2.5)$$

where the survival probability $P_{ER}(l)$ is given as

$$P_{ER}(l) = \sum_c \prod_{k=1}^{N_{ER}} P_i^{(k)}(l_i) \quad (2.6)$$

where the first sum includes any possible emission sequence c (e.g in the channel with emission of a single of proton and several neutrons the proton can be emitted at any stage of de-excitation cascade). The probability of a given decay channel i is

$$P_i(l) = \Gamma_i(l)/\Gamma_{tot}(l) \quad (2.7)$$

where $\Gamma_i(l)$, $\Gamma_{tot}(l)$ represent the width of a decay channel i and the total decay width at a given de-excitation stage. The partial emission widths for particle emission are determined as

$$\Gamma_i(E, l) \propto (2l+1)(2s_i+1) \int_0^{E-E_B(l)-E_{rot}(l)} \rho(E-E_B(l)-E_{rot}(l)-\epsilon)\epsilon\sigma_i d\epsilon \quad (2.8)$$

and the fission width as

$$\Gamma_f(E, l) \propto (2l + 1) \int_0^{E - B_f(l) - E_{rot}(l)} \rho(E - B_f(l) - E_{rot}(l) - \epsilon) d\epsilon \quad (2.9)$$

where ρ is the level density calculated using the Fermi gas formula [23] and σ_i the inverse cross section for particle emission, l again denotes the angular momentum, s_i the spin of the particle, E_B the binding energy of the particle, E_{rot} the rotational energy

$$E_{rot}(l) = \frac{\hbar^2 l(l + 1)}{2\mathcal{J}} \quad (2.10)$$

and $B_f(l)$ the fission barrier. The level density parameter used in the level density formula was determined for the particle emission channel according to the formula of Ignatyuk [24] (with the damping constant $D = 18.5 MeV$ describing the quenching of the ground state pairing correction with increasing excitation energy) while for the fission channel the asymptotic value of level density parameter $\tilde{a} = A/10 MeV$ was used.

The above model of statistical emission was verified in detail using the evaporation residue cross sections in the region from mercury to uranium [25], using the cross sections of xn, pxn and α xn evaporation channels, with long de-excitation chains of up to 13 emitted neutrons. In this region the observed values of the evaporation residue cross sections are still rather high and identification of reaction products is relatively simple since the proton-rich nuclei in this region are α -emitters. Also, since fission barriers in this region are comparable to neutron binding energy, fission channel plays important role and its implementation to the model can be put to stringent test. This region, specifically in the vicinity of the closed neutron shell $N=126$, is important also as a testing ground for the production of superheavy nuclei, where fission barrier are caused purely by the shell structure.

In the framework of statistical model of compound nucleus deexcitation, three modes of calculations were used in order to reproduce large set of production cross sections of nuclei with $Z = 82 - 92$ and $N \simeq 126$, produced in heavy ion induced reactions at projectile energies from Coulomb barrier up to 10 AMeV. Three different modes of calculation were used, introduction in different way the shell effects into the calculation of fission probability.

Within the first variant (I), the full fission barrier was calculated as the sum of liquid drop and shell components

$$B_f(l) = CB_f^{LD}(l) + \Delta B_f^{Shell}. \quad (2.11)$$

where the macroscopic component of fission barrier (B_f^{LD}) was calculated according to the rotating charged liquid drop model of Cohen-Plasil-Swiatecki [26]. Shell component of the fission barrier (ΔB_f^{Shell}) was taken as the difference between liquid drop [27] and measured [28] mass of the nucleus, i.e. as the module of $\Delta W_\nu(A, Z)$. Coefficient C was the only free parameter of calculations. In order to reproduce correctly the full set of data, including pxn and α xn channels, the values of emission barriers were scaled by factor $C_p = 0.91$ for protons and $C_\alpha = 0.82$ for α -particles.

Using this modification, the overall agreement within factor of four in all xn, pxn and α xn channels was achieved. On Figure 2.1 are given optimum values of parameter C , necessary to

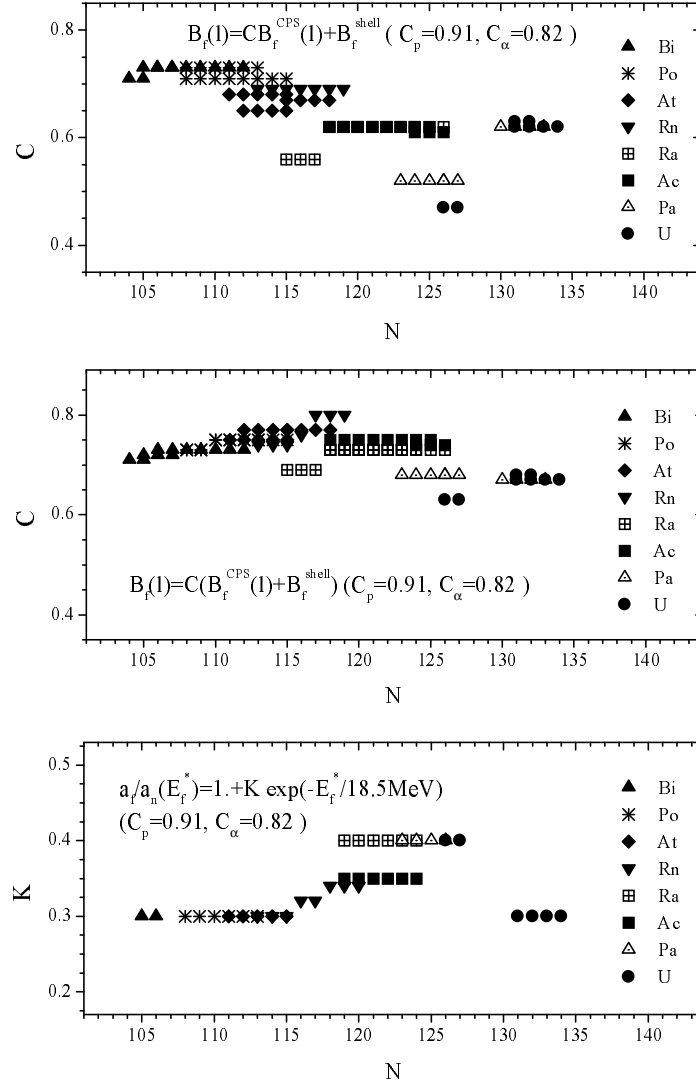


Fig. 2.1. Top panel: Optimum values of parameter C , necessary to reproduce experimental cross sections within Variant I, as a function of neutron number of residual nuclei. Middle panel: Optimum values of parameter C , necessary to reproduce experimental cross sections within Variant II, as a function of neutron number of residual nuclei. Bottom panel: Optimum values of parameter K , necessary to reproduce experimental cross sections within Variant III, as a function of neutron number of residual nuclei.

reproduce experimental cross sections, as a function of neutron number. Strong reduction of optimum C values occur in the vicinity of neutron shell $N = 126$, where C values form resonance

like structure. This may indicate that, within variant (I), the influence of shell effects onto fission channel may be introduced incorrectly, because such a strong dependence of macroscopic quantity on shell structure is hard to explain.

In an alternative variant (II), the whole sum of macroscopic and microscopic (shell) part of fission barrier was scaled by a factor C

$$B_f(l) = C (B_f^{LD}(l) + \Delta B_f^{Shell}) \quad (2.12)$$

and the values of parameters C_p , C_α and $\tilde{a}_f/\tilde{a}_\nu$ were the same as in variant (I).

Obtained overall agreement in production cross sections was of the same quality as in the previous case. On Figure 2.1b are given optimum values of parameter C , necessary to reproduce experimental cross sections, as a function of neutron number within variant (II). Values appear to be practically constant in the vicinity of neutron shell $N = 126$ and far off the shell closure. Few remnants of resonance like structure are still present but do not violate the overall trend. In this way we obtained the set of fixed parameters for the whole set of experimental data. Overall stability of coefficient C , which is the only free parameter of calculations, may point to the role of correct calculation of level density in the saddle point configuration instead of modification of fission barriers.

Taking into account results of previous calculations the last variant (III) was used, where parameter C was fixed (the value $C = 0.9$ was applied to the macroscopic fission barrier of CPS in order to use fission barriers similar to that of Sierk [29]) and the ratio of asymptotic level density parameters in fission and evaporation channels $\tilde{a}_f/\tilde{a}_\nu$ was varied with excitation energy above saddle point according to formula

$$\tilde{a}_f/\tilde{a}_\nu(E_f^*) = 1 + K \exp\left(-\frac{E_f^*}{D}\right) \quad (2.13)$$

where the value of damping parameter D was taken as ($D = 18.5 \text{ MeV}$), equal to the damping constant of shell effects in particle evaporation channels [24]. This formula leads to values of $\tilde{a}_f/\tilde{a}_\nu$ close to one at excitation energies higher than 50 MeV what is in agreement with conclusion of work [30]. The parameter K is the only free parameter of calculation within variant (III).

On the bottom panel of Figure 2.1 are given optimum values of parameter K , necessary to reproduce experimental cross sections within analogous overall agreement as in previous cases, as a function of neutron number. The values differ in the vicinity of neutron shell $N = 126$ and far off the shell. The resonance like structure is evident and is centered around value of about $N = 124$. Such a shift may imply that for determination of production cross sections mainly last few steps of deexcitation cascade are decisive. This conclusion is in agreement with our previous studies for the nuclei with the $Z = 82 - 92$ [31]. Higher value of K near the neutron shell $N = 126$ may imply transition from deformed to spherical nuclei, what leads to reduction of collective enhancement in the level density of particle evaporation remnants and thus to further increase of the dominance of level density in the fission channel.

Thus a large set of production cross sections of nuclei with $Z = 82 - 92$, produced in xn, pxn and α xn channel of heavy ion induced reactions, could be reproduced using three different sets of parameters of statistical model of nuclear deexcitation. Of the three variants, the variant (II) indicates that the fission barrier as a whole is "scaled down", which means that the relative scaling

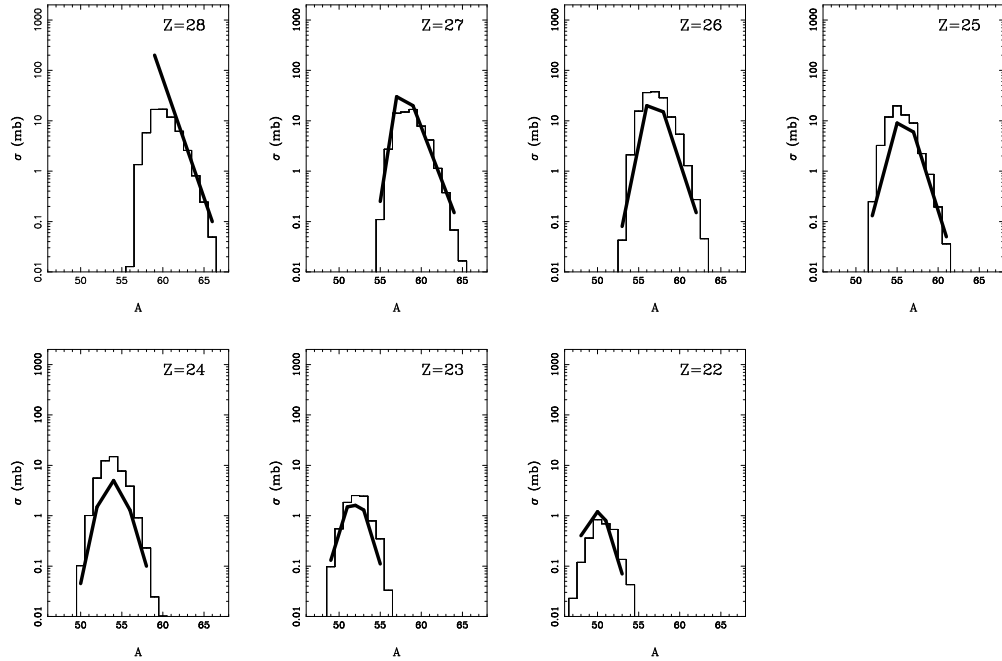


Fig. 2.2. Experimental [32] (thick lines) and simulated (lines) mass distributions in the reaction $^{58}\text{Ni}+^{208}\text{Pb}$ at 5.66 A MeV for selected elements.

of macroscopic and microscopic part of the fission barrier is not the source of discrepancy. On the other hand, the variant (III) appears to point to the decisive role of difference in deformation of saddle point and ground state, and sensitivity to changes in ground state deformation of the excited nuclei.

Besides compound nucleus reactions, where a single composite excited nucleus is formed by fusion of the projectile and target, there is other class of (binary) nuclear reactions, where both projectile- and target-like residue are preserved. Some experimental data for reactions of massive nuclei exist at energies just above the Coulomb barrier, with significant cross sections. An attempt was undertaken [33] to test the model framework, using the model of deep-inelastic transfer (DIT) in the implementation of Tassan-Got [34], combined with de-excitation code SMM [35]. It was established that using the original version of the DIT code, optimized for the beam energies comparable to the Fermi energy of the nuclear matter (which amount to approximately 40 MeV), the production cross sections of multi-nucleon transfer could not be reproduced. It was necessary to modify the parameterization of the nucleon density profile to allow opening of the transfer window at larger separation distances. Using the modified parameters of the trapezoidal density profile (maximum full density radius R_0 was enlarged by 0.7 fm and the slope increased from 0.65 to 2.2 fm), it was possible to reproduce reasonably well the cross sections of the multinucleon transfer in the reaction $^{58}\text{Ni}+^{208}\text{Pb}$ at 5.66 A MeV [32], as documented in the Figure 2.2. The necessary extension of the nuclear density profile can be possibly interpreted

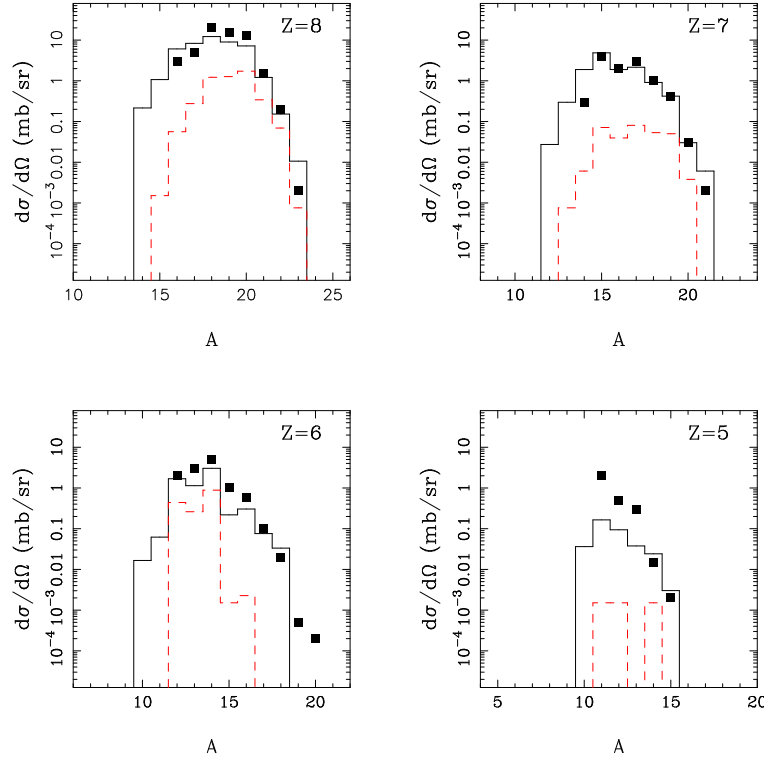


Fig. 2.3. Experimental [38] (symbols) and simulated (lines) mass distributions in the reaction $^{22}\text{Ne}+^{232}\text{Th}$ at 7.9 A MeV for selected elements at 40 degrees. Dashed lines - standard DIT+SMM simulation, solid lines - DIT+SMM using DIT code with the extension of the nuclear profile.

as a mean field effect due to evolution of the low density nuclear matter structure in the window (neck) region in the initial stage of the reaction. This explanation can provide an alternative to the initially suggested enhancement of the di-proton transfer [32]. Another reactions with available experimental data were $^{64}\text{Ni}+^{208}\text{Pb}$ at 5.47 A MeV [36] and $^{64}\text{Ni}+^{238}\text{U}$ at 6.09 A MeV [37] where an analogous simulation was carried out with the same parameters as in the previous case. The result lead to agreement which was analogous to the previous case. It appears that the extension of the nuclear density profile can be an effect caused by long reaction timescale at energies just above the Coulomb barrier and thus its evolution can be determined dominantly by the initial energy of the beam.

In this context it is of interest to investigate data also at somewhat higher initial beam energy. Projectile-like nuclei were observed in the reaction $^{22}\text{Ne}+^{232}\text{Th}$ at beam energy 7.9 A MeV, using two detectors positioned at 12 and 40 degrees [38].

The comparisons of the observed isotopic yields (symbols) at the two angles with the results of a standard DIT+SMM simulation (dashed lines) and of the version using the DIT code with the extension of the nuclear profile (solid lines) are shown in Figures 2.3, 2.4. The extension

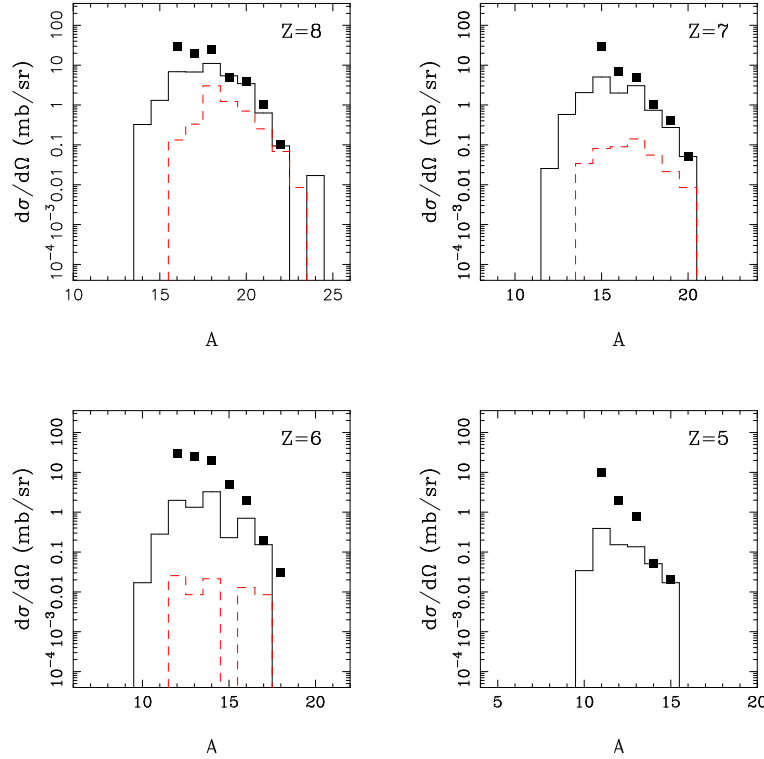


Fig. 2.4. Experimental [38] (symbols) and simulated (lines) mass distributions in the reaction $^{22}\text{Ne}+^{232}\text{Th}$ at 7.9 AMeV for selected elements at 12 degrees. Dashed lines - standard DIT+SMM simulation, solid lines - DIT+SMM using the DIT code with the extension of the nuclear profile.

of the nuclear profile amounted to approximately 75 % compared to the three reactions at beam energy 5.5 – 6.0 AMeV. Again the standard DIT+SMM simulation (dashed lines) underpredicts the magnitude of the observed cross sections and improvement is achieved when using the extended nuclear profile, with the necessary extension weaker by 25% than in reactions at lower beam energy. Thus it appears that there exists a trend where the magnitude of the necessary extension of the nuclear profile decreases with beam energy, possibly due to shorter collision time. Reasonable agreement is reached at 40 degrees, while at 12 degrees there appears a problem to reproduce the production cross sections of mainly β -stable isotopes. This discrepancy may be however caused by another reaction mechanism, possibly a direct breakup in the field of heavy target nucleus, as suggested by the fact that production cross sections of these isotopes do not follow precisely the Q_{gg} systematics [38]. This assumption is supported also by the fact that discrepancies are observed mostly at lower angle and the effect increases with decreasing atomic number.

Projectile-like nuclei were observed also in the more symmetric reaction $^{22}\text{Ne}+^{90}\text{Zr}$ at beam energy 7.9 AMeV, using detector positioned at 12 degrees [39]. The extension of the nuclear

profile in DIT+SMM simulations was again approximately 75 % compared to the three reactions at beam energy 5.5 – 6.0 AMeV. Again the standard DIT+SMM simulation underpredicted the magnitude of some observed cross sections, specifically for isotopes of oxygen and nitrogen. For these nuclei, improvement was achieved when using the extended nuclear profile, with the extension as in the reaction $^{22}\text{Ne}+^{232}\text{Th}$. The evolution of the trend thus seems consistent with the dependence on the beam energy as in the previous cases, in this reaction, however, the effect is pronounced weakly when compared to the reactions with heavy fissile target nuclei, since the difference in the overall quality of agreement between two simulations is not too significant. It appears that the extension of nuclear profile evolves (into the neck region) mostly in reactions where heavy fissile nuclei participate.

For projectile-target combinations leading to composite systems in the region of superheavy nuclei there is another possible reaction mechanism, the so-called quasi-fission. It occurs when neither compound nucleus nor the binary configuration, necessary for nucleon exchange, is formed. Instead, the system evolution turns towards the fission valley, and the system reaches scission point very quickly. The systematics in the reactions with lead target, published in [40], shows that quasi-fission sets on for beams heavier than ^{48}Ca and it vanishes when beam energy exceeds 6 AMeV. In terms of reaction mechanism, quasi-fission is similar to nucleon exchange, however it proceeds while macroscopic shape of the system also evolves along the fission valley. Compared to the fusion-fission, total kinetic energy in quasi-fission is lower and the range of mass asymmetry covers the range from mass asymmetry of projectile-target configuration to the symmetric mass split. Besides its complex dynamical nature, investigation quasi-fission is interesting also since it is a major obstacle for production of super-heavy nuclei.

2.2 Nuclear reactions at intermediate energies

The definition of energy domain, called intermediate energies, usually differs among authors, in this review we consider the beam energies between 10 and 100 AMeV, mostly due to the fact that both reaction mechanisms, common around the Coulomb barrier, and reaction mechanisms, typical for relativistic energies, contribute at these energies. As a result, a large variety of reaction mechanisms has been observed in nucleus-nucleus collisions at intermediate energies, or in other words in the Fermi energy domain (10 - 100 AMeV) depending on the impact parameter, projectile-target asymmetry and the projectile energy. The reaction mechanisms typically observed are [41]:

- peripheral elastic and quasi-elastic (QE) scattering/transfer reactions around the grazing impact parameter.
- deep inelastic transfer (DIT) at semi-peripheral impact parameters with partial overlap of the projectile and target and a significant part of the relative kinetic energy transferred into internal excitation energies of the projectile and target.
- incomplete fusion (ICF) reactions at central impact parameters with a typical participant-spectator scenario. At energies around the Fermi energy the participant zone typically fuses with one of the spectator zones (typically heavier) thus creating a highly excited composite nucleus. At most central impact parameters the complete fusion (CF) can occur.

- pre-equilibrium emission of direct particles, caused by onset of two-body nucleon-nucleon collisions at central and mid-peripheral impact parameters. Pre-equilibrium emission typically precedes the ICF/CF and DIT reactions.

While such a scheme is rather well established, there are still many open questions related to evolution of isospin-asymmetry in nucleus-nucleus collisions in the Fermi energy domain. Especially the studies of isospin degrees of freedom in the nucleus-nucleus collisions in the Fermi energy domain allow to reveal many interesting details of the reaction scenario.

Consistent with the above scheme, peripheral nucleus-nucleus collisions in the Fermi-energy domain can be described theoretically using the model of deep-inelastic transfer in combination with an appropriate model of de-excitation. Deep-inelastic transfer occurs when interaction of the projectile and target leads to formation of di-nuclear configuration which exists long enough to allow intense exchange of nucleons through the "window" formed by interaction of mean-fields in the neck region. Transfer of nucleons leads to gradual dissipation of the kinetic energy of relative motion into internal degrees of freedom such as excitation and angular momentum. After re-separation the hot projectile- and target-like prefragments with approximately equal excitation energy are formed and undergo de-excitation via subsequent particle emission or multifragmentation. The model of deep-inelastic transfer, initially developed by Randrup [42] and implemented as a Monte Carlo code by Tassan-Got [34], is essentially a solution of the Fokker-Planck equation, which is a special case of the Boltzmann equation. Still, many phenomenological assumptions were implemented by the authors of the DIT model in order to achieve its predictive power, and thus it is a phenomenological rather than first-principle model description.

Very good description of experimental data from the peripheral collisions in the Fermi energy domain was obtained [43] using the Monte Carlo implementation of the deepinelastic transfer (DIT) model of Tassan-Got [34], when combined with appropriate de-excitation code. The peripheral nucleus-nucleus collisions were investigated using the fragment data from reactions $^{28}\text{Si}+^{124,112}\text{Sn}$ at projectile energy 50 and 30 AMeV. In order to establish whether the observed fragments originate from statistical decay of hot quasiprojectiles, it was necessary to investigate dynamical properties of the projectile-like source and to determine the production mechanism. The observed fragment data provided full information (with the exception of emitted neutrons) on the decay of thermally equilibrated hot quasi-projectiles with known mass ($A = 20-30$), charge, velocity and excitation energy. Detailed investigation of the reaction mechanism allowed to establish a dominant reaction scenario. Excellent description of the fragment observables was obtained using the model of deep-inelastic transfer (DIT) [34] for the early stage of collisions and the statistical multifragmentation model (SMM) [35] for de-excitation. The model described well the dynamical properties of the reconstructed quasi-projectile such as center of mass velocity, excitation energy (see Fig. 2.5) and isospin-asymmetry (see Fig. 2.6). The fragment observables such as multiplicity, charge distributions and mean values of N/Z for a given charge were also reproduced reasonably well. Thus the data could be considered as well understood in terms of reaction mechanism.

The observation that a wide range of observables is in agreement with the dominant reaction scenario of the deep inelastic transfer followed by statistical multifragmentation allowed to conclude that the assumption of statistical equilibrium is applicable and that thermodynamical observables can be defined for the hot quasi-projectile. The contribution from non-equilibrium processes such as pre-equilibrium emission was shown to be weak. The number of emitted neu-

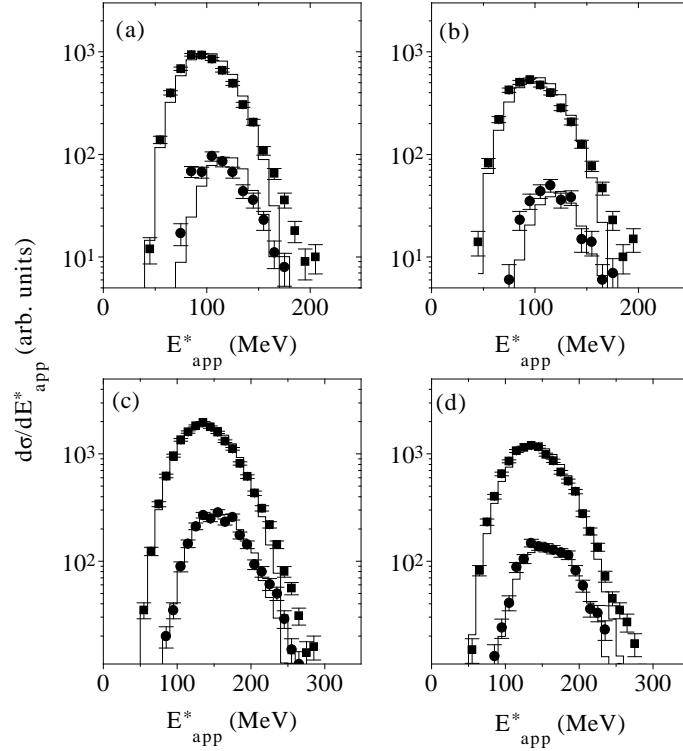


Fig. 2.5. Distributions of the reconstructed apparent excitation energies of the quasiprojectiles [43]. Symbols mean experimental distributions of the set of fully isotopically resolved quasiprojectiles with $Z_{tot} = 14$ (solid circles) and $Z_{tot} = 12 - 15$ (solid squares). Solid histograms mean simulated distributions for corresponding data sets, (a) - $^{28}\text{Si}(30 \text{ AMeV})+^{112}\text{Sn}$, (b) - $^{28}\text{Si}(30 \text{ AMeV})+^{124}\text{Sn}$, (c) - $^{28}\text{Si}(50 \text{ AMeV})+^{112}\text{Sn}$, (d) - $^{28}\text{Si}(50 \text{ AMeV})+^{124}\text{Sn}$.

trons, which are not detected, was, according to successful DIT+SMM simulation, between one and two per event (0.9 and 1.2 for ^{112}Sn and ^{124}Sn at 30 AMeV and 1.4 and 1.7 at 50 AMeV, respectively). As will be demonstrated later, the observed quasi-projectile multifragmentation data offered a good opportunity for investigation of thermodynamical properties of the multifragmentation source and of the possible phase transition.

Peripheral collisions in the nearly symmetric system in the Fermi energy domain were investigated in detail in the reaction $^{86}\text{Kr}+^{64}\text{Ni}$ at 25 AMeV [44] using the recoil separator MARS [45] centered around 0° . An enhancement of the yields of neutron-rich nuclei over the prediction of simulations (PE+DIT/ICF+SMM) [41] and EPAX [46] systematics for fragmentation cross sections was observed and the shapes of the velocity spectra suggested a process with a short timescale such as very peripheral collisions where the details of neutron and proton density profiles at the projectile and target surfaces can play a significant role. Such excessive yields of neutron-rich nuclei can be caused by the neutron-rich surface of the target nucleus, which in

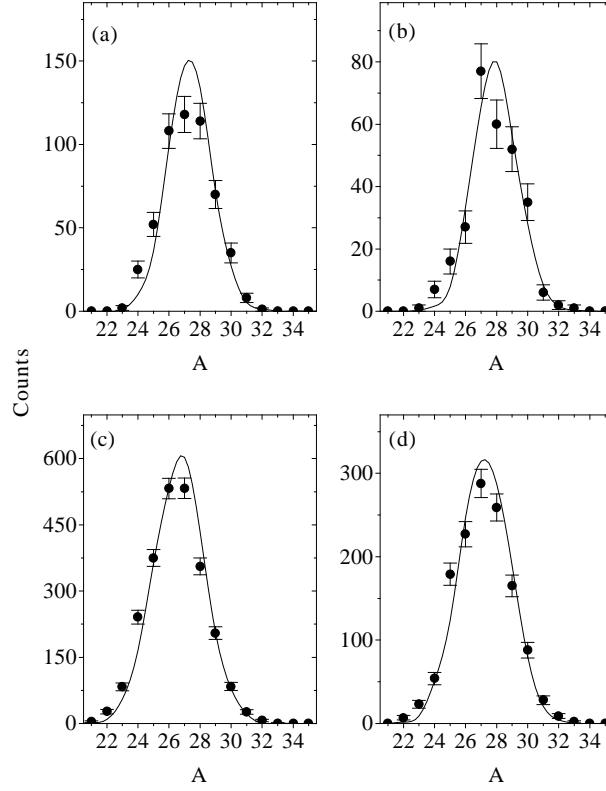


Fig. 2.6. Experimental (solid circles) and simulated (solid lines) mass distributions for the fully isotopically resolved quasiprojectiles with $Z_{tot} = 14$ [43], (a) $^{28}\text{Si}(30\text{AMeV}) + ^{112}\text{Sn}$, (b) $^{28}\text{Si}(30\text{AMeV}) + ^{124}\text{Sn}$, (c) $^{28}\text{Si}(50\text{AMeV}) + ^{112}\text{Sn}$, (d) $^{28}\text{Si}(50\text{AMeV}) + ^{124}\text{Sn}$.

peripheral collisions can lead to stronger flow of neutrons from the target to the projectile (or flow of protons in the opposite direction), thus reverting the flow toward isospin equilibration. In the work [47], the DIT model of Tassan-Got [34] was supplemented with a phenomenological correction introducing the effect of shell structure on the nuclear periphery.

Based on expected linear correlation of the difference of neutron and proton radii $R_n - R_p$ with difference of neutron and proton chemical potentials $\mu_n - \mu_p$, in particular considering the possibility to estimate the surface properties of real nuclei using the estimate of $\mu_n - \mu_p$ by the opposite of the difference of neutron and proton separation energies $-(S_n - S_p)$, a minor modification in the DIT code of Tassan-Got [34] was made by scaling the transfer probabilities by the exponential factors

$$\begin{aligned}
 P_n(P \rightarrow T) &\longrightarrow e^{-0.5\kappa(\delta S_{nP} - \delta S_{pP} - \delta S_{nT} + \delta S_{pT})} P_n(P \rightarrow T) \\
 P_p(P \rightarrow T) &\longrightarrow e^{0.5\kappa(\delta S_{nP} - \delta S_{pP} - \delta S_{nT} + \delta S_{pT})} P_p(P \rightarrow T)
 \end{aligned}$$

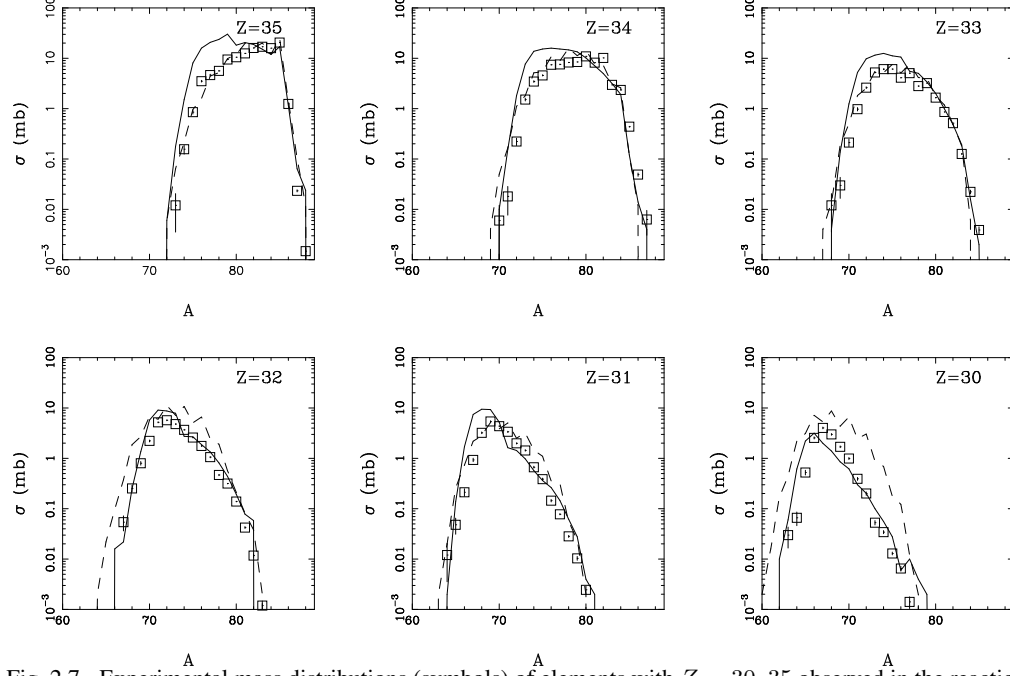


Fig. 2.7. Experimental mass distributions (symbols) of elements with $Z = 30-35$ observed in the reaction $^{86}\text{Kr} + ^{64}\text{Ni}$ at 25 AMeV [44] for angular acceptance centered around 0° , compared to the results of the PE+DIT/ICF simulation with modified DIT calculations combined with the de-excitation codes SMM and GEMINI (solid and dashed line, respectively).

$$\begin{aligned}
 P_n(T \rightarrow P) &\longrightarrow e^{-0.5\kappa(\delta S_{nT} - \delta S_{pT} - \delta S_{nP} + \delta S_{pP})} P_n(T \rightarrow P) \\
 P_p(T \rightarrow P) &\longrightarrow e^{0.5\kappa(\delta S_{nT} - \delta S_{pT} - \delta S_{nP} + \delta S_{pP})} P_p(T \rightarrow P)
 \end{aligned}
 \tag{2.14}$$

where κ is a free parameter and δS_{nP} , δS_{pP} , δS_{nT} , δS_{pT} represent the differences of separation energies calculated using the experimental [48] and liquid-drop [49] masses for the neutrons and protons in the projectile and target, respectively, thus expressing the effect of the microscopic structure. The smooth part is subtracted from the experimental values due to the fact that the macroscopic values of $\mu_n - \mu_p$ follow the bulk N/Z-ratios of reaction partners and the bulk N/Z equilibration is described consistently by the DIT code of Tassan-Got. Thus, the macroscopic concepts used in DIT model are supplemented with phenomenological information on shell structure at the nuclear periphery which can explain the deviation of nucleon exchange from the path toward isospin equilibration, and the model framework assumes the micro-macroscopic structure. The modified DIT calculation was used only for non-overlapping projectile-target configurations, consistent with the assumption that it represents an effect of nuclear periphery. A cut-off was set at separation representing touching half-density surfaces below which a standard DIT calculation, following the path toward isospin equilibration, was used. In Fig. 2.7 we

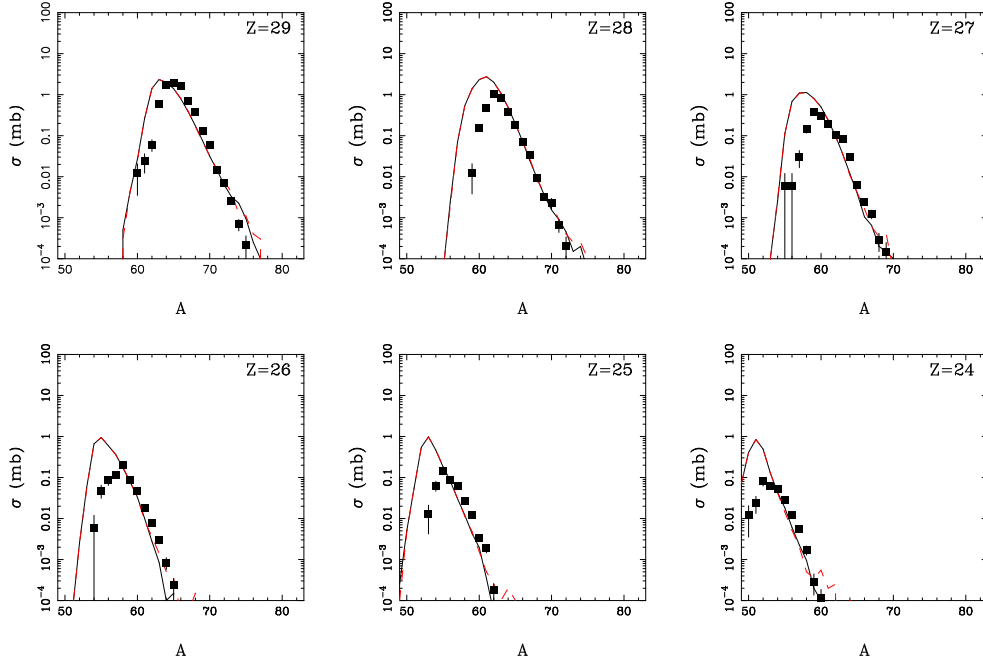


Fig. 2.8. Experimental (symbols) and simulated (lines) mass distributions of elements with $Z = 29 - 24$ observed in the reaction $^{86}\text{Kr}+^{64}\text{Ni}$ at 25 AMeV within the separator acceptance centered around 0° .

present the experimental mass distributions of elements with $Z = 30-35$ observed within the separator acceptance in the reaction $^{86}\text{Kr}+^{64}\text{Ni}$ at 25 AMeV [44] compared to the simulation with the modified DIT calculations, combined with the two de-excitation codes SMM [35] (full line) and GEMINI (dashed line) [50]. The simulated yields were filtered for angular acceptance of the spectrometer MARS. Several calculations were performed with different values of κ and the value of $\kappa = 0.53$, used in the modified DIT calculations presented in Fig. 2.7, was obtained as an optimum value reproducing the experimental mass distributions when using both de-excitation codes, specifically for neutron-rich nuclei with $Z = 35-32$. Otherwise, the GEMINI calculation results in the nearly symmetric mass distributions which appear to overestimate the widths of mass distributions of lighter elements. The SMM calculation appears to reproduce well the yields of neutron-rich nuclei also for lighter elements, on the other hand the yields of β -stable isotopes appear to be overestimated.

In Fig. 2.8 is shown a comparison of experimental and simulated mass distributions of elements with $Z = 29-24$ observed within the separator acceptance centered around 0° in the reaction $^{86}\text{Kr}+^{64}\text{Ni}$ at 25 AMeV [44]. For these products, originating predominantly from more violent collisions, incomplete fusion appears as dominant reaction mechanism. For the reaction $^{86}\text{Kr}+^{64}\text{Ni}$ at 25 AMeV, data were obtained also for angular acceptance centered around 4° . Using the same simulation as in the previous figures, and using appropriate angular cuts reflecting both radial and azimuthal coverage, the results are shown for $Z = 29-24$ in Figure 2.9. Also

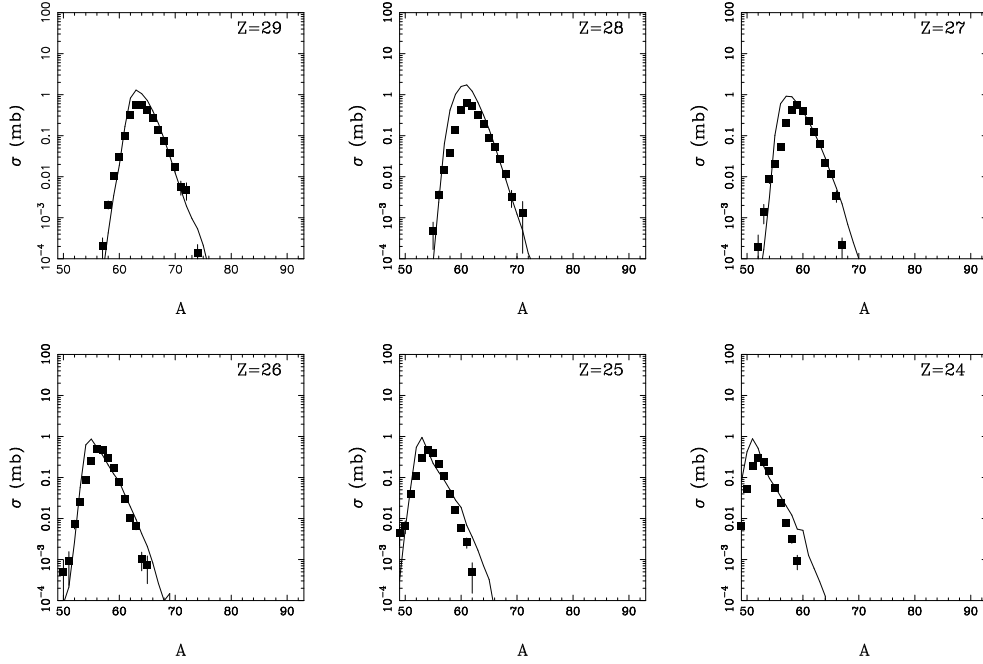


Fig. 2.9. Experimental (symbols) and simulated (lines) mass distributions of elements with $Z = 29-24$ observed in the reaction $^{86}\text{Kr}+^{64}\text{Ni}$ at 25 AMeV within the separator acceptance centered around 4° .

in this case the experimental data and simulation agree reasonably, thus the simulation appears to describe the production cross sections also at angles away from zero. The agreement with simulation was good also for experimental mass distributions in the reaction $^{86}\text{Kr}+^{124}\text{Sn}$ at 25 AMeV, observed at 4 degrees, [51], compared to the results of the PE+DIT/ICF simulation with the modified DIT model (as in the case of $^{86}\text{Kr}+^{64}\text{Ni}$ at 25 AMeV) combined with the SMM (full line). Thus the modified simulation describes consistently the whole set of experimental data, obtained at the beam energy 25 AMeV.

Figure 2.10 shows the results for the reaction $^{86}\text{Kr}+^{64}\text{Ni}$ at 15 AMeV, again at 4 degree setting. The experimental cross sections of products with $Z = 29-24$ [52] seem to be reproduced reasonably well. Figure 2.11 shows the comparison of the calculated total isotopic yields for the reaction $^{86}\text{Kr}+^{64}\text{Ni}$ at beam energies 15 and 25 AMeV. It can be seen that the production cross sections do not drop during transition from 25 to 15 AMeV, the shapes of mass distributions remain similar, with some possible excess of neutron-rich nuclei appearing at 15 AMeV, representing a component produced mostly at higher angles, which thus needs verification in corresponding measurement since the present measurement does not provide decisive answer. Similar level of agreement between experiment mass distributions and the result of the PE+DIT/ICF+SMM calculation as in the reaction $^{86}\text{Kr}+^{64}\text{Ni}$ at beam energies 15 AMeV at 4 degree setting was observed also in the reactions $^{40}\text{Ar}+^{27}\text{Al}$ and $^{40}\text{Ar}+^{64}\text{Ni}$ at the same beam energy and angular setting.

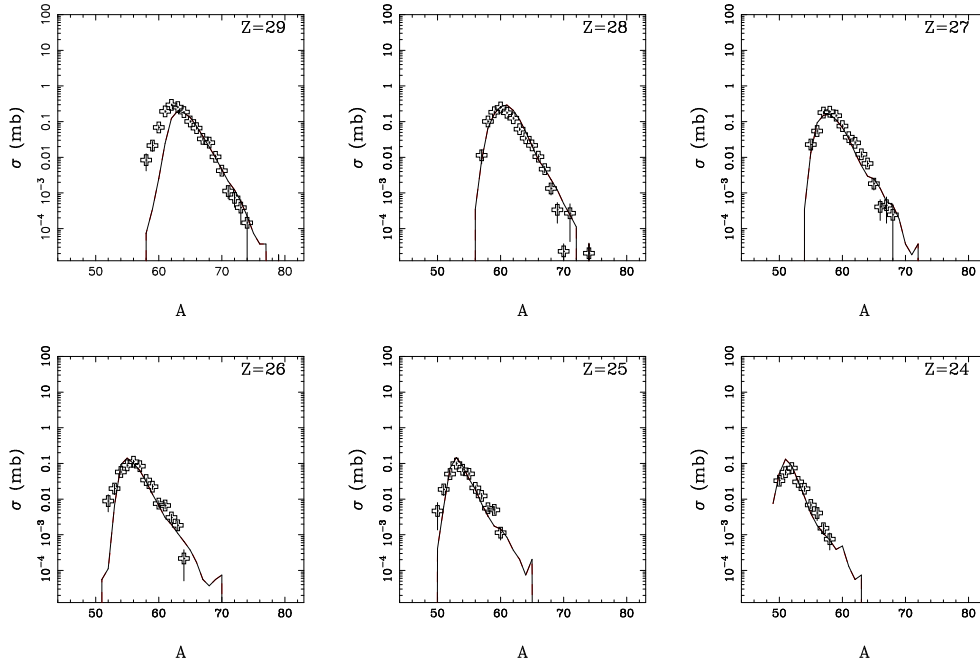


Fig. 2.10. Mass yield curves from the reaction $^{86}\text{Kr}+^{64}\text{Ni}$ at 15 AMeV at 4 degrees. Symbols - measured data. Lines - result of the PE+DIT/ICF+SMM calculation, filtered by the spectrometer angular and azimuthal acceptance.

Thus the reaction mechanism in peripheral collisions at the intermediate beam energies appears to be understood for reactions in both normal and inverse kinematics and its description is provided by the model of deep-inelastic transfer. Since this model assumes that the di-nuclear configuration, which allows intense nucleon exchange, is stabilized for necessarily long time by the balance of the attractive nuclear proximity force and repulsive Coulomb and centrifugal force, it is expected to break down in the more violent collisions, where at larger overlaps the repulsive force becomes dominant over proximity force and no stable di-nuclear configuration can be created. However, in such collision either parts of or the complete projectile and target nuclei can melt together and form hot nucleus. The physical picture employed in the calculations of more central (violent) nucleus-nucleus collisions [41] is depicted in Fig. 2.12. The Monte Carlo model considers several stages of the collision. Different stages of the collision are treated separately. First, pre-equilibrium particle emission takes place. Later, the intermediate projectile-target system is reconstructed and the participant and spectator zones are determined. Finally, an incomplete fusion channel is chosen via interaction of spectators with the participant zone.

The pre-equilibrium emission (PE) is a process where fast particles are emitted prior to the equilibration of the system. The emission of fast pre-equilibrium particles in the reactions induced by nucleons and light particles was theoretically explained using the exciton model [53].

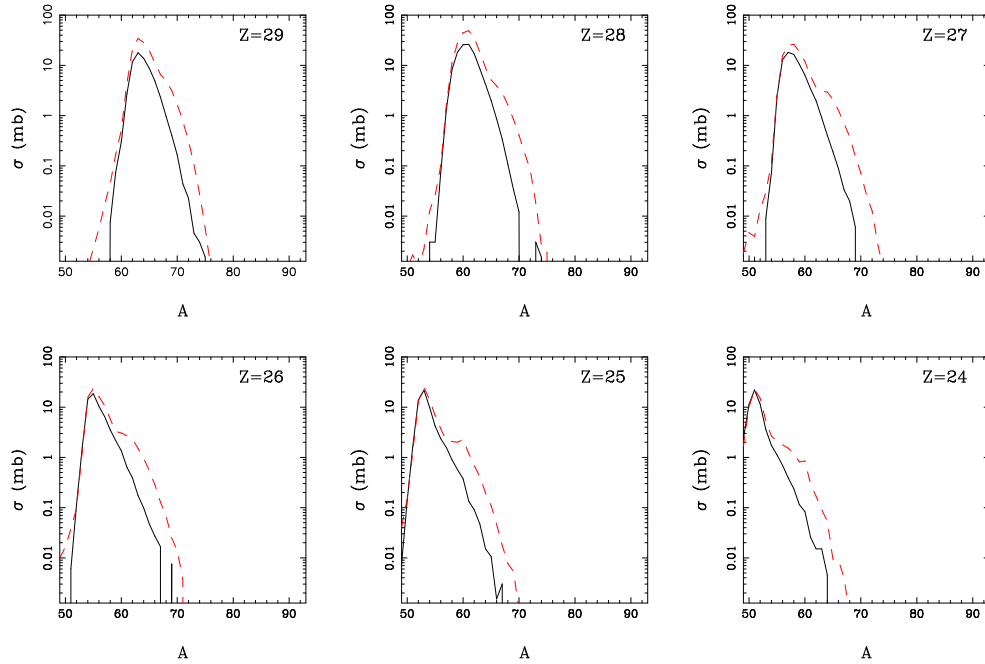


Fig. 2.11. Calculated total mass yield curves from the reaction $^{86}\text{Kr}+^{64}\text{Ni}$ at 25 (solid lines) and 15 AMeV (dashed lines).

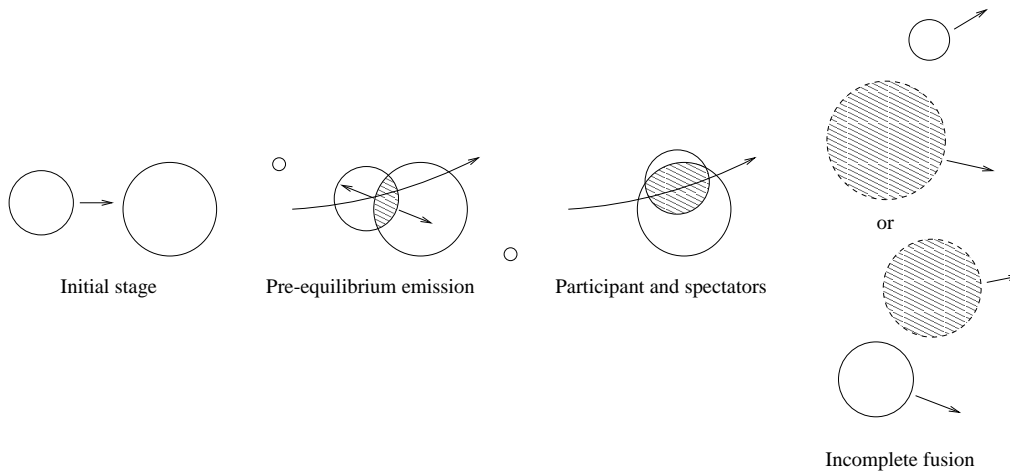


Fig. 2.12. Schematic description of the physical picture employed in the model calculation for violent collisions. Shaded areas mean overlapping and later hot regions.

For reactions induced by heavy-ion beams a model of nucleon exchange was developed [54]. In the works [55, 41], simple phenomenological description based on similar assumptions as the exciton model was introduced. The probability of pre-equilibrium emission for a given reaction stage is evaluated using the formula

$$P_{pre}(n/n_{eq}) = 1 - \exp \left[-\frac{(n/n_{eq} - 1)^2}{2\sigma^2} \right] \quad (2.15)$$

for $n \leq n_{eq}$ and equals zero for $n > n_{eq}$, where n is the number of excitons at a given stage and n_{eq} is the the expected number of excitons in the fully equilibrated compound system (consisting of both projectile and target) for a given excitation energy. The basic assumption leading to equation (2.15) is that P_{pre} depends exclusively on the ratio n/n_{eq} . The parameter σ is a free parameter of the calculation and no dependence on excitation energy is assumed. An initial exciton number is equal to the mass number of the projectile nucleus. The equilibrium number of excitons in the fully equilibrated compound system is calculated according to the formula [56]

$$n_{eq} = 2 g T \ln 2 \quad (2.16)$$

where g is the single particle level density at the Fermi energy and T is the nuclear temperature determined as $T^2 = U/\tilde{a}$, where \tilde{a} is the level density parameter and U is the excitation energy. At each emission step, a random number between zero and one is generated. If the random number is smaller than P_{pre} a pre-equilibrium particle is emitted. If no pre-equilibrium emission occurs at a given emission stage, the pre-equilibrium stage is finished. The properties of emitted pre-equilibrium particles are determined for every emission. The type of particle emitted is determined randomly using the Hauser-Feshbach emission widths for neutron, proton and α -particle. A Maxwellian spectrum of kinetic energy with an apparent temperature [57, 58]

$$T_{app} = \sqrt{\frac{2.5}{A_P} (E_P - V_C)} \quad (2.17)$$

is assumed, where A_P is the projectile mass number, E_P is the projectile energy and V_C is the Coulomb barrier of projectile and target. The apparent temperature corresponds to the excitation energy of the fireball formed by the projectile nucleus together with another A_P nucleons from the target nucleus. This model describes successfully experimental systematics of measured apparent temperatures as shown in refs [57, 58]. Particles are emitted isotropically from the fireball frame moving at half the projectile velocity. After emission, the exciton number is increased by a value

$$\Delta n = A_{pre} \frac{\kappa}{\beta_{0r}(l)} \quad (2.18)$$

where A_{pre} is the mass of emitted particle, $\beta_{0r}(l)$ is the radial velocity in the contact configuration at a given angular momentum and κ is a free parameter. Since pre-equilibrium emission is assumed to occur prior to the fragmentation stage, it is necessary to reconstruct the post-pre-equilibrium projectile-target configuration. The conclusions of the work [54] imply that in the asymmetric reactions with light projectile and heavy target the pre-equilibrium particles are

mostly emitted from the projectile and propagate through the target. Furthermore, it is assumed that the net mass loss caused by emission of pre-equilibrium particles is inversely proportional to the mass of the projectile and target. Total excitation energy of the projectile and target after the pre-equilibrium stage is approximated so that a random walk in excitation energy starts after the first two emissions. The excitation energy of the projectile and target is proportional to their masses.

Several geometrical models of fragmentation have been proposed before where projectile and target are supposed to follow a straight trajectory determined by an impact parameter [59, 60]. Other works assume a classical Coulomb trajectory up to the closest approach configuration and only later the nuclei are supposed to follow a straight line [61, 62]. In the Fermi energy domain, where angular momentum plays an important role, the classical Coulomb trajectories are more realistic since conservation of angular momentum is assured. In the violent collisions, where the proximity potential is relatively weak, it is possible to assume a classical Coulomb trajectory of the intermediate projectile-target system without making any additional assumptions. The minimum distance between the intermediate projectile and target is used as a principal parameter of the geometric overlap scenario. As a result, one participant and one or two spectator zones are created in the fragmentation stage. Their masses are determined proportionally to the determined volumes. The charges of the spectators are determined according to the combinatorial probability density [63, 64]

$$P(Z_{iS}) = \frac{\binom{Z_i}{Z_{iS}} \binom{N_i}{N_{iS}}}{\binom{A_i}{A_{iS}}} \quad (2.19)$$

where A_i, Z_i, N_i are the mass number, charge and neutron number of the projectile (target) and A_{iS}, Z_{iS}, N_{iS} are the mass, charge and neutron number of the projectile (target) spectator. The number of neighboring nucleons (A_{NS}) at the interface of the participant and spectator is then determined and the participant zone is captured by a spectator with more neighboring nucleons. The capturing spectator and participant zone form a hot fragment. The remaining spectator zone is much colder. The excitation energy of the cold fragment is determined assuming that the part of the kinetic energy of the relative motion of the cold fragment and participant zone is transferred into the internal heat during the separation via collisions of the spectator and participant nucleons along the separation plane. The formula for excitation energy reads

$$E_S^* = x A_{NS} \left(\frac{E_P - V_C}{A_P} \right) \frac{\langle s \rangle}{\lambda} \quad (2.20)$$

where E_P and A_P are the kinetic energy and the mass number of the intermediate projectile after pre-equilibrium emission, V_C is the Coulomb barrier between the cold and hot fragment in the contact configuration and $\langle s \rangle = \frac{8\langle r_{seg} \rangle}{3\pi}$ is the mean path of the spectator nucleon within the touching segment of the sphere along the separation plane. For the mean free path λ a value 6 fm is adopted. For each collision half of the asymptotic kinetic energy is converted into heat on average (x is a random number between zero and one). The kinetic energy and the emission angle of the cold fragment are determined randomly using the double differential cross section

formula based on the Serber approximation [65]

$$\frac{d^2\sigma}{dE_a d\Omega_a} = \frac{\sqrt{E_a E_b}}{(2\mu B_P + 2m_a^2 E_P / m_P + 2m_a E_a - 4\sqrt{m_a^3 E_P E_a / m_P} \cos \theta)^2} \quad (2.21)$$

where it is the fragment a which flies away and the fragment b which fuses with the other nucleus, E_a and E_b are their c.m. kinetic energies, B_P is the binding energy of a and b in P , μ is the reduced mass of the system $a + b$, m_P, m_a, m_b are the masses of P, a, b and θ is the emission angle of a with respect to the direction of P in the closest approach.

The hot fragment, produced in the incomplete fusion of one spectator and participant zone, may be very hot and the main mode of de-excitation will be multifragmentation. The most commonly used phase-space model of multifragmentation, the Statistical Model of Multifragmentation (SMM) [35] implements the grand-canonical approximation, the freeze-out volume depends on fragment multiplicity and internal excitation of fragments in the freeze-out configuration is considered, thus producing "hot" fragments.

As an alternative to model of simultaneous multifragmentation, the traditional model of compound nucleus decay based on Hauser-Feshbach approximation [66] was extended to describe the emission of intermediate mass fragments (IMF) [67]. The emission of such complex fragments is described as a binary split, essentially an asymmetric fission where the IMF is accompanied by a heavy residue. The emission probability is determined by a value of the mass-asymmetric fission barrier height. Most common implementations of such model of Sequential Binary Decay (SBD) is the the GEMINI code [50] which has been used extensively for comparisons with experimental multifragmentation data, with reasonable success in description of e.g. inclusive mass and charge distributions. However, as shown below, the model of sequential binary decay fails to describe the results of the exclusive measurements at the zero angle [68] allowing to select a narrow region around the multifragmentation threshold while SMM performs rather well.

Projectile-like products up to the krypton were investigated in another reaction of massive heavy ion beam ^{124}Sn with light target nucleus ^{27}Al at 20 AMeV [68] with the recoil separator MARS positioned at 0° . This reaction is a typical case of the reaction in inverse kinematics at beam energy around the lower edge of the region of energies comparable to the Fermi energy.

The results of the PE+DIT/ICF+GEMINI calculation, compared to experimental observables are given in Fig. 2.13. In Fig. 2.13a the mass yield curve is presented. The measured data, normalized for beam current and target thickness are given in mb and presented as solid circles. The result of the DIT+ICF/GEMINI calculation, filtered by the spectrometer angular and momentum acceptance is given by the full line, whereas the dashed line gives the total (unfiltered) yield. A comparison of the measured yields to the calculated filtered yields shows reasonable agreement for the heavier projectile-like fragments ($A > 90$). The missing experimental cross section at the masses close to the beam is caused by the limitations of the experimental set-up, imposed by the background from the scattered primary beam. The yields of residues with $A < 90$ are increasingly underestimated by the calculation despite the fact that the unfiltered calculated yields are rather flat in this region, which appears to reflect the trend of the experimental data. Since, according to Fig. 2.13a, the yield of unfiltered residues with $A < 90$ is rather flat, the missing filtered yield below $A=90$ in the calculation appears to be caused by the fact that the kinematic properties of the simulated residues with $A < 90$ increasingly miss the spectrometer acceptance with decreasing mass, leading to increasing losses in the filtering procedure.

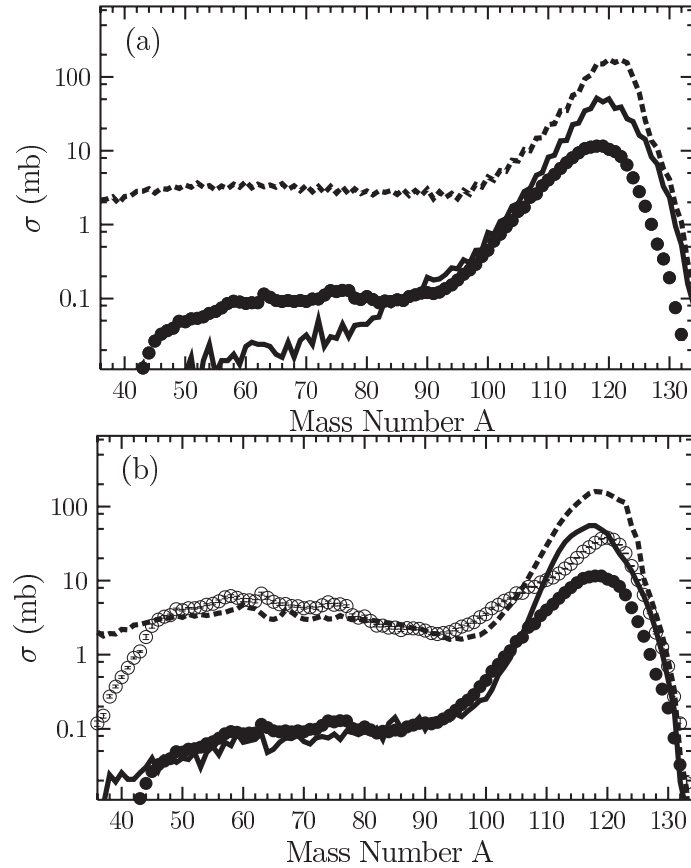


Fig. 2.13. Fragment distributions for the reaction 20 AMeV $^{124}\text{Sn} + ^{27}\text{Al}$. (a) - isobaric yield distribution. The data are shown as solid circles. The dashed line is the result of DIT+ICF/GEMINI (see text). The full line is the result of the same calculation as the dashed line, but imposing a cut corresponding to the angular and momentum acceptance of the spectrometer. (b) as in (a), except that the calculations are DIT+ICF/SMM. Open circles in show estimated total cross sections (see text).

An alternative calculation was carried out, where the SMM code was used for the de-excitation of the hot nuclei produced by the DIT+ICF simulation. In the SMM calculation, a freeze-out configuration with hot primary fragments was assumed. Hot fragments are propagated in the Coulomb field and de-excited by secondary emission. Only thermal excitation energy is used as input while the rotational energy (typically not exceeding 10 MeV) is subtracted. The results are presented in Fig. 2.13b in a fashion analogous to Fig. 2.13a. The PE+DIT/ICF+SMM calculation provides very consistent description of experimental observables for $A < 105$ (the discrepancies in the region close to the beam are analogous to previous cases). Using the ratio of filtered to unfiltered calculated yield for each mass, correction factors (whose magnitude are inferred from Fig. 2.13b) for the acceptance of the spectrometer can be obtained as a function of mass. When

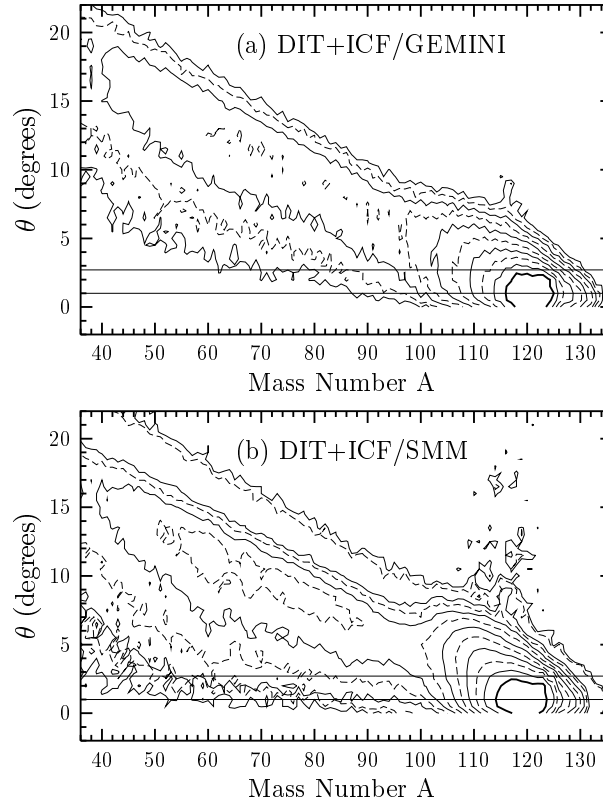


Fig. 2.14. Calculated angular distributions in the laboratory system for the reaction 20 AMeV $^{124}\text{Sn} + ^{27}\text{Al}$ as a function of residue mass for GEMINI (a) and SMM (b). Successive contours correspond to a decrease of the yield by a factor of 2. The two horizontal lines mark the angular acceptance of the MARS separator used in the present work.

applied to the measured yield data, an estimate of the total yield, shown by the open circles in Fig. 2.13b, could be obtained.

Thus, implementation of the prompt multifragmentation scenario appears to lead to production of heavy residues with proper kinematics. Compared to light particles or intermediate mass fragments (IMFs) used for imaging of the emitting source via particle-particle correlations, the experimentally detected heavy residues possess direct information on the properties of hot multifragment partitions. The process of secondary emission, as can be concluded from the simulations, does not influence significantly the kinematic properties of the heavy residues with masses $A=40-90$, since emission of nucleons is a dominant channel of secondary de-excitation.

Detailed insight into the different kinematic properties of residues simulated using GEMINI and SMM codes can be obtained from Fig. 2.14, where the calculated angular distributions are presented as a function of residue mass for GEMINI (a) and SMM (b). Two horizontal lines

mark the angular acceptance of the MARS separator. It is remarkable to notice that, in fact, the gross features of both distributions are very similar and the experimental effect appears to be caused by the distant tail of the distribution, which extends much further toward zero angle in the scenario where the hot nucleus disintegrates at once into more pieces. Nevertheless, the essential feature of the zero angle region is that it is highly selective toward products from incomplete or complete fusion channel since the hot source is flying essentially along the beam direction and the final angular distribution is determined by the de-excitation process. In the case when the hot nucleus disintegrates by sequential binary decay, the recoil from emitted fragments causes a shift of the residue angle away from the zero angle. In any case, it can be concluded, that the model of incomplete fusion [41], when combined with appropriate description of de-excitation, offers a consistent description of dynamical stage in the central collisions at intermediate beam energies.

According to the incomplete fusion model [41], the cold fragmentation-like residues should be increasingly dominant products for the channels with the number of stripped protons exceeding seven to eight. Thus the products of primary interest are the heavy residues considerably lighter than the initial projectile. The reaction of massive heavy ions ^{129}Xe with light target ^{27}Al was investigated in the work [69]. Projectile-like residues were observed at forward angles using the spectrometer A1200 [70]. In analogy to the reaction $^{124}\text{Sn} + ^{27}\text{Al}$ at the beam energy 20 AMeV, also in the reaction $^{129}\text{Xe} + ^{27}\text{Al}$ at beam energy 26 AMeV the PE+DIT/ICF+SMM simulation, filtered for separator acceptance, reproduced reasonably well the experimental data for $Z = 44\text{--}49$, representing the violent collisions.

In order to further examine the prediction of the ICF model [41], the results of PE+DIT/ICF+SMM simulations [71] were compared to experimental mass distributions of elements with $Z = 21\text{--}29$ observed in the reaction $^{86}\text{Kr} + ^{124,112}\text{Sn}$ at 25 AMeV [51]. In these reactions the simulation overpredicted the experimental yields of the most neutron-rich products below nickel (with more than 8 stripped protons). The situation was similar also for the reaction $^{86}\text{Kr} + ^{112}\text{Sn}$ even if the most neutron-rich products below nickel are less populated than in reaction of $^{86}\text{Kr} + ^{124}\text{Sn}$. To correct this, a component of excitation energy, dependent on isospin asymmetry was deduced [71], assuming fast transfer of neutrons to the cold projectile-like fragment. Such modification in the model of incomplete fusion is consistent with both overall model framework and experimental data and thus one can expect improved predictive power which can be used to predict production of exotic mid-heavy to heavy neutron-rich nuclei in the reactions around the Fermi energy, and possibly identify under which conditions such approach can be more effective than other methods. From the point of view of reaction dynamics, the modified model of incomplete fusion is consistent with the formation of a neutron-rich region between cold and hot fragment (or participant zone as its precursor). Similar effect was reported in the literature [72] as a possible consequence of the evolution of nuclear mean field. The number of transferred neutrons can then be determined by a mechanism similar to the random neck rupture, as established in nuclear fission [73], which can justify the applicability of a combinatorial (and thus essentially statistical) probability in the description of dynamical reaction mechanism such as the incomplete fusion.

The reaction of massive heavy ions ^{129}Xe with light target ^{27}Al was investigated in the work [69] also at the projectile energy 50 AMeV. While at beam energy 26 AMeV the PE+DIT/ICF+SMM simulation, filtered for separator acceptance reproduced reasonably well the experimental data, rather surprisingly, at the beam energy 50 AMeV the filtered PE+DIT/ICF+SMM simulation fails to reproduce the experimental data, both in terms of magnitude and neutron excess.

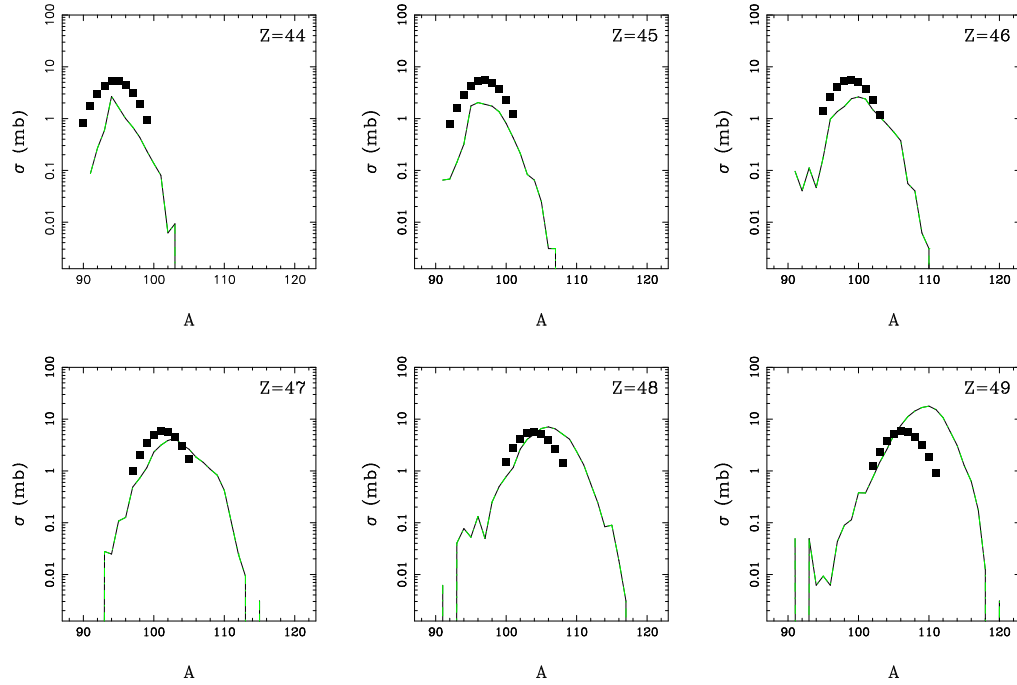


Fig. 2.15. Experimental (symbols) and simulated mass distributions in the reaction $^{129}\text{Xe}+^{27}\text{Al}$ at 50 AMeV for selected elements between iron and krypton. Lines represent the PE+participant-spectator+SMM simulation after filtering procedure taking into account angular acceptance of the A1200 spectrometer and subtraction of six neutrons prior to de-excitation.

A possible explanation for the failure of the PE+DIT/ICF simulation can be a transition from the binary ICF scenario to ternary participant-spectator scenario. To test this hypothesis the ICF model was modified so that both spectators remain cold, gaining excitation energy and kinematic properties in the same way as the cold fragment in the binary ICF scenario. Simulation using this model was performed and an improvement was achieved in terms of magnitude, however the shift in the isospin, with experimental data being less neutron-rich, remained practically unchanged. It is de-facto excluded that the isospin shift could be caused by de-excitation stage, since in the same reaction at lower beam energy 26 AMeV no such shift is observed. Thus the shift is caused by the dynamical stage. One possible cause of the shift can be in the mechanism of dynamical emission of neutrons, as recently reported in the work [74]. If such emission takes place during the re-separation, a significant shift toward proton-rich side can be achieved. Such assumption was tested by a modified participant-spectator simulation (solid line in Fig. 2.15) where six neutrons (with corresponding decrease of excitation energy) were subtracted from the projectile-like spectator. This simulation leads to reasonable agreement with experimental data, thus suggesting that mean field effects in the re-separation stage can influence the production cross sections of heavy residues, primarily in proton-rich systems.

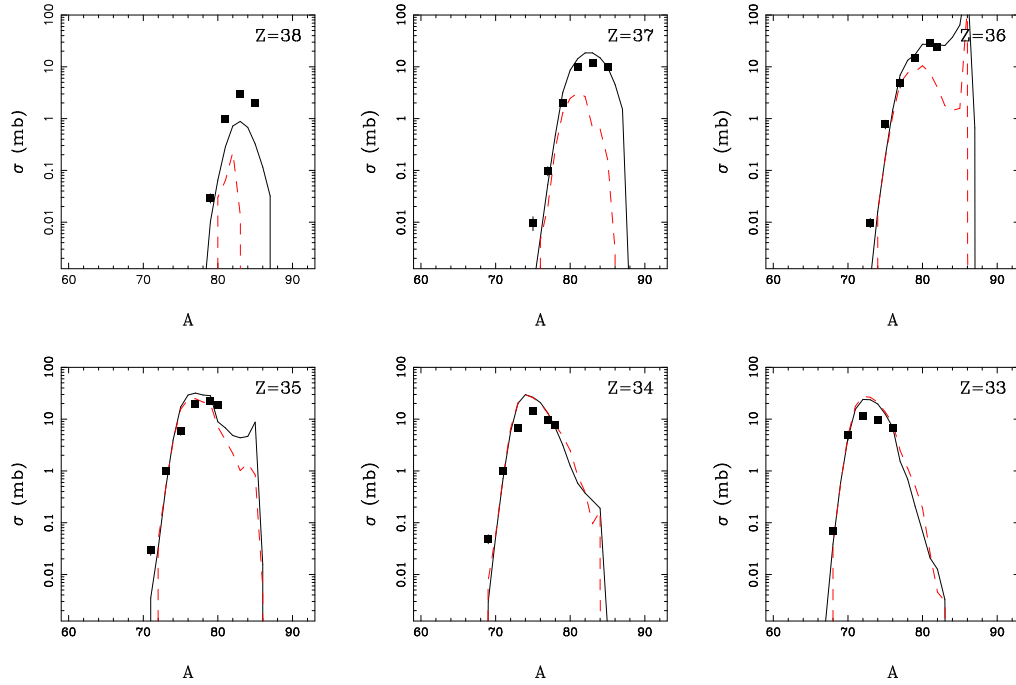


Fig. 2.16. Experimental (symbols) and simulated (lines) mass distributions in the reaction $^{86}\text{Kr}+^{27}\text{Al}$ at 70 AMeV for selected elements. Dashed line - PE+participant-spectator+SMM simulation after filtering procedure taking into account angular acceptance of the A1200 spectrometer. Solid line - PE+DIT/ICF+SMM simulation after filtering procedure.

A test of the onset of the participant-spectator scenario can be provided by the reaction of ^{86}Kr beam with light target ^{27}Al which was investigated in the work [75] at beam energy 70 AMeV, above the Fermi energy domain. As can be seen in Figure 2.16, the filtered participant-spectator simulation (solid line), with filtering procedure approximating the angular acceptance of the spectrometer A1200 [70] used in the experiment [75], appears to reproduce the experimental data below the projectile (symbols). It is however worthwhile to note that the PE+DIT/ICF simulation is successful below the projectile and works better at elements heavier than the projectile. This is caused by the fact that in pure participant-spectator scenario, the formation of sources heavier than projectile is only a statistical fluctuation with low probability.

Further test of the onset of the participant-spectator scenario can be provided by the reaction of ^{78}Kr beam with target ^{58}Ni which was investigated in the work [76] at beam energy 75 AMeV, again above the Fermi energy domain. In this case the filtered participant-spectator simulation, with filtering procedure approximating the angular acceptance of the spectrometer A1200 as used in the experiment [76], comprehensively fails to reproduce the experimental data. On the other hand, figure 2.17 shows that the filtered PE+DIT/ICF+SMM simulation (dashed line) appears to reproduce the magnitude of the cross section in the experimental data (symbols). There

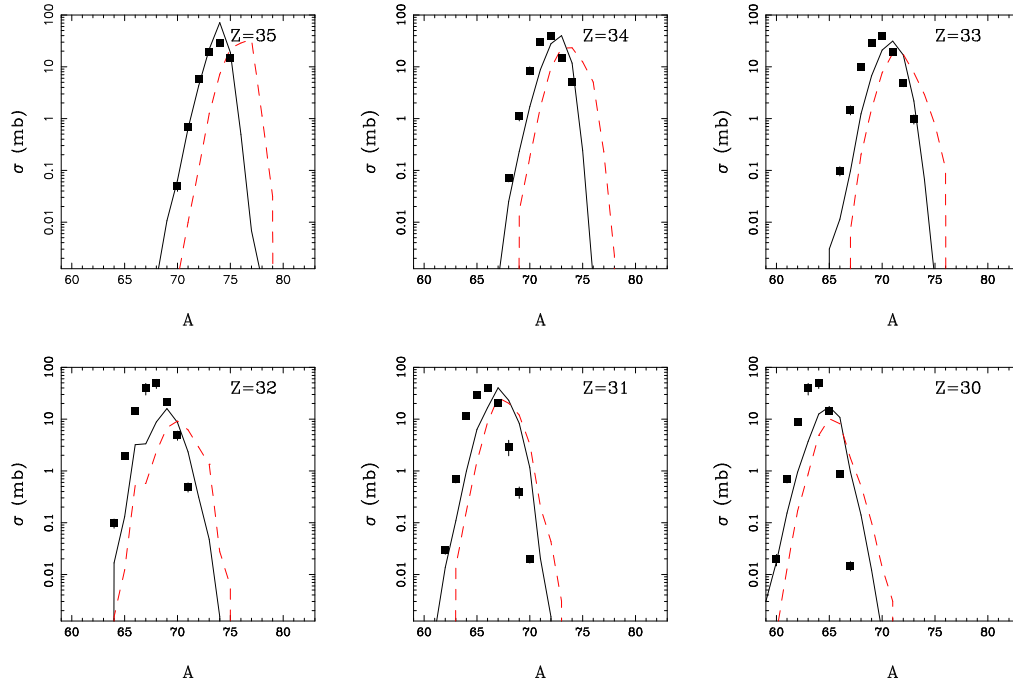


Fig. 2.17. Experimental (symbols) and simulated (lines) mass distributions in the reaction $^{78}\text{Kr}+^{58}\text{Ni}$ at 75 AMeV for selected elements. Solid line - PE+DIT/ICF+SMM simulation after filtering procedure taking into account angular acceptance of the A1200 spectrometer. Dashed line - PE+DIT/ICF+SMM simulation after subtraction of four neutrons and filtering procedure.

again remains a shift in the isospin of the heavy residues, similar to the reaction $^{129}\text{Xe}+^{27}\text{Al}$ at 50 AMeV. Also in this case improvement was achieved by subtracting neutrons prior to de-excitation, in this case four of them, as is documented in Figure 2.17 by the solid lines. Thus again an isospin-dependent mechanism of dynamical emission of neutrons appears to play role.

Based on previous analysis, the reaction $^{86}\text{Kr}+^{181}\text{Ta}$ at 64 AMeV, in normal kinematics at projectile energy above Fermi energy domain, can be expected as a case where the PE+DIT/ICF+SMM simulation will perform well. This is documented in Figure 2.18, where the filtered PE+DIT/ICF+SMM simulation (solid line), with filtering procedure approximating the angular acceptance of the spectrometer RIPS [77], appears to reproduce the experimental data (symbols) quite well. Again in this neutron-rich case, there is no need to correct for the isospin shift by subtraction of neutrons, thus suggesting that in neutron-rich systems such emission either does not exist or is indistinguishable from intense emission of neutrons in the de-excitation stage.

Another signal of dynamical neutron emission was demonstrated in the work [74] using the reactions $^{40,48}\text{Ca} + ^{27}\text{Al}$ at 45 AMeV. In the experiment, the mass and atomic number of the detected charged particles were identified up to $Z = 8$. For the subset of events where all detected charged particles were identified, it was possible to reconstruct the mass, charge and

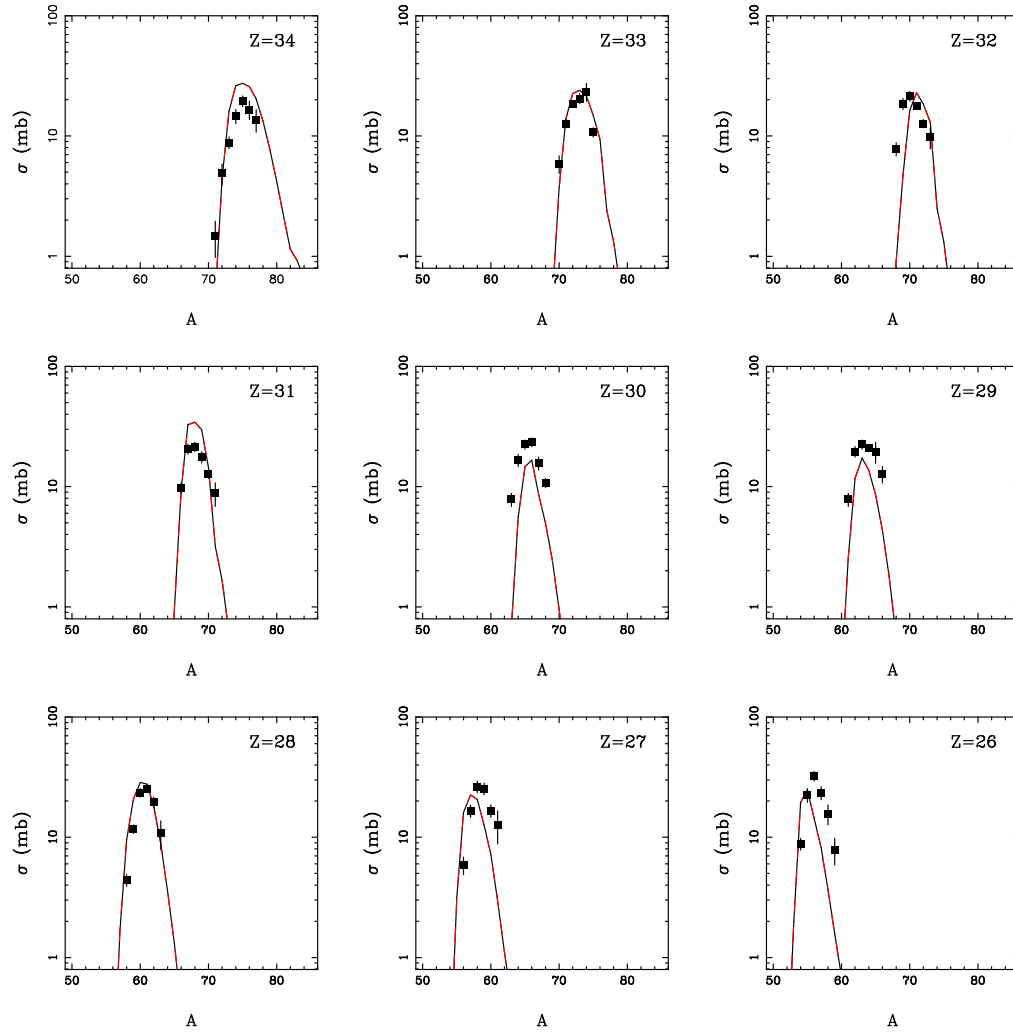


Fig. 2.18. Experimental (symbols) and simulated (lines) mass distributions in the reaction $^{86}\text{Kr}+^{181}\text{Ta}$ at 64 AMeV for selected elements. Solid line - PE+DIT/ICF+SMM simulation after filtering procedure taking into account angular acceptance of the RIPS spectrometer.

excitation energy of the composite system, in the same way as in the earlier work [78]. The analysis was performed on the subset of events with total charge larger than that of the projectile ($Z \geq 21$), thus selecting events where the incomplete fusion, occurring in mid-central collisions, is the dominant contributing reaction mechanism. The excitation energy distributions of the reconstructed quasi-projectiles in the reactions $^{40,48}\text{Ca} + ^{27}\text{Al}$ at 45 AMeV (see Fig. 2.19a) are practically identical, what is somewhat surprising when taking into account that the number of

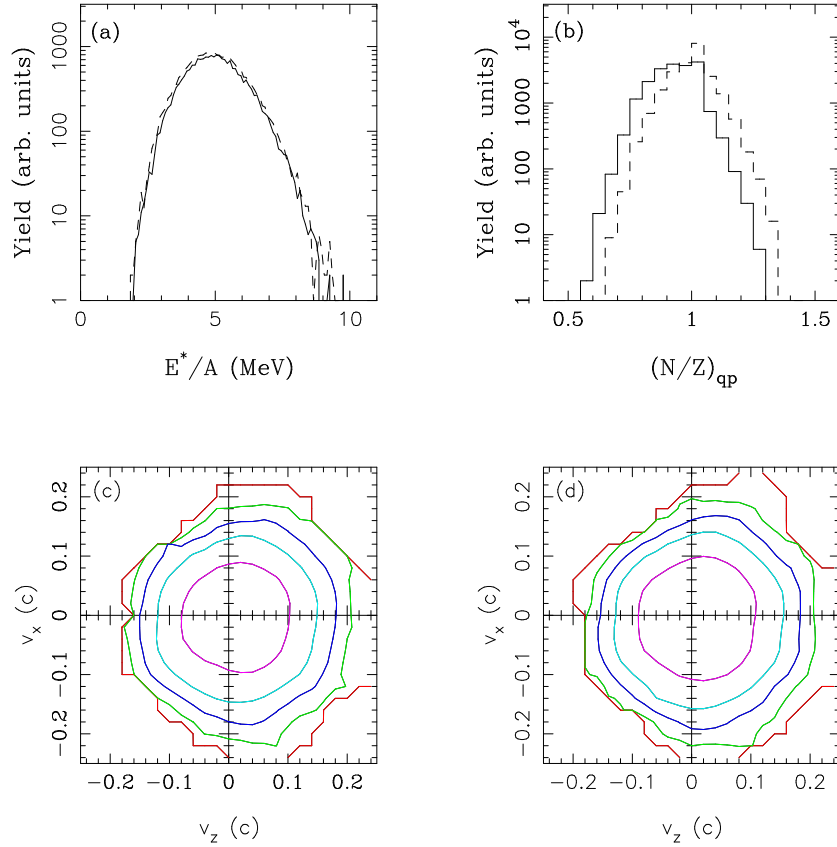


Fig. 2.19. (a) Excitation energy distributions of reconstructed quasi-projectiles from the reactions $^{40,48}\text{Ca} + ^{27}\text{Al}$ at 45 AMeV (solid line for ^{40}Ca and dashed line for ^{48}Ca), (b) N/Z -distributions of the reconstructed quasi-projectiles (solid line for ^{40}Ca and dashed line for ^{48}Ca), (c) Velocity-plot of the light charged particles from the reaction $^{40}\text{Ca} + ^{27}\text{Al}$ at 45 AMeV, (d) Velocity-plot of the light charged particles from the reaction $^{48}\text{Ca} + ^{27}\text{Al}$ at 45 AMeV.

missing (undetected) neutrons may differ considerably. A possible uncertainty in the evolution of neutrons can be documented also by the observed N/Z -distributions (see Fig. 2.19b) which reflect the initial N/Z -difference of the two projectile nuclei (amounting to 0.48) only partially, since the mean values (centroids) in the reactions $^{40,48}\text{Ca} + ^{27}\text{Al}$ are $N/Z=0.93$ and 1.01 , respectively. The velocity-plots of the light charged particles in the quasi-projectile frame in these two reactions are shown in Fig. 2.19 (for ^{40}Ca on panel 2.19c and for ^{48}Ca on panel 2.19d). Practically isotropic emission is observed which implies the statistical multifragmentation of the hot projectile-like nucleus. A slight suppression at the backward hemisphere is caused by the combined effect of limited angular coverage and energy thresholds of the experimental device.

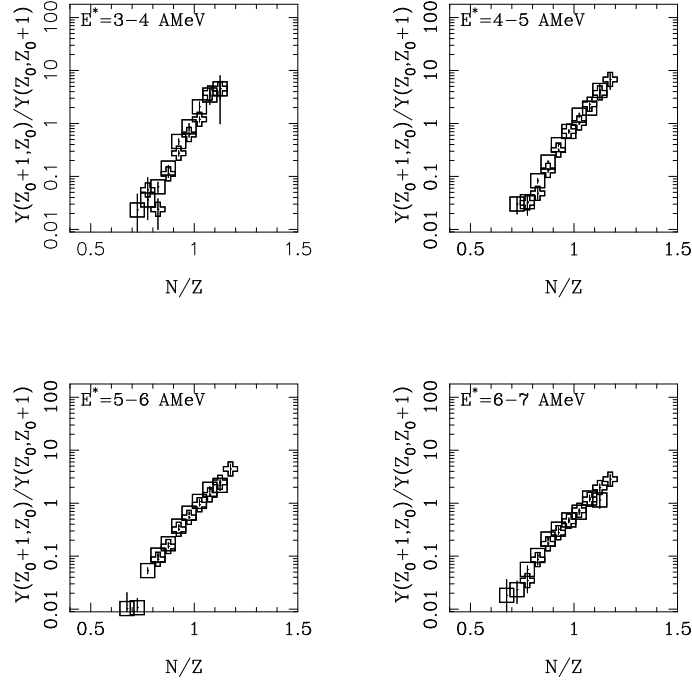


Fig. 2.20. Trends of the yield ratio of the mirror nuclei ${}^3\text{H}$ and ${}^3\text{He}$ for two reactions ${}^{40,48}\text{Ca}+{}^{27}\text{Al}$ in four excitation energy bins plotted as a function of the N/Z of the reconstructed quasiprojectile.

In the case of the reactions ${}^{40,48}\text{Ca}+{}^{27}\text{Al}$, even when assuming an incomplete fusion scenario, one has to expect that there will be a considerable difference in neutron excess of the hot systems in the two reactions (seven neutrons according to the simulation). In order to check difference in the number of missing neutrons, the trends of the yield ratios of mirror nuclei were compared. In Figure 2.20 are shown the trends of the yield ratio of the mirror nuclei ${}^3\text{H}$ and ${}^3\text{He}$ for two reactions ${}^{40,48}\text{Ca}+{}^{27}\text{Al}$ as a function of the N/Z of the reconstructed quasiprojectile and the two dependences are identical for all four excitation energy bins. Similar behavior is observed also for other three yield ratios of the mirror nuclei (${}^7\text{Li}/{}^7\text{Be}$, ${}^{11}\text{B}/{}^{11}\text{C}$, ${}^{15}\text{N}/{}^{15}\text{O}$). This behavior further documents that indeed the fragment yield ratios exhibit identical dependence on N/Z of the quasiprojectile, independent of the initial neutron excess. In this context, it is notable that also the caloric curves (dependences of temperature on excitation energy of the hot nucleus) are almost identical in both reactions, despite the expected significant difference of total excitation energy after including the missing neutrons. Thermodynamical observables thus, remarkably, do not exhibit sensitivity to the number of missing (undetected) neutrons in the two reactions.

As an explanation one has to assume that the apparent excitation energy, reconstructed using observed charged particles, is close to the true excitation energy of the hot equilibrated source, and the excess neutrons in the neutron-rich case are not part of the equilibrated source, due to dynamical emission taking place prior to equilibration. Such explanation is consistent with the

almost identical experimental excitation energy distributions shown in Fig. 2.19a for two reactions $^{40,48}\text{Ca}+^{27}\text{Al}$ and is also supported by the lack of the effect of missing neutrons on the scaling shown in Fig. 2.20. Dynamical emission of neutron-rich charged particles at mid-velocity was reported in recent years [72] and interpreted as caused by the formation of a neutron-rich neck. Such scenario can provide an explanation also in the present case, with the notable difference that the neck structure may be formed exclusively by neutrons. In the present case the low-density region between the projectile and the target can be expected to be very neutron-rich [79], since the nuclear equation of state for sub-saturation densities provides stable solutions only outside of the spinodal region and thus at very asymmetric N/Z ratios. A behavior consistent with the present case was reported recently [71] in incomplete fusion reactions, where an isospin-dependent component of excitation energy was necessary to explain the production of neutron-rich fragmentation products. Such behavior is consistent with rupture of the neck structure formed by the neutrons in the region between the hot and cold pre-fragments during the dynamical stage. Unlike the reported cases, where signatures of neck formation were reported in symmetric damped collisions of massive nuclei [72], in the present case the alternative explanation due to Coulomb force of the massive external charge [80] can be excluded. The remaining charge, especially in the incomplete fusion reactions, is rather small, and the observed trends may be attributed solely to the effect of the nuclear mean field.

Table 2.1 shows a set of reactions, considered in the systematic analysis at the low and intermediate energies [84]. The available data cover significant part of the matrix, with few exceptions at low and transitional energies. Table 2.2 provides overview of the dominant reaction mechanisms inside individual cells of the matrix. As one could expect, the scenario involving pre-equilibrium emission in the early stage followed by deep-inelastic transfer or incomplete fusion leads to consistent results in most of the cases above 10 A MeV. It nevertheless appears that participant-spectator scenario starts to play role at energies above 50 A MeV for very asymmetric projectile-target combinations. Also in this domain there are signals of the mechanism of neutron loss (dynamical emission) preceding the thermal equilibration of the massive projectile-like fragment. Such effect seems to be more pronounced in the case of proton-rich projectile-like fragments while in neutron-rich cases it may be overshadowed by intense statistical emission of neutrons. Signal of analogous behavior of neutron was observed also in the multifragmentation data in the work [74]. Also the behavior in semi-central collisions at lower energies [71], where fast transfer of multiple neutrons can be deduced, points toward non-standard dynamical evolution of neutrons, most probably in the neck region between the projectile and target. At the beam energies below 10 A MeV, deep-inelastic transfer appears to be dominant reaction mechanism, with the possible extended evolution of nuclear profile in the window (neck) region, mostly in the case of heavy target nuclei.

Besides the phenomenological models described above, there are several implementations of the solution of the Boltzmann equation, such as the Boltzmann-Uehling-Uhlenbeck equation (BUU) or Quantum Molecular Dynamics (QMD), used for description of the nucleus-nucleus collisions at intermediate energies. Among these implementations, the so-called Constrained

Tab. 2.1. Classification of investigated reactions based on mass asymmetry and beam energy

	Normal kinematics	Nearly symmetric	Inverse kinematics
Low energies up to 10 AMeV	$^{58}\text{Ni}+^{208}\text{Pb}$, E=5.7 AMeV [32] $^{64}\text{Ni}+^{208}\text{Pb}$, E=5.5 AMeV [36] $^{64}\text{Ni}+^{238}\text{U}$, E=6.1 AMeV [37] $^{22}\text{Ne}+^{232}\text{Th}$, E=7.9 AMeV [38] $^{22}\text{Ne}+^{90}\text{Zr}$, E=7.9 AMeV [39]		
Transitional energies from 10 to 20 AMeV		$^{86}\text{Kr}+^{64}\text{Ni}$, E=15 AMeV $^{40}\text{Ar}+^{64}\text{Ni}$, E=15 AMeV $^{40}\text{Ar}+^{64}\text{Ni}$, E=15 AMeV $^{124}\text{Sn}+^{124}\text{Sn}$, E=20 AMeV [81]	$^{124}\text{Sn}+^{27}\text{Al}$, E=20 AMeV [68]
Fermi energy domain from 20 to 50 AMeV	$^{129}\text{Xe}+^{197}\text{Au}$, E=44 AMeV [82]	$^{86}\text{Kr}+^{64}\text{Ni}$, E=25 AMeV [44] $^{86}\text{Kr}+^{112,124}\text{Ni}$, E=25 AMeV [51] $^{129}\text{Xe}+^{90}\text{Zr}$, E=44 AMeV [82]	$^{120}\text{Xe}+^{27}\text{Al}$, E=26 AMeV [69] $^{120}\text{Xe}+^{27}\text{Al}$, E=50 AMeV [69]
Fragmentation energies above 50 AMeV	$^{86}\text{Kr}+^{181}\text{Ta}$, E=64 AMeV [83]	$^{78}\text{Kr}+^{58}\text{Ni}$, E=75 AMeV [76]	$^{86}\text{Kr}+^{27}\text{Al}$, E=70 AMeV [75]

Tab. 2.2. Classification of principal reaction mechanisms based on mass asymmetry and beam energy

	Normal kinematics	Nearly symmetric	Inverse kinematics
Low energies up to 10 AMeV	Deep-inelastic transfer Extended nuclear profile ?		
Transitional energies from 10 to 20 AMeV		Pre-equilibrium emission Deep-inelastic transfer + Incomplete fusion	Pre-equilibrium emission Deep-inelastic transfer + Incomplete fusion
Fermi energy domain from 20 to 50 AMeV	Pre-equilibrium emission Deep-inelastic transfer + Incomplete fusion	Pre-equilibrium emission Deep-inelastic transfer + Incomplete fusion	Pre-equilibrium emission Deep-inelastic transfer + Incomplete fusion Participant-Spectator or Neutron loss ?
Fragmentation energies above 50 AMeV	Pre-equilibrium emission Deep-inelastic transfer + Incomplete fusion	Pre-equilibrium emission Deep-inelastic transfer + Incomplete fusion Neutron loss ?	Pre-equilibrium emission Deep-inelastic transfer + Incomplete fusion Participant-Spectator or Neutron loss ?

Molecular Dynamics (CoMD) [85] can be singled out as a good candidate for description of nucleus-nucleus collisions at intermediate energies. This model replaces the computationally awkward procedure of anti-symmetrization of nucleonic wave functions by a simpler procedure allowing to preserve limitations on occupation of available states, consistent with Fermionic nature of nucleons. As documented by the recent works [86, 87], this code allows to achieve agreement with experimental data, comparable with the above phenomenological description. Further work in this direction is of great interest.

2.3 Nuclear reactions at relativistic and ultra-relativistic energies

The beam energies above 100 A MeV can be considered as relativistic energies simply because the beam velocity exceeds 40% of the speed of light and classical Newtonian kinematics no longer describes kinematic properties of beam particles. Moreover, also the reaction mechanism at these energies differs from the low and intermediate energies. The collisions are faster, trajectories can be considered as straight lines, a simple geometric (Glauber) picture can be applied and nucleonic (or hadronic in general) degrees of freedom play dominant role.

When the products of interest are projectile-like and target-like fragments, the dominant reaction mechanism at the relativistic energies is represented by the geometric spectator-participant model where a hot region is formed in the participant zone (zone of geometric overlap) while the spectator regions are colder and can survive process of de-excitation as the projectile-like fragments. Still some of these spectators can be warm enough to undergo multifragmentation, especially in the semi-central collisions.

Depending on whether the product of interest is projectile-like or target-like fragment, the reactions are usually called either fragmentation or spallation reactions, respectively, but typically both of them represent the same class of reactions, either in inverse or in normal kinematics. For example, in spallation reaction the volume and thus the most probable mass A_{TS}^{abr} of the target spectator can be estimated as a function of the impact parameter using the model of geometrical abrasion [59]. The number of nucleons in the spectator zone A_{TS} can be estimated according to the binomial distribution

$$P(A_{TS}) = \binom{A_T}{A_{TS}} \left(\frac{A_{TS}^{abr}}{A_T} \right)^{A_{TS}} \left(1 - \frac{A_{TS}^{abr}}{A_T} \right)^{A_T - A_{TS}} \quad (2.22)$$

where A_T is the target mass number. The charge of the spectator Z_{TS} can be determined as [63]

$$P(Z_{TS}) = \frac{\binom{Z_T}{Z_{TS}} \binom{N_T}{N_{TS}}}{\binom{A_T}{A_{TS}}} \quad (2.23)$$

where Z_T is the target mass number and N_{TS} and N_T are the neutron numbers of the target spectator and the target, respectively. The excitation energy of the target spectator can be estimated, according to [64], as proportional to the number of abraded nucleons with the proportionality factor 27 MeV, which was found to be consistent with experimental data [88]. The formulas for the projectile spectator are analogous, after replacing the target index T with projectile index P .

A successful implementation of the above geometric picture can be found in the ABRABLA code [64,89,90,91] (its name being derived from the alternative name of the geometric participant-spectator model, the so-called abrasion-ablation model) which is routinely used for the prediction of the yields of spallation and fragmentation products. ABRABLA is a Monte-Carlo code dedicated to calculations of production cross sections and velocities of residues produced in relativistic heavy-ion collisions. It consists of ABRA - improved version of the abrasion model for peripheral and mid-peripheral collisions of relativistic heavy ions [64, 92] and ABLA - a fast code for simulation of the deexcitation cascade (particle evaporation and fission) of an excited nucleus [93]. It allowed to reproduce e.g. an extensive set of high-quality experimental fragment production cross sections, measured at the fragment separator FRS at GSI Darmstadt using the beams of ^{56}Fe , ^{136}Xe , ^{197}Au , ^{208}Pb and ^{238}U , delivered by the synchrotron SIS. The relatively simple geometric abrasion-ablation model thus proves to be a valuable tool, which can be used for applications such as prediction of the yields of rare ion beams or development of the future facilities for transmutation of nuclear waste. Other implementations of the geometric picture can be found in the codes such as EPAX [46] and COFRA [94], which are also used mostly for the prediction of the yields of fragmentation products.

While the abrasion-ablation models consider collision geometry in terms of participant and spectator zones, the model of intranuclear cascade (INC) is based on the assumption that nuclear collisions can be described as a sequence of independent nucleon-nucleon collisions, leading to prompt emission of particles and to two-body dissipation of the kinetic energy of the relative motion into intrinsic (thermal) excitation energy of the resulting pre-fragments. As a consequence, the hot and cold zones are again formed consistently with the participant-spectator scenario. Various implementations of the model of intranuclear cascade exist, most notably INC models of Yariv and Fraenkel [95] and Bertini [96]. As in the case of the pure participant-spectator scenario, the use of the INC model can be justified at relativistic energies, with typical lower limit of applicability around 100 A MeV. An example of the implementation of the model of intranuclear cascade is the code ISABEL [95], which, among others, allowed to describe the mass distributions of the projectile-like fragments in the reaction of $^{84}\text{Kr}+^{197}\text{Au}$ at 200 A MeV [97]. Still, for such predictions of mass distributions the geometrical model appears as better solution, due to its computational simplicity. On the other hand, the intranuclear cascade allows to predict production of all classes of reaction products e.g. emission of cascade particles (neutrons, light charged particles, pions) in coincidence with heavier projectile- or target-like products. A rather comprehensive set of cascade models describing the nuclear reactions in this energy range can be also found in several Monte Carlo simulation codes such as Geant4 [98], MARS [99] or MCNP [100]. All of them provide a hybrid set of models describing subsequent stages of simulations (hadronic cascade, primary and secondary fragmentation, or eventually particle transport). Such codes are used for wide range of applications such as detector design, simulations for space research or nuclear energy.

Further extension of the model description can be made by supplementing the intra-nuclear cascade by the effect of the nuclear mean field, which leads to either one-body dissipation or to emission of particles accelerated by the force caused by its strong gradient. Such a transport model is very useful to treat dynamics of the heavy ion collision and obtain important information of nuclear matter EoS as well as the symmetry energy. In relativistic energy heavy ion collisions, the Boltzmann-Uehling-Uhlenbeck model is an extensively useful tool [101, 102], which takes both nuclear mean field and Fermionic Pauli blocking into consideration. The BUU equation

reads

$$\begin{aligned} \frac{\partial f}{\partial t} + v \cdot \nabla_r f - \nabla_r U \cdot \nabla_p f &= \frac{4}{(2\pi)^3} \int d^3 p_2 d^3 p_3 d\Omega \frac{d\sigma_{NN}}{d\Omega} v_{12} \\ \times [f_3 f_4 (1-f)(1-f_2) - f f_2 (1-f_3)(1-f_4)] \delta^3(p + p_2 - p_3 - p_4), \end{aligned} \quad (2.24)$$

where $f=f(r, p, t)$ is the phase-space distribution function. It is solved with the test particle method of Wong [103], with the collision term as introduced by Cugnon, Mizutani and Vandermeulen [104]. In Eq.(2.24), $\frac{d\sigma_{NN}}{d\Omega}$ and v_{12} are in-medium nucleon-nucleon cross section and relative velocity for the colliding nucleons, respectively, and U is usually the sum of the single-particle mean field potential with the isospin-dependent symmetry energy term

$$U = a\rho + b\rho^\kappa + 2a_s \left(\frac{\rho}{\rho_0} \right)^\gamma \tau_z I, \quad (2.25)$$

where $I = (\rho_n - \rho_p)/\rho$, ρ_0 is the normal nuclear matter density; ρ , ρ_n , and ρ_p are the nucleon, neutron and proton densities, respectively; τ_z assumes value 1 for neutron and -1 for proton, coefficients a , b and κ represent properties of the symmetric nuclear matter while the last term, which describes the influence of the symmetry energy, can be obtained e.g. from simple Weizsacker formula, where a_s represents the coefficient of the symmetry energy term and γ is the exponent, describing the density dependence. Typical sets of mean field parameters cover substantial range, between the soft EoS with the compressibility K_0 of 200 MeV and the stiff EoS with K_0 of 380 MeV [101].

Another method of the solution of the Boltzmann equation is the quantum molecular dynamics (QMD), with the main difference by using the Gaussian wave packets instead of the sets of test particles. Both BUU and QMD are a suitable platforms for the investigation of the nuclear equation of state. At beam energies well above 1 AGeV, it is important to implement all the channels, leading to production of elementary particle in the two-body collisions, what typically leads to softening of the nuclear equation of state. Principal advantage of the simulations, based on the Boltzmann equation, over the pure intra-nuclear cascade is the possibility to describe the flow phenomena.

The flow observables were introduced primarily as observables directly related to the equation of the state of nuclear matter. Essentially, different flow observables can be identified with the coefficients of the Fourier expansion of the azimuthal angular distribution of particle multiplicity N relative to the reaction plane

$$\frac{d^3 N}{dp_t dy d\Phi} = \frac{1}{2\pi} \frac{d^2 N}{dp_t dy} (1 + 2v_1 \cos(\Phi) + 2v_2 \cos(2\Phi) + \dots) \quad (2.26)$$

where p_t is the transverse momentum, y is rapidity, Φ is the azimuthal angle relative to the reaction plane. The Fourier coefficients (components of transverse flow) can be determined as

$$v_n = \langle \cos(n\Phi) \rangle \quad (2.27)$$

of which the flow observable, related to the first Fourier coefficient v_1 is usually called as directed flow, which can be related to the nuclear stopping [105]. It can be alternatively expressed in terms of the slope of the momentum p_x (in the reaction plane) at zero rapidity. The elliptic

flow, which describes the azimuthal momentum space anisotropy of particle emission from non-central heavy-ion collisions in the plane transverse to the beam direction, is characterized by the value of the second Fourier coefficient v_2 . The reasons for emergence of flow can be related to the properties of the nuclear media, such as stopping, incompressibility, and symmetry energy, described by the equation of the state.

Besides the study of equation of state, the nucleus-nucleus collisions in this energy range allow to do detailed studies of in-medium mass modification of hadrons, such as ρ , ω and ϕ mesons, thus performing an in-medium hadron spectroscopy, providing a unique testing ground for the non-perturbative quantum chromo-dynamics (QCD). Such physical programme is addressed e.g. by the hadronic detector HADES at GSI Darmstadt [106]. To provide a physics analogy, one is attempting to search for a change of the hadronic excitation spectrum by an external field (represented by its surrounding nuclear matter). This is analogous to atomic physics where external electromagnetic fields change the spectrum, as verified by the Stark and Zeeman effects.

At very high (ultra-relativistic) energies the beam velocity is practically equal to the speed of light. There, in addition to production of elementary particles, a nuclear media known as hadronic gas, and, ultimately, quark-gluon plasma, can be created (for an overview see e.g. [107,108,109]). According to contemporary knowledge, the temporal evolution of a nucleus-nucleus collision at ultrarelativistic energies proceeds through the following stages: i) deconfinement of quarks and gluons due to the high energy deposited in the overlap region of the two nuclei; ii) equilibration of quarks and gluons; iii) crossing of the phase boundary and hadronization; iv) freeze-out.

Such a high-energy nucleus-nucleus collisions bear some similarity to the evolution of the early Universe, and the term Little Bang was introduced as its name. Obviously, the final state of collision, observed in the experiment, contains also information on the earlier stages of collision, however such information needs to be extracted using a sophisticated analysis of experimental data. Practically, mostly the remnants of the last stage of the collision, such as nucleons, hadrons and other elementary particles, are present in the final state which is observed in the experiment. It is the main task of experimental analysis to extract the information on the earlier stages from the distributions and properties of the particles in the final state. As a first step of analysis, the global properties of the final state, representing the freeze-out stage, can be examined. It has to be mentioned, that two different freeze-out stages are distinguished, the chemical freeze-out, when the particle production in two-body collisions freezes out and thus the relative abundances of different hadrons become fixed, and the kinematic freeze-out, when the two-body dissipation freezes out and momenta of the particles become fixed. Final state of the high-energy nucleus-nucleus collision thus bears resemblance to the relict radiation in cosmology, since it offers the information on temperature of the system at the freeze-out stage. Moreover, by using model assumption about evolution of the system, one can extract information on the earlier stage (again in analogy to cosmology). Still, such procedure is model-dependent, and the resulting values are as realistic as the model assumptions used.

Among the properties of nuclear matter at the early stage of the collision, the initial energy density, ε , and the net baryon density, n_{baryon} produced in a (central) heavy ion collision can be calculated from the measured transverse energy ($dE_t/d\eta$) and net baryon ($dN_{b-\bar{b}}/d\eta$) densities, respectively, in the so-called "Bjorken-scenario" [110]. This assumes self-similar (Hubble-like) homogeneous (hydrodynamical) expansion of the fireball in the longitudinal (beam) direction.

The resulting relations are

$$\varepsilon = \frac{1}{A_t} \frac{dE_t}{d\eta} \frac{d\eta}{dz}, \quad n_{baryon} = \frac{1}{A_t} \frac{dN_{b-\bar{b}}}{d\eta} \frac{d\eta}{dz} \quad (2.28)$$

where A_t is the transverse area of the fireball. In the above equations the only unknown parameter is the formation time (the time for establishing the equilibrium), τ ($d\eta/dz = 1/\tau$), which is usually taken to be 1 fm/c, although it is expected to decrease as a function of the energy. In this sense, the values obtained using the Eq. 2.28 provide conservative estimates for most of the energy range covered by the experiments. The experimental values of these observables are shown in Table 2.3, which is an updated version of the analogous table in the work [108], with the first experimental values from the LHC [111]. It is remarkable that the matter obtained at LHC matches in practically vanishing net baryonic density the matter created by the Big Bang. This might open possibilities for the study of matter-antimatter asymmetry in the early Universe.

The interesting experimental information on the chemical freeze-out stage is contained in the distributions of (mostly charged) hadrons. When assuming that the system is in thermodynamical equilibrium, values of thermodynamical observables can be extracted from the relative abundances of baryons. Thermodynamical analysis became a standard procedure in analysis of ultrarelativistic nucleus-nucleus collisions and it is described e.g. in [108]. The basic thermodynamical quantity required to compute the thermal composition of particle yields measured in heavy ion collisions is the partition function $Z(T, V)$. In the grand canonical (GC) ensemble, for particle i of strangeness S_i , baryon number B_i , electric charge Q_i and spin-isospin degeneracy factor $g_i = (2J_i + 1)(2I_i + 1)$, the partition function is

$$\ln Z_i = \frac{V g_i}{2\pi^2} \int_0^\infty \pm p^2 dp \ln[1 \pm \exp(-(E_i - \mu_i)/T)] \quad (2.29)$$

with (+) for fermions (baryons, made of 3 quarks) and (−) for bosons (mesons, made of quark-antiquark pairs). Furthermore, for massless particles (which is an acceptable approximation at ultra-relativistic energies) the analytic integration of Eq. 2.29 can be performed. The particle density is then

$$n_i = N/V = -\frac{T}{V} \frac{\partial \ln Z_i}{\partial \mu} = \frac{g_i}{2\pi^2} \int_0^\infty \frac{p^2 dp}{\exp[(E_i - \mu_i)/T] \pm 1} \quad (2.30)$$

Tab. 2.3. Measured quantities at AGS, SPS, RHIC and LHC for central nucleus-nucleus collisions.

Facility	AGS	SPS	RHIC	LHC [111]
$\sqrt{s_{NN}}$ (GeV)	4.9	17.3	200	2760
$dE_T/d\eta$ (GeV)	192	363	625	~1600
$dN_{b-\bar{b}}/d\eta$	170	100	25	~0
ε (GeV/fm ³)	1.2	2.4	4.1	~15
n_{baryon} (fm ⁻³)	1.1	0.65	0.17	~0

where T is the temperature and $E_i = \sqrt{p^2 + m_i^2}$ is the total energy. $\mu_i = \mu_b B_i + \mu_S S_i + \mu_{I_3} I_{3i}$ is the chemical potential, with μ_B , μ_S , and μ_Q the chemical potentials related to baryon number, strangeness and electric charge, respectively, which ensure the conservation (on average) of the respective quantum numbers: i) baryon number: $V \sum_i n_i B_i = Z + N$; ii) strangeness: $V \sum_i n_i S_i = 0$; iii) charge: $V \sum_i n_i I_{3i} = \frac{Z-N}{2}$. This leaves T and the baryochemical potential μ_b as the only parameters of the model, which need to be determined by comparison with experimental data. In practice, however, the volume determination may be subject to uncertainties due to incomplete stopping of the colliding nuclei. Due to this reason, the most convenient way to compare with measurements is to use particle ratios.

The interaction of hadrons and resonances is usually included by implementing a hard core repulsion of Van der Waals-type via an excluded volume correction. This is implemented in an iterative procedure according to

$$P^{excl.}(T, \mu) = P^{id.gas}(T, \hat{\mu}); \quad \hat{\mu} = \mu - V_{eigen} P^{excl.}(T, \mu) \quad (2.31)$$

where V_{eigen} is calculated for a radius of 0.3 fm, considered identical for all particles.

Such model assumptions are used to perform the so-called "thermal" fits of the particle yields, specifically of the particle yield ratios. The typical values of extracted temperatures are $T = 170$ MeV for SPS energies, $T = 200$ MeV for RHIC energies, and $T = 165$ MeV for LHC energies. It is interesting to observe that the freezeout temperature, measured at LHC, is lower than at RHIC. This imply much stronger expansion due to much higher initial density, as shown in Table 2.3. These values are comparable to or higher than the predictions of the lattice QCD calculations [112] for the critical temperature where the deconfinement phase transition is expected to occur. This is a strong argument for the onset of deconfinement, however by itself it can not be considered as a definite proof. Other observables, potentially capable to provide stronger evidence, will be discussed later.

Besides the study of the onset of deconfinement, nucleus-nucleus collision at ultrarelativistic beam energies offered a possibility to synthesize light anti-nuclei by the coalescence of anti-protons and anti-neutrons in the final state. Phase-space density of the final state at RHIC [113, 114] and at LHC [115] proved high enough for production of anti-nuclei up to the anti- α -particle and anti-hypernuclei. Study of such nuclei is of fundamental importance for physics, any inconsistency in properties of nuclei and corresponding anti-nuclei would be very interesting as a signature of the asymmetry of properties of matter and anti-matter, which is still an open question in cosmology and related astro-particle physics.

3 Production of exotic nuclei

Atomic nuclei are characterized by their number of constituent protons (Z) and neutrons (N). Chemical elements exhibit only limited number of stable isotopes (maximum being 10 stable isotopes of tin), which can be found in the Nature with various abundances. Limited amount of unstable isotopes can be encountered in the Nature due to radioactive decay of heavy long-lived primordial nuclei such as ^{238}U . Some radioactive isotopes in the Nature, such as ^{14}C , are produced by spallation reactions initiated by nucleons and light nuclei arriving to the Earth atmosphere as the cosmic rays.

Construction of powerful proton accelerators after the Second World War opened possibility to produce unstable nuclei in reactions of spallation. However, study of unstable nuclei was limited by necessity to process the irradiated target by the radiochemistry methods, which restricted this method to production of relatively long-lived unstable nuclei. Only after construction of accelerators, accelerating light and later also heavy ions, it became possible to produce short-lived unstable nuclei systematically within a wide range of proton-neutron asymmetries. Initially, the most frequently used type of reactions, initiated by the beams of heavy ions was the compound nucleus reaction [11], where statistically equilibrated compound nucleus is formed by fusion of the beam and target nuclei, and the excess of energy is disposed by emission of light particles (mostly neutrons) and γ -rays. This method allowed, among others, production of transfermium elements and access to the proton drip-line for wide range of chemical elements. Still, typical number of produced unstable nuclei (reaction channels) is limited to few species at a given beam energy. It was necessary to build more powerful heavy-ion accelerators, which allowed observation of deep-inelastic transfer (see, e.g. [3]), reactions where a wide range of unstable nuclei could be observed simultaneously. Further increase of the energy of heavy-ion beams facilitated use of reactions of nuclear fragmentation [116], de-facto a spallation reactions performed in inverse kinematics, where a wide range of projectile-like unstable nuclei can be produced and, eventually, used to form unstable secondary beams. In the meantime, applicability of spallation reactions for production of unstable nuclei was extended by the ISOL (Isotope Separation On-Line) method [6], allowing to transport unstable nuclei from the thick target, irradiated by high-energy proton beam, by thermal transport and subsequently ionize them and transport them to the experimental area as secondary beams. Possibility to induce nuclear processes with production of wide range of unstable secondary nuclei allowed to study the role of the proton-neutron asymmetry, or isospin asymmetry, in such processes, and, ultimately, the properties of the isospin-asymmetric nuclear matter. The stable nuclei observed in the Nature are proton-neutron symmetric at atomic masses up to 40, and above that mass an increasing neutron excess evolves in order to counterbalance increasing Coulomb repulsion among protons. For heaviest nuclei such as lead or uranium the neutron excess exceeds 50 %. However, there exist astronomical objects, called neutron stars, consisting almost exclusively of neutrons. Still there exists a wide range of isospin asymmetries, which can be observed only in the nuclear processes with intense evolution of the isospin degree of freedom, resulting in production of wide range of unstable nuclei. Very isospin-asymmetric nuclei can be in produced in various ways. The process of spallation or fragmentation (depending on reaction kinematics) allows to reach high isospin-asymmetry by knocking out protons and neutrons from the heavy reaction partner. Similar picture can in principle arise also if fusion reaction leads to highly excited compound nucleus, allowing emission of significant number of protons or neutrons. Reactions of deep-inelastic transfer

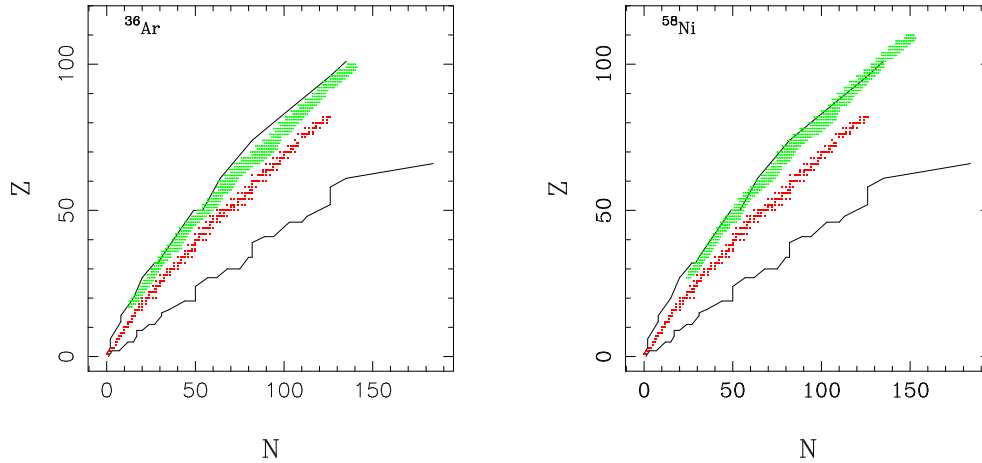


Fig. 3.1. Accessible regions of the proton rich nuclei (green), which can be produced using proton rich ion beams such as ^{36}Ar (left) and heavier ions ^{58}Ni (right) in the compound nucleus reactions. Red region represents stable target nuclei. Lines represent the proton and neutron driplines.

proceed by intense exchange of nucleons between the projectile and target nucleus. Process of nuclear fission bears some similarity to the deep-inelastic transfer, since exchange of nucleons can proceed simultaneously to shape evolution from parent nucleus through saddle configuration towards scission point. All these processes can be in principle understood as a form of random walk in the proton-neutron plane and suggest description in terms of transport theory, specifically of the nucleon transport. Role and influence of the isospin degrees of freedom is then demonstrated in the isotopic composition of the reaction products. In principle, cause and consequence can be reverted and isospin composition of the reaction products can be used as experimental observable carrying information on the role and evolution of the isospin degrees of freedom.

3.1 Production of proton-rich nuclei

Despite significant progress of the facilities, providing radioactive beams, the compound nucleus reactions around the Coulomb barrier remain the most common mechanism for production of neutron deficient nuclei, which are used for a wide range of spectroscopic studies. For this, the necessary experimental facilities are heavy ion accelerator, target system, kinematic separator and detection system. For illustration, Fig. 3.1 shows accessible regions of the proton rich nuclei, which can be produced using proton rich ion beams such as ^{36}Ar and ^{58}Ni , combined with stable target nuclei, in the most populated de-excitation channels such as 3-6n, p2-5n, a2-5n at and slightly above the Coulomb barrier.

Intense ion beams of ^{36}Ar and ^{58}Ni , or eventually heavier ones, thus lead to production of proton rich nuclei up to the proton dripline. Production rates are influenced by production cross sections in specific reactions, which are known to be rather high in the vicinity of the Coulomb barrier and decrease only in the region of fissile nuclei heavier than lead, due to competition with

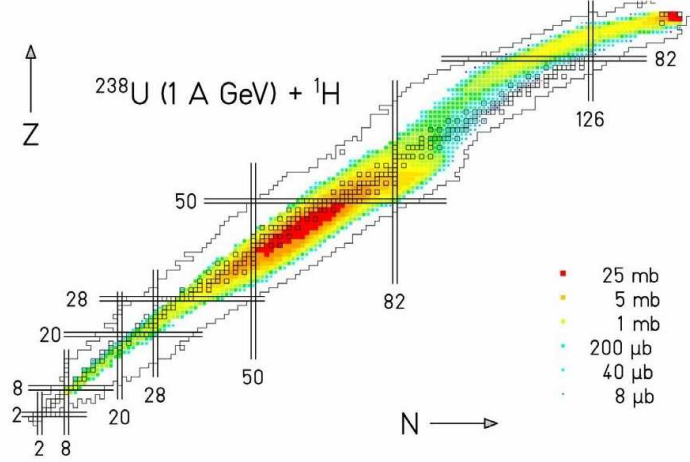


Fig. 3.2. Measured nuclide distribution from the reaction $^{238}\text{U} (1 \text{ A GeV}) + ^1\text{H}$ [120, 121, 122, 123].

fission channel. Relatively easy production of proton-rich nuclei in the compound nucleus reactions can be in principle utilized for formation of secondary beams, however the main obstacle is the limited target thickness and high thermal losses per volume, and thus only some target materials can be considered, what would limit the range of possible secondary beams.

Unlike the compound nucleus reactions, spallation reactions of high energy proton beam with thick target allow to use the rather high intensities of the primary beam. Strictly, this type of reactions is not a nucleus-nucleus collision, however it is mentioned here, since it can eventually allow studies of nucleus-nucleus collisions, initiated by the secondary heavy ion beams. Typically, two different types of nuclear reactions are exploited for the nuclide production in the ISOL facility based on the 1-2 GeV proton beam. In the direct-target option, spallation-evaporation and spallation-fission residues are produced in direct interactions of the primary protons with various feasible target materials (tungsten, lead). In the high-power fission-target option, secondary neutrons from a lead converter target induce fission in uranium or thorium target at excitation energies mostly around or up to a few MeV above the fission barrier. Of these two options, direct-target option appears more suitable for production of proton-rich nuclei, especially in the region of heavy nuclei. From recent experiments performed at GSI in inverse kinematics [117, 118, 119, 120, 121, 122, 123], there is a good empirical knowledge of the general characteristics of these reactions. Figure 3.2 presents the measured nuclide distributions for 1 GeV proton-induced reactions on ^{238}U , respectively, measured in inverse kinematics [120, 121, 122, 123]. It can be seen that even if the target nucleus is relatively neutron-rich, the projectile-like fragments become quite proton-rich in the actinide and lead region. For production of lighter proton-rich nuclei, other target material, possibly a proton-rich isotope, will be the best option.

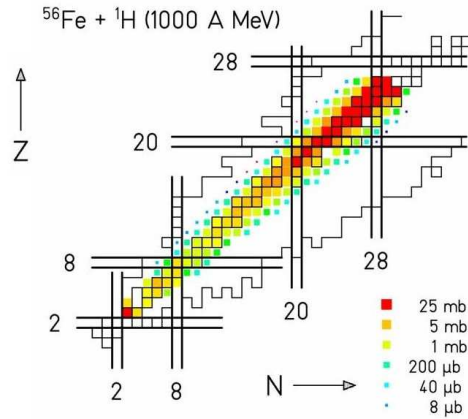


Fig. 3.3. Measured nuclide distribution from the reaction $^{56}\text{Fe} + ^1\text{H}$ (1 A GeV) + ^1H [117, 118].

Production of proton-rich nuclei in fragmentation reactions of heavy-ion beam with, usually, the beryllium target is analogous to spallation reactions in inverse kinematics. In this case, larger yields of proton-rich products can be obtained using heavier target, however such gain is compensated by the loss in the possible beam intensity brought to the target. The beryllium target remains a first choice at the existing RIB facilities at GANIL, at Michigan State University, or at RIKEN.

In conclusion, the production of proton-rich nuclei up to the proton dripline appears to be relatively well understood and also technologically solved. Main progress can be expected in increasing the intensities of the primary beam and in development of necessary target system, and, eventually, in stopping and re-acceleration of the secondary beam.

3.2 Production of neutron-rich nuclei

Main difficulty in production of neutron-rich nuclei consists in circumstance that, due to the lack of electric charge and thus missing Coulomb barrier, the emission of neutrons becomes the most effective de-excitation mode of the excited nuclei, produced in nuclear reactions. Intense neutron emission explains the relative ease of the production of proton rich nuclei. To produce neutron-rich nuclei, the excitation energy, obtained during the nuclear reaction, must be relatively low and thus neutron-rich nuclei will be preferably produced in the so-called "cold" processes with minimum neutron loss.

The spallation or fragmentation reactions (former in normal and latter in inverse kinematics), the most often exploited option for production of radioactive beams at present, offer possibilities for production of neutron-rich nuclei mostly close to the initial heavy target or projectile, respectively. This is documented in Figures 3.2, 3.3, and 3.4, for spallation/fragmentation of nuclei ^{56}Fe , ^{136}Xe , and ^{238}U . Besides spallation/fragmentation close to the heavy beam/target, neutron-rich nuclei can be produced in fission of heavy beam/target, as documented in Figure 3.2. This

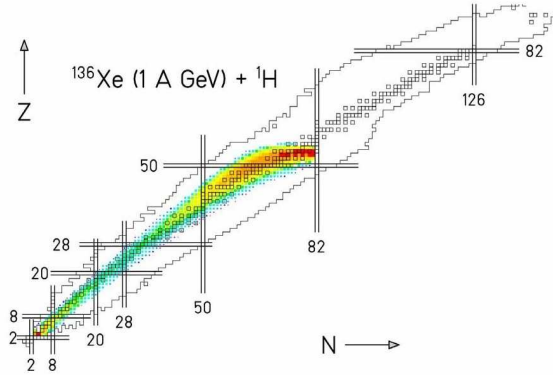


Fig. 3.4. Measured nuclide distribution from the reaction ^{136}Xe (1 A GeV) + ^1H [119].

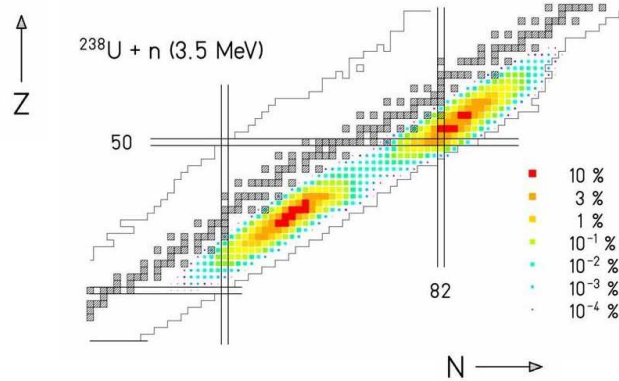


Fig. 3.5. Nuclide distribution of fission products from the neutron-induced fission of ^{238}U for a fixed neutron energy of $E_n = 3.5$ MeV, calculated with the nuclear-reaction code ABRABLA. The color code gives the yields in percent.

option was used intensely in GSI Darmstadt and now in RIKEN. In addition to fission, following spallation/fragmentation, it is possible to consider the low energy fission, induced by thermalized neutrons, obtained by the proton beam hitting the lead converter. Nuclide distributions, produced in neutron-induced fission of ^{238}U at the typical excitation energy of 2 MeV above the fission barrier (corresponding to the fission of ^{238}U induced by 3.5 MeV neutrons) is shown in Figure 3.5 as calculated with the ABRABLA code [64, 89, 90, 91]. From comparison of Figures 3.2 and 3.5 it is obvious that the low-energy fission leads to more neutron-rich products, at the expense that the range of products is more limited. Fission, following spallation/fragmentation, is thus a plausible solution for production of medium-mass neutron-rich nuclei. The open question is, in

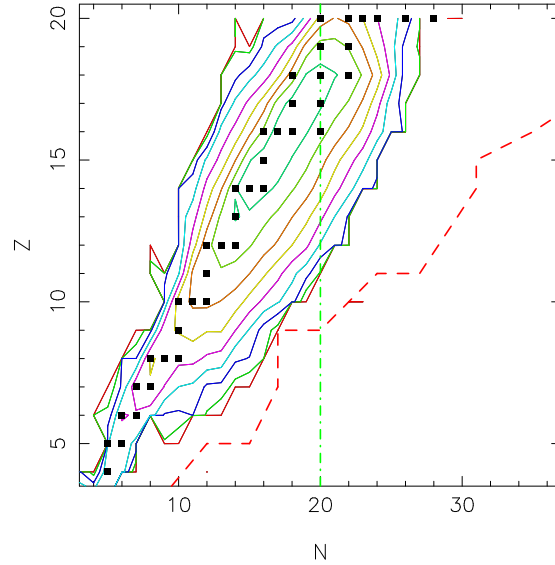


Fig. 3.6. Estimated cross sections for reaction $^{40}\text{Ar}+^{238}\text{U}$ at energy 16 MeV per nucleon. Dashed line represents neutron dripline and vertical dash-dotted line represents the closed neutron shell $N=20$. Symbols represent stable nuclei. Contours are plotted with density two contours per order of magnitude.

which way the more neutron-rich nuclei can be produced.

As demonstrated in the recent works [41, 44, 47, 51, 52], nucleus-nucleus collisions at intermediate energies 15 - 25 A MeV seem to offer relatively favorable conditions for production of neutron-rich nuclei. Reactions of heavy ions at these energies can lead to production of sufficiently cold products, and interesting neutron-rich nuclei can be produced after exchange of sufficient number of neutrons. Fig. 3.6 shows an example of estimated cross sections for reaction $^{40}\text{Ar}+^{238}\text{U}$ at energy 16 MeV per nucleon. Dashed line represents neutron dripline and vertical line represents the closed neutron shell $N=20$. Symbols represent stable nuclei. The cross sections were obtained using model calculations, reproducing the nucleon-exchange reactions at energies 10-50 MeV per nucleon [41, 47], as shown in the section 2.2. Contours are plotted with density of two contours per order of magnitude. It is apparent that the production cross sections of neutron-rich nuclei are rather high, extending even to the drip-line in this region of relatively light nuclei. Of course, to separate such products one needs, as in the case of compound nucleus reactions, an ion-optic separator. Suitable separator will need wide angular and momentum acceptance and its design must allow easy installation of variable detector setups. Production cross sections, shown in Fig. 3.6, were obtained after selection for spectrometer acceptance extending to 10 degrees. Lowest estimated cross sections correspond to 0.5 microbarns, which after assuming the initial beam intensity of 100 pA and target thickness 50 mg/cm² leads to expected production around 10 nuclei per second. Fig. 3.6 thus shows that for light nuclei up to neon one can expect interesting production of the neutron-rich nuclei up to the dripline, which can be identified using the suitable spectrometer and used for coincidence measurement.

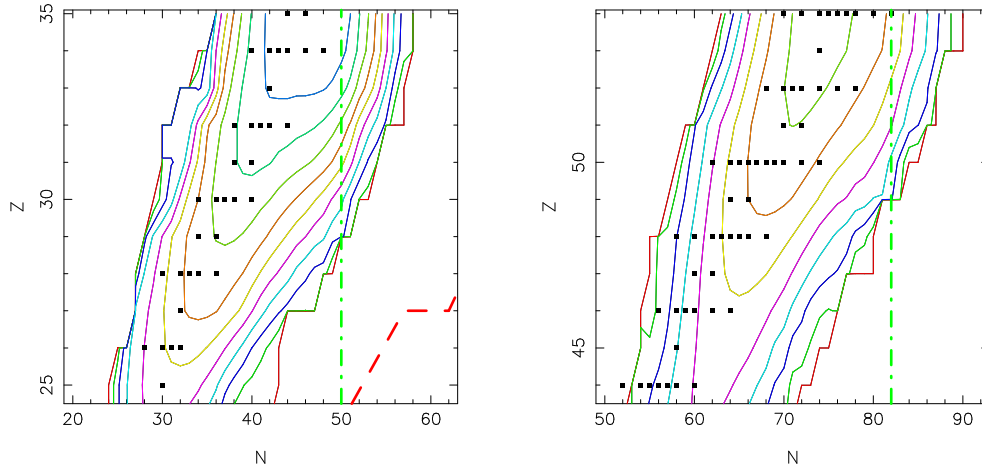


Fig. 3.7. Estimated cross sections for heavier neutron-rich nuclei produced in symmetric reactions $^{86}\text{Kr}+^{90}\text{Zr}$ at energy 8.5 MeV per nucleon (left) and $^{136}\text{Xe}+^{124}\text{Sn}$ at energy 7 MeV per nucleon (right). Lines and symbols have identical meaning as in Fig. 3.6.

Fig. 3.7 shows estimated cross sections for heavier neutron-rich nuclei produced in symmetric reactions $^{86}\text{Kr}+^{90}\text{Zr}$ at energy 8.5 MeV per nucleon (left) and $^{136}\text{Xe}+^{124}\text{Sn}$ at energy 7 MeV per nucleon (right). Comparison of model calculations with existing data at energies below 10 MeV per nucleon showed that production of neutron-rich nuclei can be even more intense, due to effect of diffuse surface in the window (neck) region, not accounted in the model [33]. Low limit of estimated cross sections corresponds to rates ranging from several nuclei per second to one nucleus per several seconds. In these cases dripline is not reached (it will not be achieved even in the new generation of planned exotic beam facilities), however the neutron-rich nuclei are produced in the vicinity of neutron shells $N=50,82$ almost up to the doubly magic nuclei ^{78}Ni and ^{132}Sn . Properties of these nuclei are interesting for studies of nuclear structure and nuclear astrophysics.

It thus appears that nucleus-nucleus collisions at low and intermediate energies can be in principle competitive to other options. In order to verify such possibility, a comparison of various options of production of the exotic nuclei was carried out as a part of the EU 6FP project EURISOL Design Study [125]. Production cross section estimates for nuclear reactions around the Fermi energy were shown to be competitive in comparison to estimates for fragmentation reactions, in particular for very neutron-rich products. Figure 3.8 shows a comparison of the production of element Zr and below. The experimental spallation cross sections for the reaction of 1 GeV protons with ^{238}U [124] is represented by symbols and solid lines, representing Gaussian fits of the experimental mass distributions. The estimates of production cross sections in fragmentation of stable nuclei, obtained using EPAX [46] by optimization for each nucleus separately are represented by dotted lines. The production cross sections for the reactions of $^{86}\text{Kr}, ^{82}\text{Se}+^{64}\text{Ni}$ at 25 A MeV, were calculated using the PE+DIT/ICF+SMM framework [41,71] (dashed and dash-dotted lines), described in the previous sections. One can see that the estimated optimum fragmentation

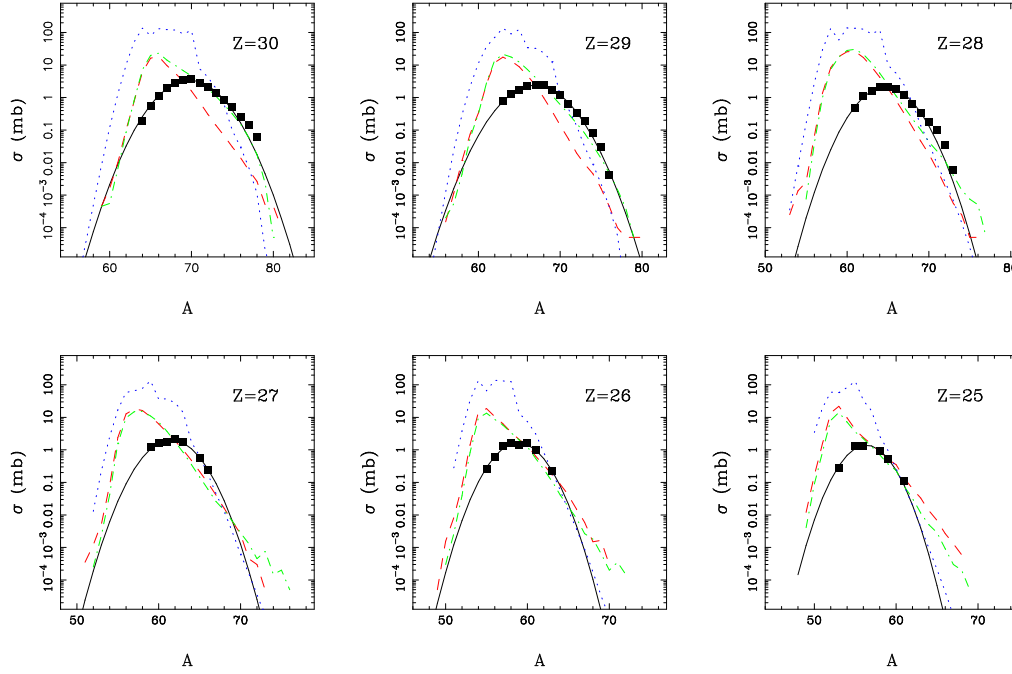


Fig. 3.8. Production cross sections of isotopes of Zr and elements below. Symbols - experimental data for reaction of 1 GeV protons with ^{238}U [124], solid lines - Gaussian fits of experimental mass distributions, dotted lines - estimates of production cross sections in fragmentation of stable nuclei, obtained using EPAX [46] by optimization for each nucleus separately, dashed and dash-dotted lines - production cross sections for reactions of ^{86}Kr , $^{82}\text{Se}+^{64}\text{Ni}$ at 25 AMeV, calculated using the PE+DIT/ICF+SMM simulation.

cross sections essentially follow the experimental trend as described by the Gaussian fits. On the other hand, the production cross sections in the reactions of ^{86}Kr , $^{82}\text{Se}+^{64}\text{Ni}$ at 25 MeV appear to dramatically overshoot the experimental trend for spallation of ^{238}U , thus indicating that this option can be competitive even despite its limitations on target thickness. In order to explore such excess in cross sections, heavy ion beams of high intensities must be available and new experimental techniques for extraction and formation of secondary beams need to be developed.

One of the promising ways to produce extremely neutron-rich nuclei around the neutron shell $N=82$ is fragmentation of a secondary beam of ^{132}Sn [8]. Nevertheless, based on the measured production rates, one can in principle consider also the reaction in the Fermi-energy domain at energies below 50 AMeV.

The comparison of possible in-target yields for the reaction $^{132}\text{Sn}+^{238}\text{U}$ at 28 AMeV with fragmentation cross section of ^{132}Sn beam with Be target is provided in Fig. 3.9. For the reaction $^{132}\text{Sn}+^{238}\text{U}$ the PE+DIT/ICF+SMM simulation was used (solid histograms), while for the fragmentation of ^{132}Sn beam the code COFRA [94], which is reported to reproduce the experimental cross sections [8], (dashed histograms) was used. For the fragmentation of ^{132}Sn secondary beam an energy 100 AMeV was used, the value foreseen for EURISOL facility [126].

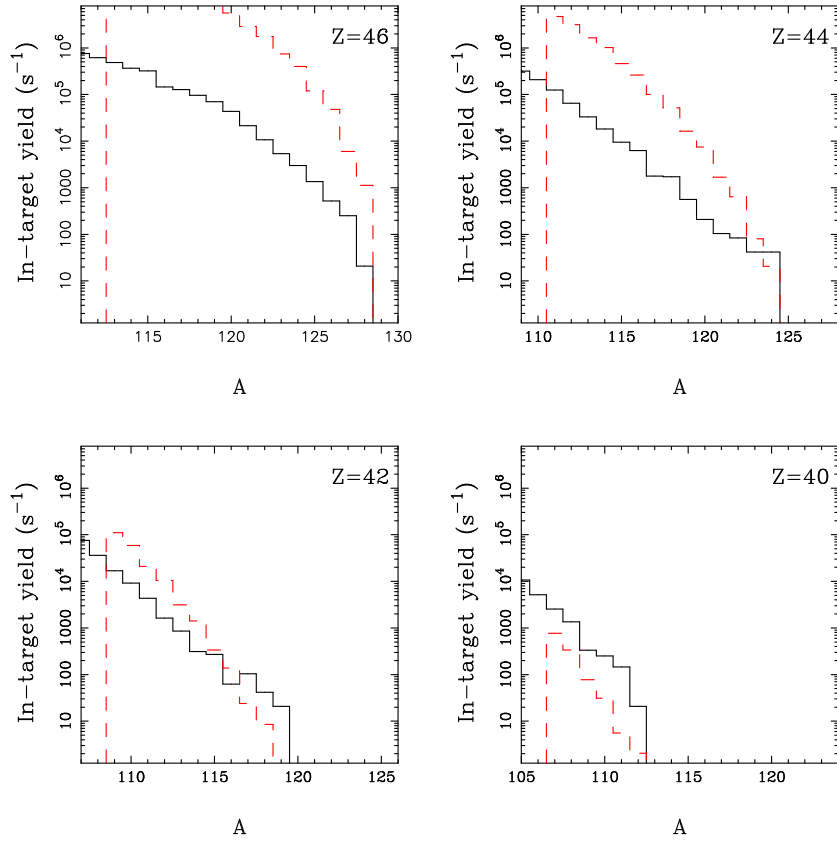


Fig. 3.9. The in-target yields (for the intensity of ^{132}Sn beam 10^{12} s^{-1}). Solid lines - $^{132}\text{Sn}+^{238}\text{U}$ at 28 AMeV, PE+DIT/ICF+SMM simulation, dashed lines - fragmentation of 100 AMeV ^{132}Sn beam with Be target using COFRA [94].

The achievable in-target reaction rate was determined using code AMADEUS [127]. For the reaction $^{132}\text{Sn}+^{238}\text{U}$ at 28 AMeV a target thickness 40 mg/cm^2 was assumed. For the intensity of ^{132}Sn secondary beam a value of 10^{12} s^{-1} was adopted from Eurisol RTD Report [126]. Due to larger target thickness, the in-target yield for fragmentation option calculated using COFRA dominate for elements $Z=44$ and above, for lighter nuclei nevertheless the larger production cross sections in the Fermi-energy domain lead also to larger in-target yields despite relatively thin target and for $Z=40$ such in-target yields exceed the COFRA value. The COFRA values were used for fragmentation since several recent measurements show that EPAX overpredicts the yields of neutron-rich nuclei. For instance, fragmentation experiment with ^{86}Kr beam carried out at MSU [128] showed that experimental fragmentation cross section of neutron-rich Ni isotopes are overpredicted by EPAX by up to two orders of magnitude. The recent experiment on the fragmentation of ^{132}Sn beam [8] demonstrated that predictions of COFRA are favorable for

neutron-rich nuclei. Thus it appears that the reactions in the Fermi-energy domain can become interesting. However, the wide angular distribution of reaction products below 50 AMeV would require a large-acceptance separator with angular coverage up to 10 degrees, wide charge state acceptance and a highly efficient gas-cell in order to form a secondary beam.

In the context of isotopic distributions, sensitivity to isospin degrees of freedom can be explored globally by investigating the ratio of isotopic yields from two processes with different isospin asymmetry, essentially dividing the two isotopic distributions in point-by-point fashion. When employing the statistical model, such a ratio will depend on N and Z as follows

$$R_{21}(N, Z) = Y_2(N, Z)/Y_1(N, Z) = C \exp(\alpha N + \beta Z) \quad (3.1)$$

where, in grand-canonical limit, $\alpha = \Delta\mu_n/T$ and $\beta = \Delta\mu_p/T$, $\Delta\mu_n$ and $\Delta\mu_p$ are the differences in the free neutron and proton chemical potentials of the fragmenting systems. C is an overall normalization constant. An exponential scaling of R_{21} with the isotope neutron and proton numbers was observed experimentally in the multifragmentation data from the reactions of high-energy light particles with massive target nucleus [129, 130] or from the reactions of mass symmetric projectile and target at intermediate energies [131] and such behavior is called isoscaling [131] (the parameters α, β being called isoscaling parameters). Isoscaling behavior was further reported in the heavy residue data [132] and also in fission data [133]. It was shown that the values of isoscaling parameters can be related to symmetry energy [131, 130], to the level of isospin equilibration [132] and to the values of transport coefficients [133].

From the experimental data on production of projectile-like nuclei in reactions induced by ^{86}Kr beam at 25 AMeV, one can construct the yield ratio $R_{21}(N, Z)$ using the convention that index 2 refers to the more neutron-rich system and index 1 to the less neutron-rich one. Fig. 3.10 shows the yield ratios $R_{21}(N, Z)$ as a function of fragment neutron number N for selected isotopes (top panel) and proton number Z for selected isotones (bottom panel) for the reactions of $^{86}\text{Kr}(25\text{AMeV})$ with $^{124,112}\text{Sn}$. The different isotopes and isotones considered are shown by alternating filled and open symbols for clarity. Analogous behavior was observed also in the reactions of $^{86}\text{Kr}(25\text{AMeV})$ with $^{64,58}\text{Ni}$. The positive slopes in the upper panel of Figs. 3.10 indicate that neutron-rich fragments are more efficiently produced, as expected, from the more neutron-rich systems. Similarly, the negative slopes in the bottom panel indicate that proton-rich fragments are more efficiently produced from the more proton-rich systems.

Left panel of Figure 3.11 shows the isoscaling plot of fragments from the reactions of $^{64,58}\text{Ni}$ with ^{208}Pb at beam energies close to 5.5 AMeV. The symbols represent the experimental data for fragments with $Z=27-24$. The lines are exponential fits to the data. The symbols and the lines are shifted up/down by one order of magnitude for each removed/added proton relative to $Z=26$. It is remarkable that isoscaling behavior is preserved even at low energies close to the Coulomb barrier.

If the reaction mechanism is well understood, it can be assumed that it persists even for reactions induced by exotic beams. The isoscaling lines can be extrapolated to the larger or smaller neutron number (or any other measure of isospin asymmetry), and the production cross sections of very exotic species can be predicted using the corresponding yields measured (where available) or calculated for less exotic or stable beams. This approach can be a valuable tool in the continued endeavor to produce rare isotopes towards the drip-lines. Nevertheless, additional

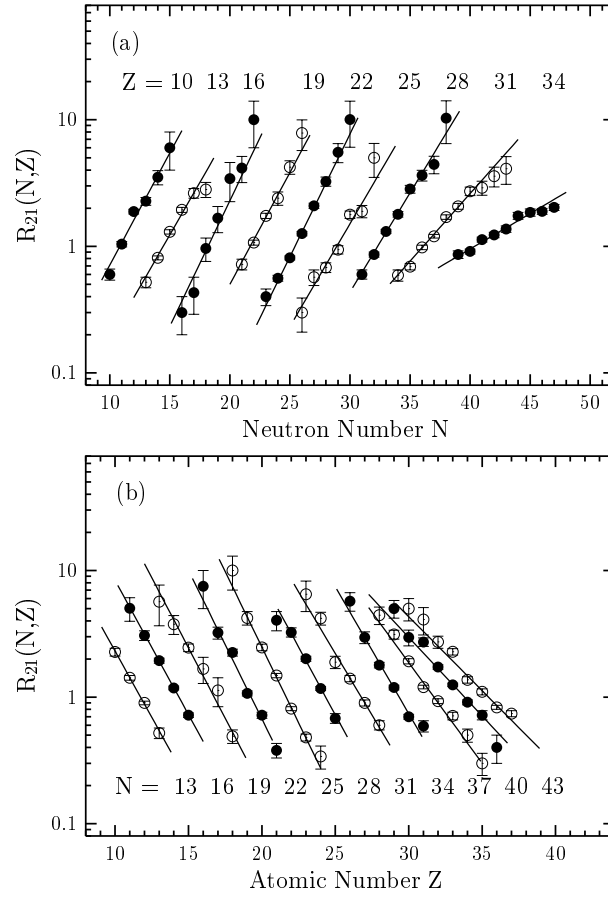


Fig. 3.10. Yield ratios $R_{21}(N, Z) = Y_2(N, Z)/Y_1(N, Z)$ of projectile residues from the reactions of $^{86}\text{Kr}(25\text{AMeV})$ with $^{124,112}\text{Sn}$ (a) with respect to N for the Z 's indicated, and (b) with respect to Z for the N 's indicated. The data are given by alternating filled and open circles, whereas the lines are exponential fits (see text).

systematic work is still needed, especially experiments with a variety of different beams on the same targets. The isoscaling approach is applicable to collisions in which the deep-inelastic transfer mechanism dominates, i.e., in the beam energy range from the Coulomb barrier up to 60–70 AMeV or even more.

The analysis presented above allows to consider the reactions in the Fermi energy domain as a possible source of neutron-rich nuclei for secondary beam formation. A logical continuation of this effort is the investigation of the practical aspects and specifically the possibilities to produce reaction products with optimum mixture and properties for subsequent formation of the secondary beams using the ISOL (IGISOL) method. The kinetic energy of the products will limit the possible target thickness and, due to the wide angular and charge distributions, the in-flight

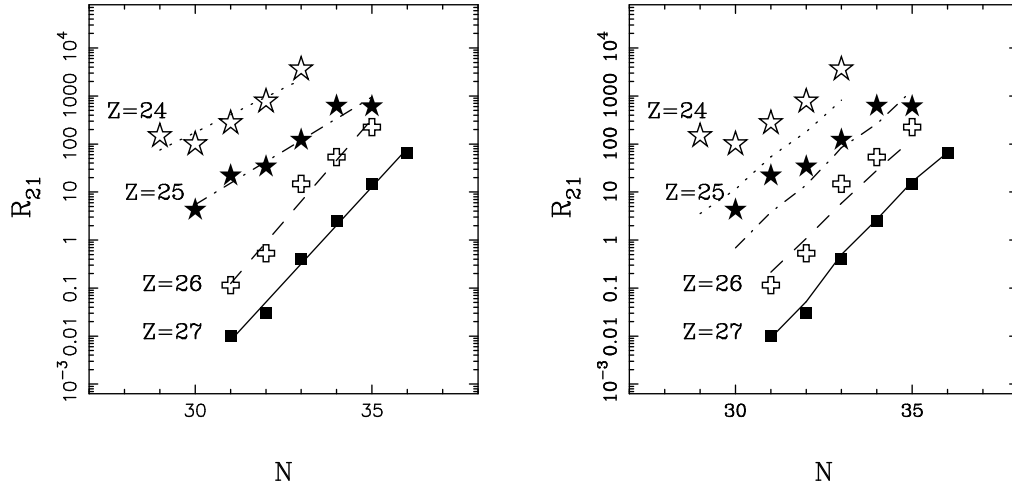


Fig. 3.11. Left panel - Isoscaling plot for fragments from the reactions of $^{64,58}\text{Ni}+^{208}\text{Pb}$ at incident energy around 5.5 AMeV. Symbols: experimental data for fragments with $Z=27-24$. Lines: exponential fits to the data. The symbols and the lines are shifted up/down by one order of magnitude for each removed/added proton relative to $Z=26$. Right panel - symbols as in the left panel, lines represent the result of simulations.

method for the formation of secondary beams would not lead to high quality beams. As relatively suitable appears the possibility to use a version of the ISOL method, where the products will be stopped in the gas volume (gas cell) and subsequently extracted, ionized and formed into a beam. Such a solution is in principle verified and practically used to form secondary beams of the fission products or products of fragmentation reactions [134, 135].

One additional goal of further development is to explore a solution for the optimum target setup and subsequent separation and modification of the properties of the reaction products for further use as secondary beams. It will be necessary to use the production cross sections of the very neutron-rich nuclei in reactions at beam energies around the Fermi energy, depending on the beam energy and emission angle, as an input for the target simulation, specifically for the optimization of the yields of desired products while preserving the properties allowing their subsequent separation from other products, most notably particles of the scattered beam.

For the subsequent separation a system consisting of a large-bore superconducting solenoid (of typical magnetic field of 5-7 Tesla) can be assumed, along the lines described in [136]. The primary beam will be collected with an on-axis blocker covering the angular range 0 to 2 degrees. The deep inelastic products, along with the elastically scattered beam will pass the solenoid and will be focused into a gas cell after traversing appropriate diagnostic detectors (e.g. PPAC, ionization chamber etc.) and a degrader of appropriate thickness. After that point, the techniques developed in [134, 135] can be applied to extract and form the RIB. In order to increase the flexibility and separation ability of such a system, the option of employing two solenoid magnets will be explored in detail. With a dual solenoid system, additional purification of the RIB mixture can be achieved with appropriate diaphragms and/or degrader at the intermediate focus, in addition

to the possibility of obtaining a good TOF measurement between a PPAC at this location and the PPAC at the final focus. Depending on the reaction of choice, the angular range up to 10 degrees should be adequate to collect the products of interest from heavy-ion reactions in the Fermi energy regime.

3.3 Production of super-heavy nuclei

Around the turn of millennia, the heavy elements up to $Z = 112$ have been synthesized in the so-called "cold fusion" reactions using ^{208}Pb , ^{209}Bi - targets, which are essentially the reactions of complete fusion, where due to strong shell structure of the target the evaporation residues are synthesized in the de-excitation channel with the emission of one neutron (for review see [137, 138]). The experimentalists had to face a steep decrease of the cross sections down to the picobarn level. Interestingly, the same level of the cross sections has been reached in the hot fusion reactions with the emission of 5 neutrons. Considerable effort to this topic has been paid especially in the Flerov Laboratory of Nuclear Reaction at Dubna, investigating the potential of such "hot fusion" as an alternative for cold fusion. Using the kinematic separators, the cross sections of evaporation residue production in the 4-5n channels have been measured for the transfermium nuclei [139]. The measured cross sections were analyzed using statistical model of nuclear deexcitation in the work [140], where a statistical code HIVAP [141] was used for calculations. The level densities have been calculated using the well known Fermi gas model. Of the relevant parameters of the fission channel, the asymptotic level density parameter was identical for the fission and particle evaporation channels ($\tilde{a}_f/\tilde{a}_\nu = 1.$) and the fission barrier has been calculated, according to formula 2.12 as the sum of the liquid drop and shell components, scaled by coefficient C . This formula for the fission barrier in the case of nuclei around closed neutron shell $N = 126$ led to typical values of a coefficient C have been 0.65–0.75 independently on the ratio of macroscopic to shell components of the fission barrier, and a similar behavior could be expected also for transfermium nuclei. The principal difference of transfermium region is that the liquid drop barriers are small comparing to the shell component of the fission barrier (ΔB_f^{Shell}), which was taken from the mass calculation [142]). As a default the Bass potential [143] was used for the calculation of fusion cross section. As an alternative the modified WKB formula with the quasi-gaussian barrier distribution [144] was used. Both calculations gave very similar results. The coefficient C was the only free parameter within the calculations. The optimum values of a parameter C , necessary to reproduce the experimental cross sections, are given in Figure 3.12 as a function of neutron number. One can see that, as expected, the optimum values of C remain stable within $Z = 102$ – 110 . The value of $C = 0.8$ – 0.9 is higher when compared to $N = 126$ region and this difference could be most probably attributed to the differences of the saddle point configurations in both regions.

For the case of Pb-target, similar calculations were carried out. In this case the two different fusion cross section calculations give strongly different results. In the case of Bass potential the 1n channel appears to be deeply subbarrier. In the case of barrier distribution no suppression by interaction barrier could be observed. Some indication on the barrier position could be obtained from the ratio of maximum cross sections of 1n and 2n channels. The available data [145] on cold fusion σ_{1n}/σ_{2n} ratio indicate that the 1n channel is subbarrier in the reaction $^{48}\text{Ca}+^{208}\text{Pb}$, in the reaction $^{50}\text{Ti}+^{208}\text{Pb}$ both channels are of the same magnitude and for the heavier projectiles ^{54}Cr and ^{58}Fe the 1n channel is dominating. Such a tendency indicates that for the heavier projectiles

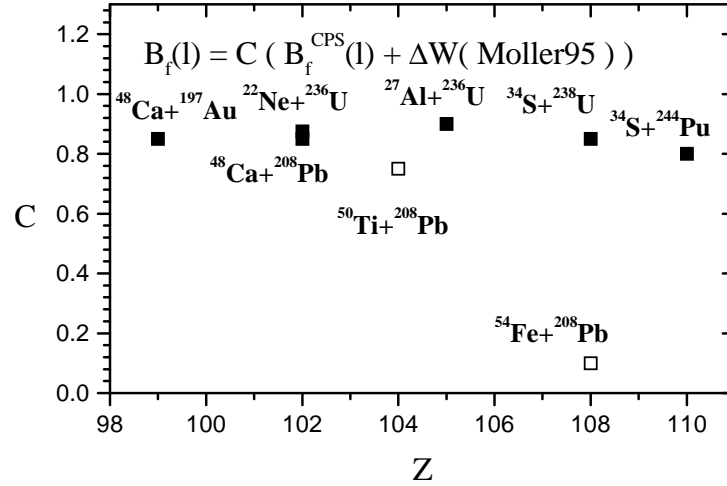


Fig. 3.12. Optimum values of the parameter C , necessary to reproduce the experimental cross sections of hot fusion reactions (solid symbols), as a function of atomic number of residual nuclei. Open symbols - the cold fusion reactions falling out of systematics at $Z > 104$.

the 1n channel is not suppressed due to interaction barrier. For the further calculations the barrier distribution concept has been used with the parameter set ($V_0 = 40$ MeV, $r_0 = 1.11$ fm, $d = 0.75$ fm, $\sigma_{r_0} = 3\%$) which allows to reproduce the maximum cross sections of channels near the fusion barrier for the reactions from $^{16}\text{O} + ^{208}\text{Pb}$, $^{22}\text{Ne} + ^{208}\text{Pb}$ up to $^{48}\text{Ca} + ^{208}\text{Pb}$, $^{50}\text{Ti} + ^{208}\text{Pb}$ and to set right positions of the maximum cross sections for heavier projectiles.

In the Table 3.1 are given the experimental and calculated ($C = 0.85$) values of 1n cross sections and the estimated fusion probability factors. As one may see the fusion probabilities steeply decrease and reach the value of about 10^{-7} for the heaviest projectile ^{70}Zn . This means that, unlike to the hot fusion, in the cold fusion reactions, leading to the evaporation residues with $Z > 104$, the fusion-fission competition to evaporation residue channel is not strong enough and

Tab. 3.1. The fusion probability in the cold fusion reactions with ^{208}Pb target.

Reaction	$\sigma_{1n}(\text{exp})$	$\sigma_{1n}(\text{calc})$	P_{fus}
$^{50}\text{Ti} + ^{208}\text{Pb}$	10 nb	40 nb	0.25
$^{54}\text{Cr} + ^{208}\text{Pb}$	0.5 nb	45 nb	8.8×10^{-3}
$^{58}\text{Fe} + ^{208}\text{Pb}$	60 pb	94 nb	6.3×10^{-4}
$^{62}\text{Ni} + ^{208}\text{Pb}$	3 pb	0.28 μb	1.1×10^{-5}
$^{64}\text{Ni} + ^{208}\text{Pb}$	15 pb	1.38 μb	1.1×10^{-5}
$^{70}\text{Zn} + ^{208}\text{Pb}$	1 pb	4.3 μb	2.3×10^{-7}

another mechanism of fission with shorter timescale could contribute.

To explain the origin of the fusion hindrance, one can in principle assume that during the fusion process the projectile-target system can pass nearby the traditional saddle point configuration. In that case, an additional competition of the immediate fission with the complete fusion may take place and the statistical weights of the compound nucleus and scission configuration, as a final energetically allowed states, may determine the probabilities of the fusion resp. immediate fission. The open question is the statistical weight of the scission point. Also the reaction timescale is relevant for reaction scenario determination.

For the quantitative calculations of competition of fusion and quasifission the following statistical formula for the fusion probability was introduced [140]

$$P_{fus}^{stat} = \frac{\rho(E_{CN}^*)}{\rho(E_{CN}^*) + \rho(E_{sc,eff}^*)} \quad (3.2)$$

where the level density is calculated according to the Fermi-gas formula. The use of such a simple level density approach without shell effects may be under discussion but in the region of $N=126$ it gives a quite good results [146] and it allows to avoid nontrivial calculation of shell correction at the scission point. The estimate of excitation energy in the scission point, based on its expected proportionality to extrapolation of the linearly increasing trend of neutron multiplicity in spontaneous fission with the mass of fissioning nucleus (see Fig. 3.13), can be expressed as

$$E_{sc,eff}^* = [\nu_n^{s.f.}(A_{CN}) + \Delta\nu_n(E_{CN}^*)]E_n \quad (3.3)$$

where $\nu_n^{s.f.}(A_{CN})$ is the linear extrapolation of the available spontaneous fission neutron multiplicity data to a given mass A_{CN} ($\nu_n^{s.f.}(A_{CN}) = 3.316 + 0.0969(A_{CN} - 250)$), $\Delta\nu_n(E_{CN}^*)$ is the additional increase of the post-scission neutron multiplicity at given E_{CN}^* which can be expressed approximately as $\Delta\nu_n(E_{CN}^*) = 0.035E_{CN}^*$, as follows from the available post-scission neutron multiplicity data [147], and E_n is the amount of excitation energy per emitted neutron. The values of E_n were determined for the cold fusion reactions and exhibit the linear dependence on A_{CN}

$$E_n = 3.795 + 0.04(A_{CN} - 260). \quad (3.4)$$

Using obtained set of parameters, the estimations of the cross sections of heavier nuclei are possible for the both cold and hot fusion. An open question is whether such procedure and specifically such a far extrapolation is applicable. However, the results of the studies of fusion-fission of systems up to $Z = 120$ [148] show that the observed fission mode in fusion-fission of such heavy systems remains essentially the same as in the region of uranium, stabilized by the shell-structure in the region of shell closures $Z = 50$ and $N = 82$. Understandingly, for super-heavy system such fission fragment is the lighter one. Such smooth and consistent behavior appears to validate the possibility to extrapolate properties from the region around uranium up to the region of super-heavy nuclei.

The analysis was performed using the modified HIVAP code with the statistical competition of fusion and quasi-fission in the entrance channel [140, 149]. Since the fission barrier of the nuclei with $Z > 100$ is determined by the ground state shell correction of these nuclei, the

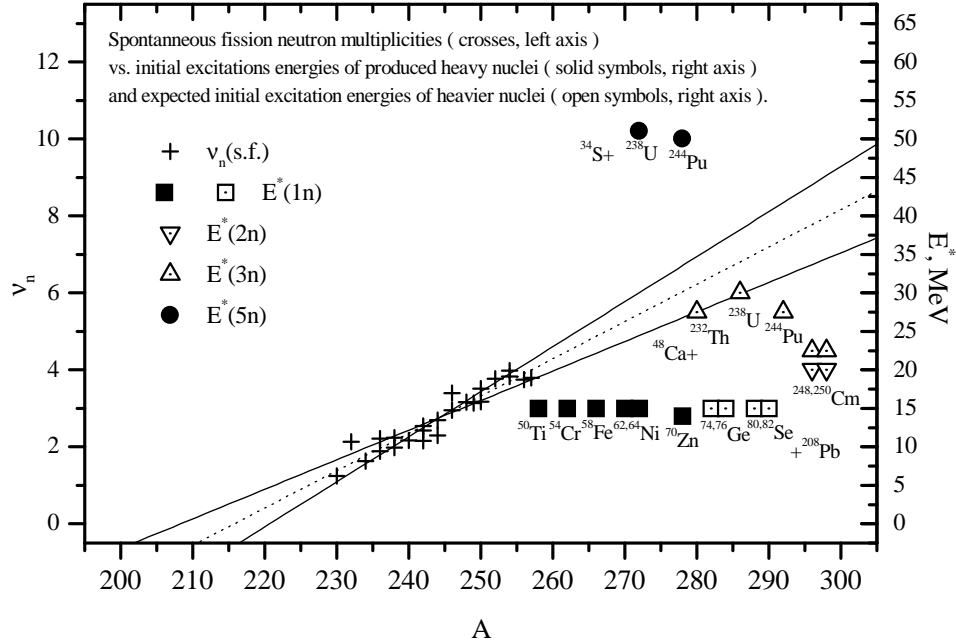


Fig. 3.13. The multiplicity of emitted neutrons (crosses, left abscissa) from spontaneous fission as a function of mass of fissioning system versus the excitation energy at which different heavy nuclei have been synthesized (solid symbols, right abscissa) or could be synthesized (open symbols, right abscissa) in dependence on mass of compound system. The ratio between left and right abscissa is chosen 1:5.

principal problem of such analysis is the availability of reliable predictions of this quantity. This is not yet a solved issue and thus two alternative predictions of Moller [142] and HFB8 [150] are used and compared.

For each reaction, the experimental cross sections were compared to the results of calculations and an optimal scaling factor of the fission barrier was obtained. The results for the synthesized SHE nuclei with $Z = 112-118$ [151, 152, 153, 154, 155, 156, 157] is shown in Fig. 3.14. The experimental cross sections in the 2-5n evaporation channel are shown as stars, squares, crosses, and diamonds, respectively. The results of simulations are shown as corresponding lines (2n - solid line, 3n - dashed line, 4n - dash-dotted line, 5n - dotted line). It can be seen that the simulation is generally capable to reproduce experimental cross sections in the 3-5n evaporation channels. The 2n channel appears to be sub-barrier, for which the WKB fusion model with diffuse barrier is not suitable. The increase of the calculated cross sections in the 4n and especially in the 5n channel, observed for the heaviest system with $Z = 118$ can be an artifact of the extrapolation used to estimate the excitation energy of the scission configuration, based on the neutron multiplicity in the spontaneous fission on nuclei with $Z < 100$. For the system with mass number close to 300 such extrapolation leads to uncertainty of estimation of excitation energy at the scission point close to 10 MeV and thus it is reasonable to restrict the analysis to

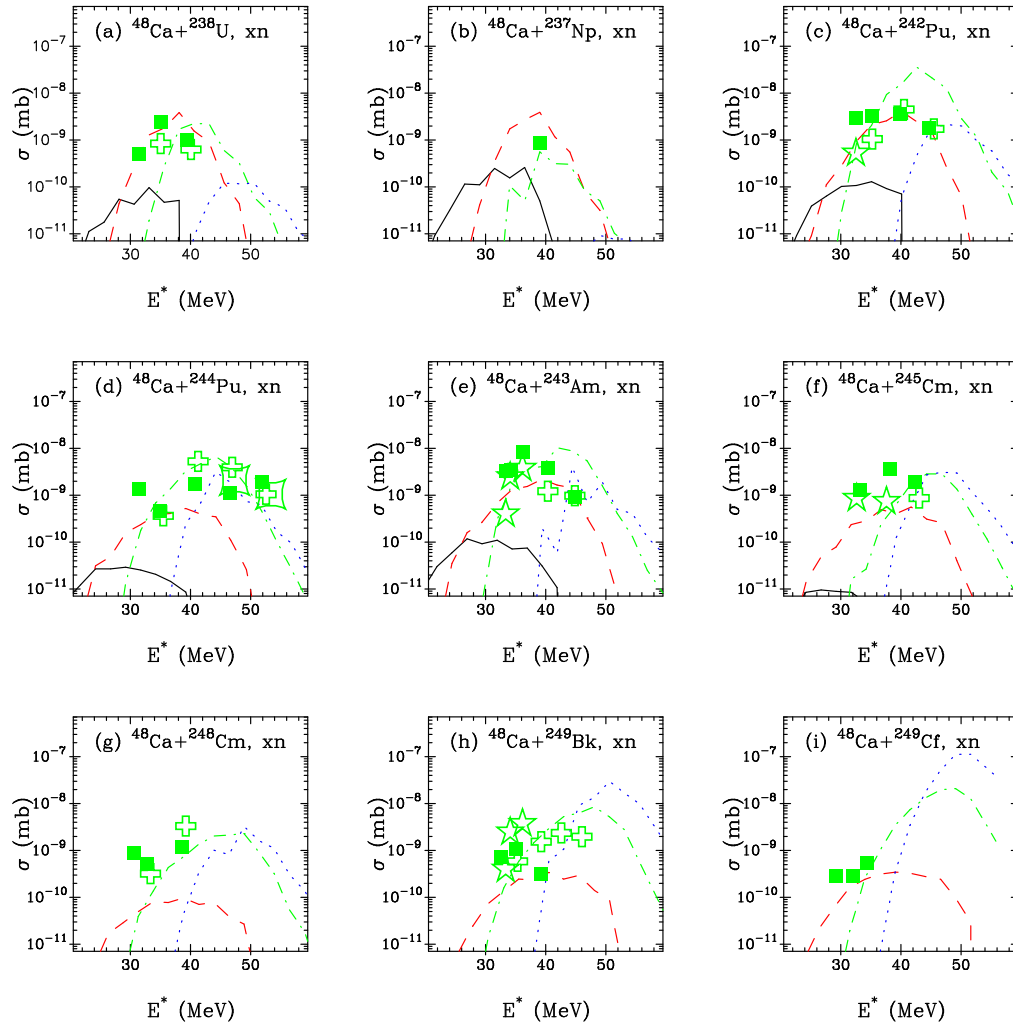


Fig. 3.14. Comparison of experimental (symbols) and calculated (lines) production cross sections of super-heavy elements with $Z=112-118$ produced using the ^{48}Ca beam. The masses and ground state shell corrections of Moller [142] are used. The experimental cross sections in the $2-5n$ evaporation channel are shown as stars, squares, crosses, and diamonds, respectively. The results of simulations are shown as corresponding lines ($2n$ - solid line, $3n$ - dashed line, $4n$ - dash-dotted line, $5n$ - dotted line).

excitation energies lower than 40–45 MeV.

Analogous level of agreement was obtained also when using the alternative set of calculated ground state shell corrections, known as HFB8 [150]. However, there is a difference in the optimal scaling factors, applied to the fission barrier. As shown in Fig. 3.15, the HFB8 prediction appears to be more successful for the nuclei with $Z = 112-116$ (where the dependence is practically constant and the value is close to unity), while for the heaviest nuclei, approaching the

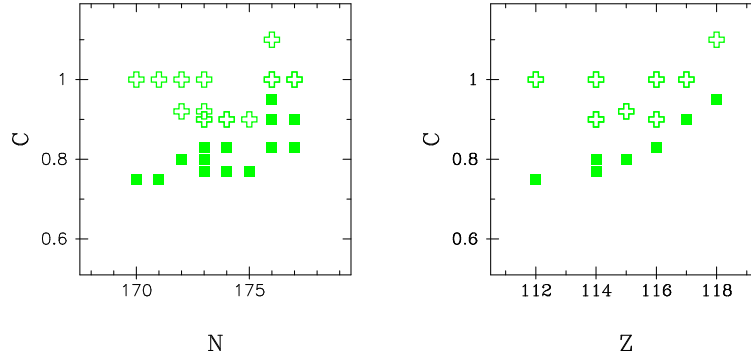


Fig. 3.15. Optimal scaling factors, applied to the fission barrier, plotted as a function of neutron (left) or proton (right) number. Squares shown values for the ground state shell corrections of Moller [142] while crosses show values for the HFB8 prediction [150].

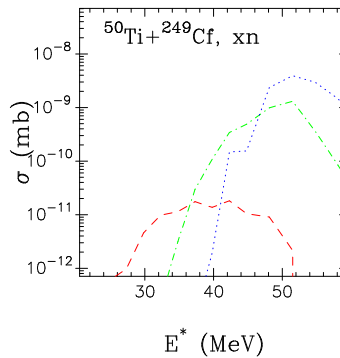


Fig. 3.16. Estimated production cross sections for the heavier system with $Z=120$, produced in the reaction $^{50}\text{Ti}+^{249}\text{Cf}$ (2n - solid line, 3n - dashed line, 4n - dash-dotted line, 5n - dotted line). The prediction of Moller [142] was used for the ground state shell corrections.

predicted spherical neutron shell $N = 180\text{--}184$ and proton shell $Z = 118\text{--}120$, the prediction of Moller et al. appears to be more successful (and its linearly growing trend, especially its dependence on atomic number Z , reaching the unity in this region, is very well pronounced).

Thus, a rather simple and fully statistical procedure appears to lead to surprisingly reasonable results. There still remains question, why such a complex process as a fusion of superheavy nuclei, would be so insensitive to dynamics, which is typically described using theoretical tools such as model of di-nuclear system [158] or Langevin equation [159]. It indeed appears that the competition of fusion and quasi-fission is driven by the available phase-space and no hindrances originating in diabatic dynamics are present.

Based on the above, one can use the predicted of Moller [142] to estimate the production cross sections for the heavier system with $Z = 120$, produced in the reaction $^{50}\text{Ti}+^{249}\text{Cf}$ (see Fig. 3.16). Such prediction suggests that the elements with $Z = 120$ could be produced in the 4n

channel with production cross sections of fractions of picobarn. This prediction is based on the fission barrier scaling parameters used for the synthesis of nuclei with $Z = 117$ – 118 and thus such extrapolation, even when taking into account the probably overestimated cross sections in the $5n$ channels, can be considered as plausible. Thus the production of the element with $Z = 120$ in the reaction $^{50}\text{Ti} + ^{249}\text{Cf}$ should be considered as a serious candidate for synthesis of this element.

In order to synthesize even heavier elements, wholly new approach might be necessary. The increasingly heavy beams will lead to entrance channel mass asymmetries, analogous to observed nuclear fission splits, and such type of fusion in the inverse fission channel appears to be strongly hindered [140]. The possibility to use heavier targets is limited by short lifetimes of such materials. Ultimately, it might be necessary to build a new generation of nuclear reactors with extremely high neutron flux to simulate the conditions during the astrophysical r -process of nucleosynthesis. This, however, may not be available anytime soon.

4 Nuclear equation of state

Atomic nuclei in their ground state can be considered as the drops of extremely dense nucleonic liquid. The nuclear liquid drop model, based on this idea, is capable to describe many properties of nuclei using a relatively simple model assumptions. However, in order to learn more about the properties of such nuclear matter, it is necessary to study its properties away from the normal nuclear (saturation) density. To achieve this, a nuclear system either at lower (sub-saturation) or higher (supra-saturation) density needs to be prepared via nuclear reactions. In the thermodynamical approach, it is possible to describe the properties of nuclear matter by parameterizing their density and temperature dependence. At the saturation density, the stability conditions dictate that a minimum of energy at zero temperature should be located there and also the pressure must vanish to prevent expansion or compression. Additional degree of freedom is the isospin asymmetry, or imbalance in proton and neutron concentrations, which leads to the so-called symmetry energy, which is zero at symmetric matter and raises quadratically with excess of either protons or neutrons. The equation of state of nuclear matter is the global dependence of pressure or energy density on density, temperature and isospin asymmetry and the nucleus-nucleus collisions are a suitable tool to study it at both sub-saturation and supra-saturation densities.

4.1 Nuclear matter

Symmetric nuclear matter, or just nuclear matter, is an idealized system that was derived from the simple model of the atomic nucleus, the liquid-drop model [160]. The properties of nuclear matter at equilibrium (saturation) density are thus inferred from the experimentally observed properties of finite nuclei such as its mass. Unfortunately, the properties of nuclear matter away from saturation density practically cannot be observed directly. They are usually inferred from the evolution of nuclear medium in nuclear reactions such as giant monopole resonance, deep-inelastic transfer or multifragmentation, Also e.g. the thickness of the neutron skin of heavy nuclei such as ^{208}Pb appears to be connected to the properties of the nuclear matter at sub-saturation densities. Below we give a list of main properties of the nuclear matter along with their most probable values.

The short-ranged, strong nuclear interaction is the dominant interaction between nucleons at short distances up to 1–2 fm. It is mostly attractive, which is necessary to form stable nuclei, but repulsive at very short distances (≤ 0.4 fm) [160]. This interaction does not have infinite range and above a certain density the nucleus or nuclear matter will become unstable. This implies that at some density there will be a maximum of binding energy (minimum energy of the system), which is the saturation density. The term saturation stems from the fact that the volume binding energy does not follow quadratic dependence on the mass of nucleus (number of nucleons), as it would be the case if the strong attractive interaction would act at long distance, instead the dependence is linear what implies that each nucleon interacts only with few neighboring nucleons, and so the saturation of binding energy is reached. The saturation density also marks the point at which the pressure in the nuclear system vanishes. For nuclear matter the saturation density is given as $0.15\text{--}0.16\text{ fm}^{-3}$ [160, 161], while the binding energy of nuclear matter is given as $-16.3\text{--}16.0\text{ AMeV}$ in [160, 161]. The other property of nuclear matter at saturation, the compression modulus, defines the curvature of the equation of state at saturation and it can be related to the high density behavior of the equation of state [160]. A *stiff* equation of state

refers to the situation when the system's pressure increases rapidly with an increase in (energy) density. In the case of a *soft* equation of state, the pressure increases more gradually as a function of the (energy) density [160]. The compression modulus K_0 is defined as

$$K_0 \equiv 9 \left[\rho^2 \frac{d^2}{d\rho^2} \left(\frac{\epsilon}{\rho} \right) \right]_{\rho=\rho_0} \quad (4.1)$$

where ϵ is the energy density of the system and the ratio ϵ/ρ expresses the energy per particle. K_0 gives an indication of the stiffness of the equation of state, since it is the measure of the curvature of binding energy at saturation and thus essentially the derivative of the pressure. The value of K_0 is typically estimated to be 230–265 MeV [160, 161]. Stable nuclei with low proton number (Z) prefer a nearly equivalent neutron number (N). As Z increases the (repulsive) Coulomb interaction between the protons also increases. As can be seen on any table of nuclides, stable nuclei diverge from $N = Z$ (isospin symmetric) nuclei to ones with a $N > Z$ as Z increases. This preference for neutrons is described by the symmetry energy. As a measure of the symmetry energy, the symmetry energy coefficient a_{sym} was defined. This coefficient stems from the liquid-drop model of the nucleus and refers to the contribution made by the isospin asymmetry to the energy of the nucleus [162]. In the semi-empirical mass formula (also known as the droplet formula for nuclear masses), a_{sym} is the coefficient of the symmetry contribution (proportional to $I(N - Z)^2/A$) to the mass of the nucleus [160], where $A = N + Z$. This symmetry energy coefficient is given by

$$a_{sym} = \frac{1}{2} \left(\frac{\partial^2 \epsilon}{\partial I^2} \frac{\epsilon}{\rho} \right)_{I=0} \quad \text{with} \quad \left(I \equiv \frac{\rho_n - \rho_p}{\rho} \right) \quad (4.2)$$

where $\rho = \rho_p + \rho_n$ and ρ_p and ρ_n are the proton and neutron densities, respectively. Thus the smaller the value of a_{sym} , the more asymmetric the system tends to be. The value of a_{sym} is estimated to be between 31 and 33 MeV [163, 160, 161].

Large efforts have been undertaken by both the nuclear structure and heavy-ion reaction communities over the last three decades [164] to constrain the EoS of symmetric nuclear matter. Among others, the incompressibility at saturation density $\rho_0 = 0.16 \text{ fm}^{-3}$ has been determined to be $K_0 = 231 \pm 5 \text{ MeV}$ from nuclear giant monopole resonances [165], however also this value depends on model assumptions. The EoS at densities $2\rho_0 < \rho < 5\rho_0$ has been constrained by measurements of collective flows [164, 166] and of sub-threshold kaon production [167, 168] in relativistic nucleus-nucleus collisions. It has been also pointed out [164, 169, 170] that residual uncertainties in the determination of both K_0 and the EoS of symmetric nuclear matter are mainly governed by the uncertainties in density dependence of the symmetry energy, which will be discussed later.

4.2 Hot nuclei and multifragmentation

Hot nucleus is a nucleus, which is highly excited, thermally equilibrated and can be characterized by a temperature. Such nuclei are typically produced in nucleus-nucleus collisions at intermediate and relativistic beam energies. The value of temperature is usually estimated using the apparent compliance of the yield ratio of pairs of isotopes to the grand-canonical picture. The procedure for extraction of the temperature was suggested by Albergo [171]. When expressing the isotopic yield within the equilibrium limit of the grand-canonical ensemble, the simple

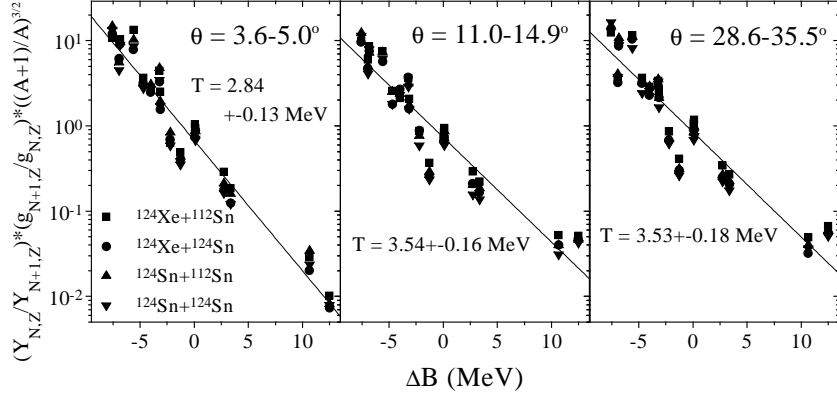


Fig. 4.1. Systematics of corrected isotopic ratios $Y_{N,Z}/Y_{N+1,Z}$ from four reactions plotted against the difference of binding energies [173].

formula is obtained [172]

$$Y(N, Z) = F(V, T) g(N, Z) e^{\frac{B(N, Z) + N\mu_n + Z\mu_p}{T}}. \quad (4.3)$$

The isotopic yield is thus essentially governed by free neutron and proton chemical potentials $\mu_{n,p}$, temperature T and fragment binding energy $B(N, Z)$. The factor $F(V, T)$ encompasses information on the global properties of the fragment partition. The ground state spin degeneracy factor $g(N, Z)$ represents the internal state sum of the fragment, which is restricted to ground state only. In order to extract temperature, a double isotope ratio is constructed [171]

$$\frac{Y(N_1 + 1, Z_1)/Y(N_1, Z_1)}{Y(N_2 + 1, Z_2)/Y(N_2, Z_2)} = \frac{g(N_1 + 1, Z_1)/g(N_1, Z_1)}{g(N_2 + 1, Z_2)/g(N_2, Z_2)} \times \exp \left[\frac{B(N_1 + 1, Z_1) - B(N_1, Z_1) - B(N_2 + 1, Z_2) + B(N_2, Z_2)}{T} \right] \quad (4.4)$$

and the temperature T can be obtained as

$$T = \frac{\Delta B_{1234}}{\ln a \frac{Y(N_1+1, Z_1)/Y(N_1, Z_1)}{Y(N_2+1, Z_2)/Y(N_2, Z_2)}} \quad (4.5)$$

where $a = \frac{g(N_2+1, Z_2)/g(N_2, Z_2)}{g(N_1+1, Z_1)/g(N_1, Z_1)}$ and $\Delta B_{1234} = B(N_1 + 1, Z_1) - B(N_1, Z_1) - B(N_2 + 1, Z_2) + B(N_2, Z_2)$. Thus an estimate of the grand-canonical temperature can be determined using the isotope yields and some of their ground state characteristics.

The formula (4.5) was used extensively in experimental studies [174, 175]. Typically, the temperature determined using various thermometers (sets of isotope yields) exhibited large spread, possibly due to side-feeding from secondary decay. In [173] a graphical method was employed in order to extract the average temperature. The isotopic yield ratios, corrected for ground state spin degeneracy, are plotted as a function of binding energy difference (see Fig. 4.1).

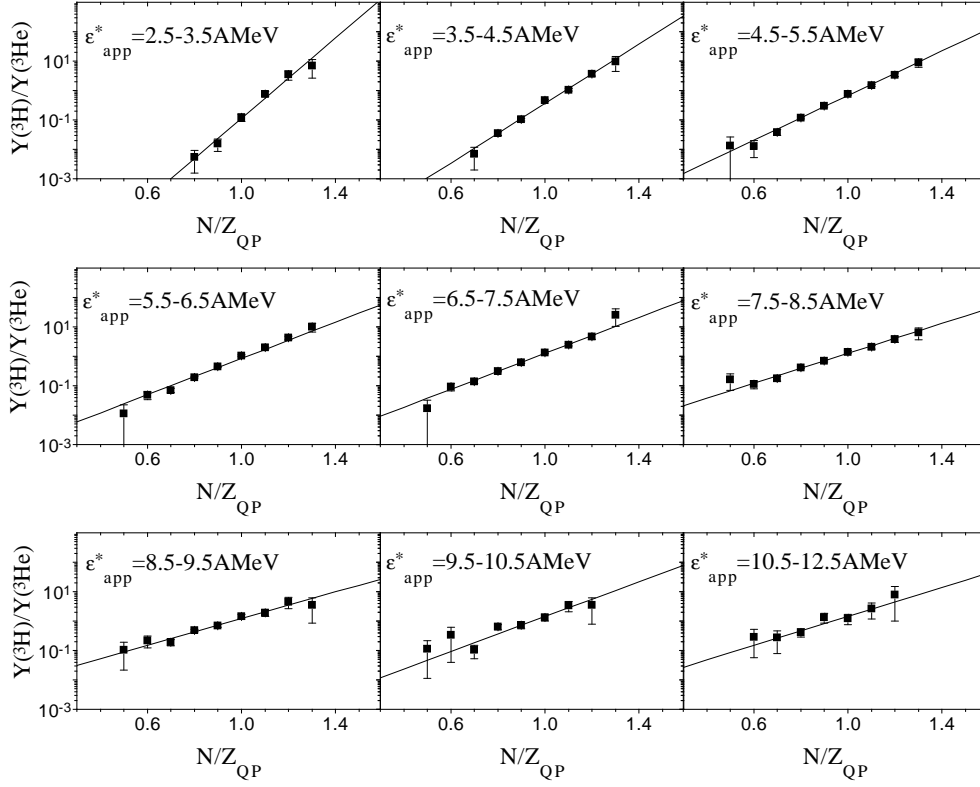


Fig. 4.2. Dependence of the yield ratio $Y(^3\text{H})/Y(^3\text{He})$ on N/Z ratio of the isotopically resolved quasiprojectiles with $Z_{QP} = 12 - 15$ for nine bins of ϵ_{app}^* [176].

The data from four reactions of $^{124}\text{Sn}, ^{124}\text{Xe}$ beams with $^{112,124}\text{Sn}$ targets at 28 A MeV are investigated. Individual double isotope ratio thermometers can be represented (in the logarithmic scale) when connecting the two points corresponding to used isotope ratios by a straight line. The inverse of the slope of such line is then the temperature. When assuming that the effect of side-feeding in the secondary decay is distributed randomly, an average temperature can be obtained by a linear fit of the systematics of all isotopic yield ratios.

An information on the temperature can be obtained also from the slope of dependence of the isobaric yield ratio $Y(^3\text{H})/Y(^3\text{He})$ on neutron to proton ratio of the quasiprojectile N/Z_{QP} . The data from reactions of a ^{28}Si beam with ^{112}Sn and ^{124}Sn targets at 30 and 50 A MeV (see Fig. 4.2) were used [176] and the extracted temperatures compared well with the temperatures obtained using the double isotope ratio thermometer $(^2\text{H}/^3\text{H})/(^3\text{He}/^4\text{He})$. An assumption was employed that the values of chemical potentials can be approximated by the values of separation energies. The reason why such approximation is applicable for hot expanded nuclei can be in the possible interplay of the effect of expansion (reducing absolute values of chemical potentials) and separation of the isospin-asymmetric free nucleon gas from the isospin-symmetric heavier

liquid phase [176], as indicated by observed inhomogeneous isospin distribution among light charged particles and heavier fragments [177].

At excitation energies above 1 AMeV the hot nuclei can evaporate not only nucleons and α -particles (as is common at lower excitation energies of several tens of MeV), but also heavier fragments. In order to describe such fragment emission, the traditional model of compound nucleus decay based on Hauser-Feshbach approximation [66] was extended by Moretto to describe the emission of intermediate mass fragments (IMF) [67]. The emission of such complex fragments is described as a binary split, essentially an asymmetric fission where the IMF is accompanied by a heavy residue. The emission probability is determined by a value of the mass-asymmetric fission barrier height. The model of fission-like binary split describes reasonably well the onset of fragment emission, thus indicating that at the onset the complex fragment emission is a fission-like process [178]. Success of such approach prompted the attempts to describe multifragmentation using the model of Sequential Binary Decay (SBD). Several implementations (e.g. the GEMINI code [50]) have been used extensively for comparisons with experimental multifragmentation data, with reasonable success in description of e.g. inclusive mass and charge distributions. However, as shown earlier, the model of sequential binary decay fails to describe the results of the exclusive measurements at the zero angle [179]. An explanation is suggested by comparison of the model of sequential binary decay to transitional-state model of multifragmentation [180] where even for binary exit channel the number of available degrees of freedom is different. Furthermore, the model of sequential binary decay also fails to reproduce the observed fragment correlations [181].

Simultaneous multifragmentation is a process where the final state consists of multiple fragments which are the remnants of a hot nucleus. Statistical phase-space models of multifragmentation typically assume that the properties of final fragments are determined in the so-called "freeze-out" configuration, where the typical distance of pre-fragments becomes, due to thermal expansion, larger than radius of the short-range nuclear interaction. Main assumption of the statistical phase-space models describing various processes is that a certain stage of the process can be identified where the available phase-space determines the final probability distribution of exit channels. For instance, in statistical description of the fully equilibrated compound nucleus, the probabilities of various evaporation channels are determined by available phase space of the corresponding evaporation residue and the fission probability is determined by available phase space at the saddle-point on top of the fission barrier. In the case of simultaneous multifragmentation, the phase-space is explored for the possible multi-fragment configurations (partitions), typically at the stage where short-range nuclear interaction freezes out and the identities of final fragments are determined. The probabilities of various partitions can be determined statistically, exactly using the micro-canonical ensemble [182], or approximately using the canonical and grand-canonical ensembles [35]. Canonical and grand-canonical approximations typically reduce the mathematical complexity while raising questions on the applicability of such approximations since the nuclei are rather small systems. Detailed discussion of the application of statistical mechanics to small systems can be found in [183].

Here we briefly review the most commonly used phase-space model of simultaneous multifragmentation, the Statistical Model of Multifragmentation (SMM) [35]. The model uses the grand-canonical approximation, the freeze-out volume depends on fragment multiplicity and internal excitation of fragments in the freeze-out configuration is considered, thus producing "hot" fragments. Analogous models with "cold" fragments also exist [182], typically the freeze-

out volume is chosen approximately twice larger than in the case of hot fragments. Yield of fragments with neutron and proton numbers N and Z can be, within grand-canonical approach, characterized by formula [35]:

$$Y(N, Z) = g_{NZ} \frac{V_f}{\lambda_T} A^{3/2} \exp \left[-\frac{F_{NZ}(T, V) - N\mu_n - Z\mu_p}{T} \right] \quad (4.6)$$

where g_{NZ} is the ground state spin degeneracy, V_f is the free volume ($V_f = V - V_0$ where V and V_0 are the volumes at freeze-out and ground state), λ_T is the thermal wavelength, F_{NZ} is the intrinsic free energy of the fragment, μ_n and μ_p are the free neutron and proton chemical potentials, and T is the temperature. The free volume at freeze-out is determined as $V_f = \chi V_0$. The parameter χ is determined as

$$\chi = \left[1 + \frac{d}{r_0 A_0^{1/3}} (M^{1/3} - 1) \right]^3 - 1. \quad (4.7)$$

where M is the fragment multiplicity, d is nuclear diffuseness, A_0 is the mass of the system and r_0 is the nuclear radius parameter. It is essentially a product of the additional fragment surface area and nuclear diffuseness length. The values of χ range from 0.2 to 2. The fragment free energy is at most part determined using the liquid drop model. The component of free energy corresponding to Coulomb interaction is determined using the Wigner-Seitz approximation. The Wigner-Seitz clusterization energy is calculated at volume $V = (1 + \kappa)V_0$. The value of κ can be related to average Coulomb barrier and thus is generally different from χ , which controls the freeze-out of strong interaction. Typical value is $\kappa = 3.5$ which is between the values for closely packed fragments ($\kappa = 2$) and for fission ($\kappa = 5$). The statistical model of multifragmentation was used for extensive comparisons with experimental multifragmentation data, typically obtaining a consistent description of a wide range of experimental observables [35, 78, 179].

As an alternative to two-step reaction scenario, where reaction dynamics is attributed to the early stage of nucleus-nucleus collision while multifragmentation of the hot nucleus is described statistically, the whole process can be described in unified fashion by dynamical theory with explicit time-dependence. In the microscopic time-dependent Hartree-Fock theory [184], an extension of the stationary Hartree-Fock theory used to describe the ground state, the nucleus-nucleus collision is represented by time evolution of the one-body mean field, which defines the collective degrees of freedom of the system. The time-dependent Hartree-Fock theory does exhibit collective behavior which reminds many experimentally observed phenomena [184], it nevertheless does not include two-body dissipation via collisions of nucleons which is supposed to play significant role at energy regimes where the hot nuclei are produced. Two-body interaction can be included in the framework of quantum kinetic theory as represented by the Boltzmann transport equation, which describes the reaction dynamics in terms of both mean-field and two-body dissipation. Various semi-classical methods featuring the concept of pseudo-particle are used to simulate the solution of the Boltzmann transport equation. The most common approximations are Vlasov-Uehling-Uhlenbeck (VUU) [185], Boltzmann-Uehling-Uhlenbeck (BUU) [186], Landau-Vlasov (LV) [187], Boltzmann-Nordheim-Vlasov (BNV) [188] and Quantum Molecular Dynamics (QMD) [189] methods. Results of such simulations typically offer a qualitative description of the main features of reaction dynamics including multifragmentation.

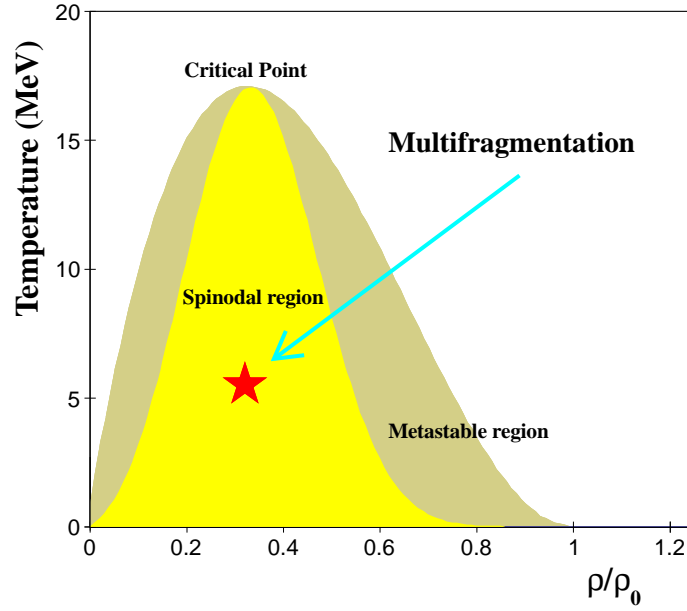


Fig. 4.3. A schematic description of the nuclear liquid-gas phase transition as a mechanism of multifragmentation.

Using the transport theory, the properties of the nuclear equation of state such as nuclear incompressibility and symmetry energy can be investigated phenomenologically.

4.3 Liquid-gas phase transition

Phase-space models of multifragmentation typically explore the properties of final fragments in the freeze-out configuration where nuclear interaction between the fragments does not play a role anymore. The underlying mechanism leading to multifragmentation is nevertheless closely related to properties of the nuclear medium, which can be studied microscopically. Over the recent decades, thermal properties of the nuclear medium were studied theoretically using microscopic approaches such as temperature-dependent Hartree-Fock [190] or relativistic mean-field [191] approximations. The microscopic theory of the nuclear matter predicts a phase transition of the liquid-gas type. Below a critical temperature, the two phases can coexist. The spatial distribution of phases can be expected to develop from vapor bubbles in liquid at high density toward liquid droplets in vapor at low densities [192]. A hot nucleus undergoing multifragmentation can be envisioned as rapidly expanding until it enters the spinodal region (as it is schematically shown in Fig. 4.3). At that stage multifragmentation occurs due to rapidly developing dynamical instabilities. When considering the isospin-asymmetric nuclear matter [191, 193], the phase transition is supposed to lead to separation into a symmetric dense phase and asymmetric dilute phase. It has been discussed in literature [194] to what extent such a phase transition is generated by fluctuations of density or concentration, typically suggesting a coupling of different instability

modes.

The properties of clusters formed in the phase transition can be described by a variety of random cluster models. Simple model of clusterization was proposed by Fisher [195], where the liquid drop expansion of the Gibbs free energy leads to the mass distribution of clusters

$$P(A) \propto A^{-\tau} \exp \left[-b(T)A^{2/3} \right] \quad (4.8)$$

where the surface term $b(T) = 4\pi r_0^2 \sigma(T)/T$ decreases monotonically toward zero as temperature approaches critical temperature T_c . At critical temperature the mass distribution becomes a power law with critical exponent τ . Similar properties are obtained using percolation models, lattice models and cellular model of fragmentation (an extensive overview of these models in the context of multifragmentation can be found in [196], sections 4., 5.).

Calculations based on the microscopic nuclear theory [191, 193] suggest that nuclear matter undergoes liquid-gas phase transition which is of the first order, the density difference between phases being the order parameter. Similar conclusions can be obtained also in the context of SMM [197]. However, the phase transition in the percolation models is of the second order and lattice models such as Ising model [198] exhibit a complex phase diagram with both first and second order phase transitions. Furthermore, since theory of nuclear phase transitions is formulated for infinite systems while the experiments investigate multifragmentation of finite nuclei, it is necessary to assess the effect of finite size. As discussed in [196], the critical behavior observed in random-cluster models can be related to scaling properties and self-similarity of the system at different scales, what suggests that observed properties of finite system represent the properties of infinite media. On the other hand, finiteness constraints of small systems can lead to a behavior analogous to criticality [196]. Obviously, for any experimental observation the effect of finite size should be understood.

In the work [200], thermodynamical properties of the quasi-projectiles undergoing statistical multifragmentation [78, 177, 176, 199] were investigated in order to reveal possible signals of the phase transition. The difference of isovector chemical potential in two reactions $\Delta(\mu_n - \mu_p)$ was estimated using the isoscaling analysis [199], by constructing the observable $\beta'T$ (see Fig. 4.4a), where isoscaling parameter β' obtained by fitting the exponential dependence of the ratio R_{21} on projection of isospin N-Z. The temperature of the hot system was obtained using ^2H , $^3\text{H}/^3\text{He}$, ^4He double isotope ratio thermometer (see Fig. 4.4b). A horizontal line in Fig. 4.4a represents an estimate of the zero temperature value of $\Delta(\mu_n - \mu_p)$ by the proton and neutron separation energies ($\mu_{p,n} \approx -S_{p,n}$) of reconstructed quasi-projectiles, using their known N/Z ratio and a correction for neutron emission from back-tracing of DIT/SMM simulations [78]. The zero temperature estimates of $\Delta(\mu_n - \mu_p)$ for all excitation energy bins are consistent with the horizontal line. The experimental dependence of $\Delta(\mu_n - \mu_p)$ at low excitation energies is consistent with a trend of decrease caused by expansion of the homogeneous hot source (shown as dashed line), at 4 AMeV it deviates from the trend of homogeneous system and the zero temperature value is again approached at 6-7 AMeV. The trend of $\Delta(\mu_n - \mu_p)$ for homogeneous system was obtained assuming $\rho^{2/3}$ -dependence of the Fermi energy and using the estimate of free volume by formula (52) of [35]. The turning-point at 4 AMeV can be understood as a signal of the onset of phase coexistence since chemical separation into an isospin symmetric heavy fraction and an isospin asymmetric nucleon gas leads to increase of $\mu_n - \mu_p$ of the dilute phase (free nucleon gas). The onset of chemical separation is correlated to the onset of the plateau

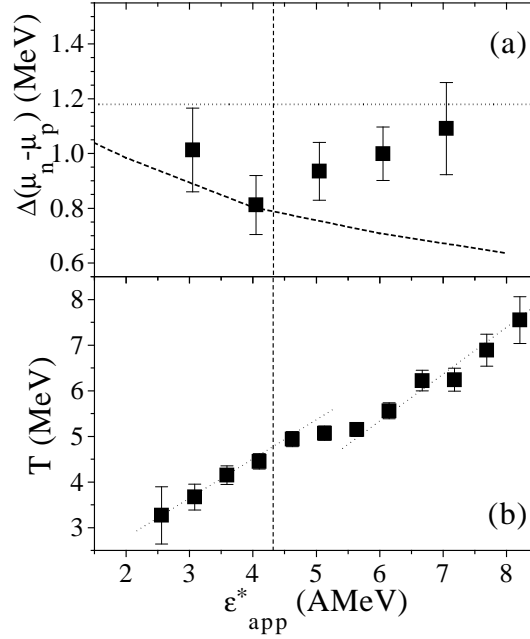


Fig. 4.4. (a) The dependence of observable $\beta'T = \Delta(\mu_n - \mu_p)$ on apparent excitation energy of the quasiprojectile [199] (full squares). Horizontal line shows estimate of $\beta'T$ obtained when assuming $\mu_{p,n} \approx -S_{p,n}$. Dashed curve represents the expected trend for homogeneous system. (b) Corresponding caloric curve [176]. Vertical line indicates the position of turning point.

in the caloric curve in Fig. 4.4b, thus signaling that chemical separation is accompanied by a latent heat. Such a behavior can be expected in the first-order phase transition. The dotted lines in Fig. 4.4b indicate discontinuity in the heat capacity.

Several experimental signals of the first-order phase transition were reported, such as negative micro-canonical heat capacity [201], characterized by abnormal kinetic energy fluctuation, and the "fossil" signal of spinodal decomposition [202], characterized by abnormal production of equally sized fragments. The isospin-asymmetry of the fragments is not explored in such investigations. The behavior in Fig. 4.4 relates the signal of chemical separation to the plateau of the caloric curve, thus providing a signal of isospin-asymmetric first-order phase transition. Further support for such conclusion can be deduced from the inhomogeneous distribution of isospin-asymmetry [177] among dense and dilute phases represented by light charged particles (LCPs) and intermediate mass fragments (IMFs), respectively. The effect is strongly dependent on the N/Z ratio of the quasiprojectile. So are multiplicities of LCPs and IMFs which further indicate that with increasing isospin-asymmetry of the quasiprojectile the dilute phase becomes more isospin-asymmetric and abundant. The estimated density at the turning point in Fig. 4.4a is consistent with theoretical estimates of the position and shape of the spinodal contour, typically at almost constant total density $0.6\rho_0$ in a wide range of asymmetries [194]. Thus, inside

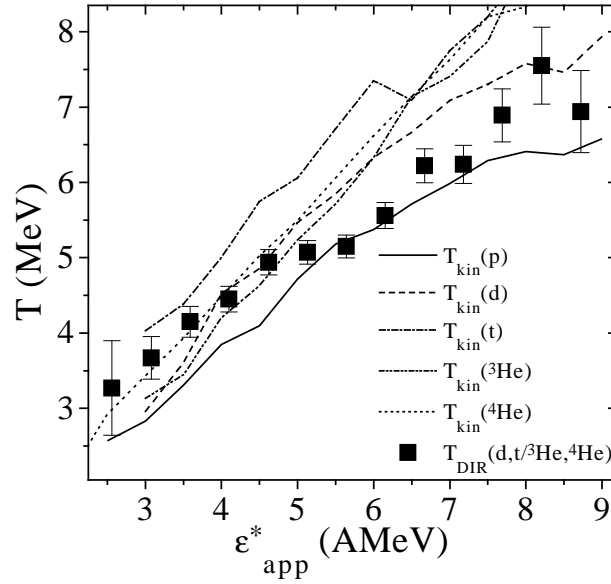


Fig. 4.5. Comparison of temperature obtained using the double isotope ratio thermometer $d,t/{}^3\text{He}, {}^4\text{He}$ [176] with kinematic temperatures of $p,d,t,{}^3\text{He}, {}^4\text{He}$ in the quasi-projectile frame.

the spinodal region the homogeneous nuclear medium is quickly replaced by both isospin and spatially inhomogeneous system. Such a conclusion is further supported by a comparison of the temperature obtained using the double isotope ratio thermometer $d,t/{}^3\text{He}, {}^4\text{He}$ [176] with kinematic temperatures of $p,d,t,{}^3\text{He}, {}^4\text{He}$ obtained from Maxwellian fits of the kinetic energy spectra in the quasiprojectile frame (see Fig. 4.5). While at low excitation energies the double isotope ratio temperature represents essentially an average of the kinematic temperatures of individual species, in the plateau region a transition occurs to the regime where the double isotope ratio temperature represents the kinematic temperature of protons (and possibly of the nucleon gas). Such a transition, just above the turning-point where the isovector part of chemical potential deviates from the trend of homogeneous system (as shown in Fig. 4.4), suggests that the isotopic composition of fragments is in equilibrium with the free nucleon gas what is a basic assumption used in grand-canonical models such as SMM [35]. Higher values of kinematic temperatures of $d,t,{}^3\text{He}, {}^4\text{He}$ indicate that the clusters are created prior to such equilibration (possibly by spinodal decomposition). On the other hand, the low energy behavior can be explained by an assumption that the isotopic composition is determined at the instant when clusters are emitted what is in good agreement with our understanding of de-excitation of the compound nucleus. The two different values of heat capacities in low- and high-energy parts of the caloric curve, suggested in Fig. 4.4b, can thus be understood as representing a homogeneous nuclear liquid and an isospin-asymmetric free nucleon gas, respectively. For the quasiprojectiles with $A = 20\text{--}30$ the finite-size effect can play role and thus similar analysis for heavier sources is necessary in order to establish a link to the phase transition in the isospin-asymmetric nuclear matter at

sub-saturation densities. It may be however noted that theoretical studies of small systems [183] suggest that van der Waals-like loops observed in infinite systems are affected in transition to finite system only by small terms and thus the conclusions for finite systems can be applicable also for infinite case.

One of the goals of the work [74] was to verify the behavior observed in the reaction $^{28}\text{Si} + ^{112,124}\text{Sn}$. Of special interest was the verification of the signal of the liquid-gas phase transition, obtained using isoscaling analysis in the earlier work [199]. Practically isotropic emission is observed (as documented in Fig.2.19) which implies the statistical multifragmentation of the hot projectile-like nucleus. As in the work [199], the isoscaling analysis was performed also for the reactions $^{40,48}\text{Ca} + ^{27}\text{Al}$ at 45 AMeV. The observed isoscaling behavior is quite regular and the value of the isoscaling parameter (slope) decreases with excitation energy, in agreement with the previous experiment [199] and other experiments reported in the literature. Also the yield ratios of mirror nuclei measured in the reaction $^{48}\text{Ca} + ^{27}\text{Al}$ at 45 AMeV exhibit exponential scaling with the quasiprojectile N/Z , with identical slopes for all ratios within each of the excitation energy bins. The slope decreases with increasing excitation energy in an analogous way as in the reactions $^{28}\text{Si} + ^{112,124}\text{Sn}$ [176]. The observed grand-canonical scaling provides further evidence that statistical multifragmentation is a dominant mode of de-excitation also in this case.

In order to estimate the evolution of the chemical potential, as in the earlier work [199], it was necessary to estimate the system temperature. Fig. 4.6a shows the caloric curve obtained for the selected fully resolved data with $Z \geq 21$ using the double isotope ratio thermometer $d,t^{3,4}\text{He}$ (squares). Furthermore, Fig. 4.6a shows the comparison of the double isotope ratio thermometer $d,t^{3,4}\text{He}$ to global temperature from the slopes of ΔB dependences in (triangles, obtained in similar way as temperature in Fig. 4.1) and to proton kinematic (slope) temperature (line). One can see that, unlike the work [200], there is no clear correspondence of the slope temperature to the double isotope ratio thermometers. Thus one needs to establish to what extent the double isotope ratio temperature of the two thermometers represents the multifragmentation temperature. When comparing the $d,t^{3,4}\text{He}$ temperature observed in the reactions $^{40,48}\text{Ca} + ^{27}\text{Al}$ at 45 AMeV to the earlier results for the reactions $^{28}\text{Si} + ^{112,124}\text{Sn}$ [176, 200], both caloric curves are consistent and thus possibly represent general properties of the multifragmenting system. On the other hand, a similar comparison for the proton kinetic temperature shows that in the heavier system it dropped considerably, what can be explained by the onset of intense secondary emission of protons in the heavier system. In the reactions $^{40,48}\text{Ca} + ^{27}\text{Al}$ at 45 AMeV, proton kinematic temperature is consistent with the global temperature from the slopes of ΔB dependences and thus the latter also appears to be consistent to secondary emission. Thus the mass range $A = 40\text{--}50$ appears to represent an upper limit where the effect of secondary emission can be disentangled.

It is remarkable to note, that there is a good correspondence between the global isotope ratio temperature and proton kinematic temperature. Both curves are relatively flat above 4 AMeV, which can be possibly interpreted as a long plateau. However, comparison with the lighter hot system in ref. [199] shows that the value of the plateau temperature is much lower than it can be expected in multifragmentation. Especially in the case of thermometers using proton multiplicity and proton kinematic temperature such low temperature with flat behavior may be caused by increased influence of secondary de-excitation via nucleon (proton) emission. Such a mode is not dominant in the lighter system of ref. [199], where the Fermi decay, analogous to multifragmentation, dominates [35]. Thus the proton kinematic temperature for the lighter system represents the earlier de-excitation stage, as is documented by higher values of the temperature [200] than

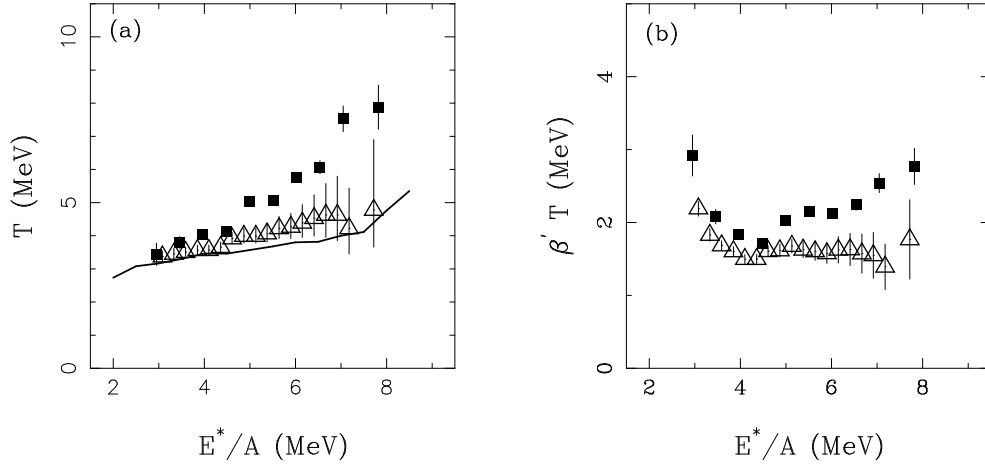


Fig. 4.6. (a) Caloric curve obtained using global temperature from the slopes of ΔB dependences (triangles) along with the caloric curves obtained using the double isotope ratio thermometer $d,t^{3,4}\text{He}$ (squares) and proton slope temperatures (line). (b) Resulting values of $\beta' T$ obtained using the global (triangles) and $d,t^{3,4}\text{He}$ (squares) temperatures.

in the present case.

In the macrocanonical limit, the product of the temperature T and isoscaling parameter β' (obtained by fitting the exponential dependence of the ratio R_{21} on projection of isospin $N-Z$), corresponds to the value of the isovector part of the chemical potential. The resulting values of $\beta' T$ are shown in Fig. 4.6b for the $d,t^{3,4}\text{He}$ thermometer (squares) and the global isotope ratio temperature (triangles). In the chemical potential corresponding to the $d,t^{3,4}\text{He}$ thermometer, a reversion of the trend is observed at 4 AMeV, analogous to the results for the lighter system [199]. Such behavior of chemical potential was also confirmed by lattice-gas calculations [203]. The estimate of the isovector chemical potential, obtained using the thermometer representing the secondary emission, still leads to approximately constant behavior above 4 AMeV. It can be concluded that the increase of the isovector chemical potential, as documented for the $d,t^{3,4}\text{He}$ thermometer, is related to de-excitation of the hot multifragmenting source and signals an increasing isospin asymmetry of the gas phase in the isospin-asymmetric liquid-gas phase transition [199].

In general, one can conclude that the trends observed in the lighter quasi-projectiles in the reactions $^{28}\text{Si} + ^{112,124}\text{Sn}$ [199, 176, 200] were confirmed in the reactions $^{40,48}\text{Ca} + ^{27}\text{Al}$ at 45 AMeV for projectile-like nuclei with mass about twice that of the former. Moreover, it has been shown that the properties of the hot systems, as reflected by the fragment observables, become still more distorted by secondary emission with increasing mass. It thus appears that thermodynamical observables, observed in multifragmentation of fully reconstructed quasi-projectiles, are consistent with the first order phase transitions. Still, the power-law behavior, considered as a signature of critical behavior and thus of second order phase transition, was observed also for one of these systems [204], and thus a question whether and under which conditions such signatures can coexist.

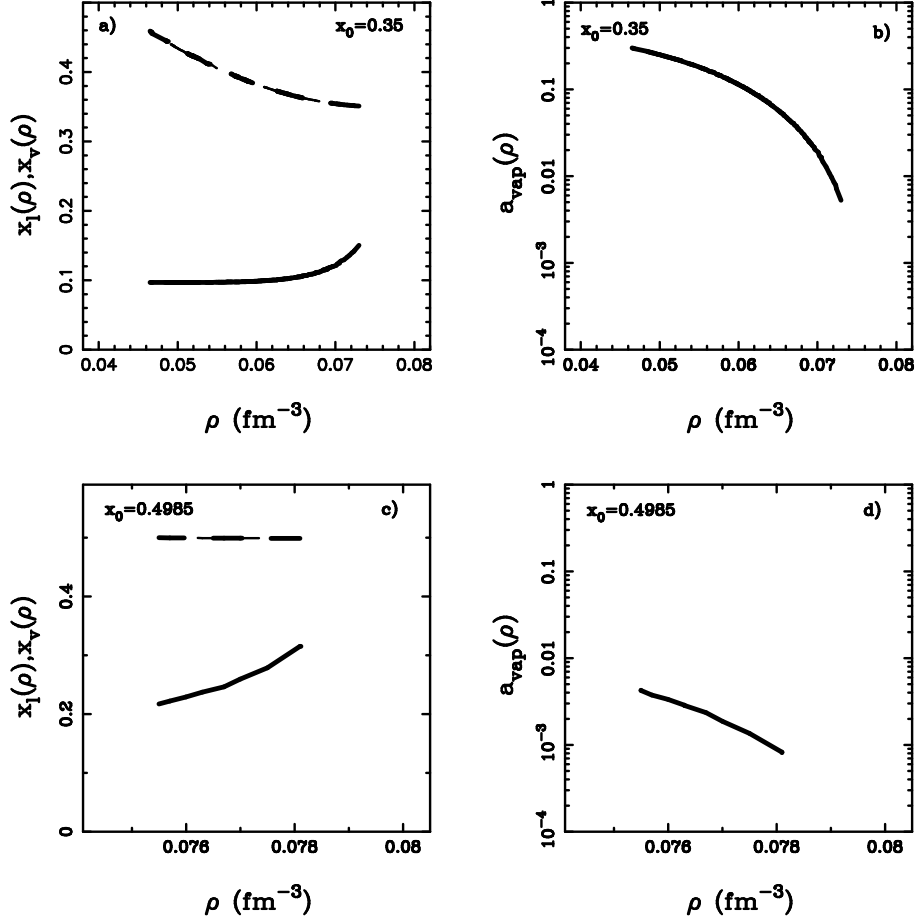


Fig. 4.7. The resulting values of a) proton concentrations x_v (solid line), x_l (dashed line) and b) vapor fraction a_{vap} for an adiabatically expanding system with $T_0 = 10$ MeV and isospin asymmetry of the system $(N - Z)/A = 0.3$. Panels c) and d) show analogous results for isospin asymmetry of the system $(N - Z)/A = 0.003$.

This question was examined in the work [205]. Thermodynamical properties of the nuclear matter at sub-saturation densities were investigated using a simple van der Waals-like equation of state with an additional term representing symmetry energy. For the isolated system an enthalpy conservation rule was introduced resulting in significant limitations for the isospin-asymmetric liquid-gas phase transition, which is a sizable effect for very isospin-asymmetric systems but becomes negligible for symmetric systems.

The resulting values of proton concentrations x_v , x_l for vapor and liquid, respectively, and mass fraction of vapor a_{vap} for an adiabatically expanding system with $T_0 = 10$ MeV are shown in Fig. 4.7, for the isospin asymmetries of the system $(N - Z)/A = 0.3$ and 0.003 , respec-

tively. It can be seen that for the asymmetric system with $(N - Z)/A = 0.3$ there occurs a well pronounced isospin asymmetric liquid-gas phase transition with a sizable part of the system being converted into very isospin asymmetric vapor while the rest of the system becomes still more and more symmetric liquid. These trends become more prominent as the density of initial meta-stable state decreases. When the system becomes more symmetric the vapor fraction drops very quickly while the vapor preserves its isospin asymmetry. Also the region of densities where isospin asymmetric liquid-gas phase transition can occur shrinks quickly. From the Fig. 4.7 one can conclude that observable isospin asymmetric liquid-gas phase transition will occur for very asymmetric systems such as these observed in the experiment [200] while for symmetric systems (and for the remnants of liquid phase in asymmetric systems) another mechanism, analogous to percolation, will play role. In order to reach spinodal region the system must pass the multifragmentation barrier and thus these systems will be unstable toward sudden decomposition into multiple fragments. Such a scenario can provide explanation for the somewhat confusing situation where signatures of both first and second order phase transitions can be extracted from observed data (even from the same set of data [200, 204]). The first-order behavior can be attributed to the distillation of isospin-asymmetric gas while the second-order signatures can be attributed to subsequent fragmentation (percolation) of the remaining symmetric liquid.

4.4 Symmetry energy

Understanding the equation of state (EoS) of asymmetric nuclear matter, i.e. nuclear matter with different neutron and proton concentrations, is of fundamental importance since it underpins our knowledge of many aspects of nuclear physics and astrophysics. The equation of state of asymmetric nuclear matter (AsyEoS) describes the relationship between energy, pressure, temperature, baryonic density and isospin asymmetry, $\delta = (\rho_n - \rho_p)/\rho$, of nuclear matter [164], where ρ_n and ρ_p are the neutron and proton densities, respectively, and $\rho = \rho_n + \rho_p$ is the total isoscalar nuclear density. The AsyEoS can be expressed as the sum of a symmetric term (i.e., independent from the isospin asymmetry) and an asymmetric term; the latter can be expressed as $E_{sym}(\rho/\rho_0)\delta^2$ [206, 207, 208, 209]; the density dependent function $E_{sym}(\rho/\rho_0)$ is termed the Symmetry Energy (SE).

One of the main goals of intermediate and relativistic energy heavy-ion collisions (HIC) is to study properties of nuclear matter, especially to determine the nuclear equation of state (EoS). HIC provide a unique possibility to compress nuclear matter to a hot and dense phase within a laboratory environment. The pressures that result from the high densities achieved during such collisions strongly influence the motion of ejected matter and are sensitive to the EoS. Within the hard work of the researchers over the three decades, the EoS of symmetric nuclear matter was studied in detail by the study of giant monopole resonances, collective flow as well as multifragmentation [165, 210, 164, 211]. The study of EoS of isospin asymmetric nuclear matter is recently underway, particularly, for the density dependence of symmetry energy. Considerable progress has been made in determining the sub- and supra-saturation density behavior of the symmetry energy [212, 213, 214, 215, 216, 217, 218, 219]. The later part is still an unanswered question in spite of recent findings in term of neutron-proton elliptic flow ratio and difference [217, 218]. However, the former one is understood to some extent [212, 213, 214, 215], although, more efforts are needed for precise measurements.

Theoretical studies of the SE have been based on different many-body theories using var-

ious two-body and three-body forces or interaction Lagrangians as well as various numerical implementations. However, because of our poor knowledge about the isospin dependence of in-medium nucleon-nucleon interaction and the difficulties in solving the nuclear many-body problem, predictions of the SE based on the three main concepts, such as the microscopic many-body approach the effective-field theory and the phenomenological approaches differ widely. The absence of strong constraints on the SE engenders major theoretical uncertainties: the above mentioned well established theoretical approaches disagree in predicting the ρ dependence of the SE among them but also within the same approach. Indeed, different parameterizations capable of describing available nucleon scattering data, lead to strong discrepancies in the ρ dependence of the SE within the same model.

Heavy-ion reactions are a unique tool for obtaining information on the SE in the laboratory, and a considerable activity is presently devoted to its low-density behavior; in contrast, very few experimental constraints exist on the SE at supra-saturation baryonic densities, $\rho > \rho_0$. In fact, recent measurements of the Giant Monopole [220] and Pygmy Dipole [221] resonances in neutron-rich nuclei, isospin diffusion [212, 214], neutron/proton emission and flow [213, 214], isospin dependence of incomplete fusion [222] and fragment isotopic ratios [223, 224] suggested a the density dependence of the SE of the form [214]

$$E_{sym}(\rho/\rho_0) = C_{s,k} \left(\frac{\rho}{\rho_0} \right)^{2/3} + C_{s,p} \left(\frac{\rho}{\rho_0} \right)^{\gamma}, \quad (4.9)$$

where the first term is related to the momentum distribution of the Fermionic gas, leading to the value of $C_{s,k} = E_F/3$, while the second term represents the potential contribution with possible exponents in the range $\gamma = 0.6 - 2$. In the near future, progresses in these kinds of measurements with both stable and radioactive isotope beams (RIB) will provide further stringent constraints at sub-saturation densities Viceversa the supra-saturation behavior, that has the largest impact on understanding certain neutron star properties [207, 208], is still subject to greatest theoretical uncertainties. The study of the SE at supra-saturation densities requires high-energy reactions capable of compressing the colliding nuclei and suitable probes sensitive to these early reaction stages. Several probes have been proposed including neutron and proton directed and elliptic flows [225, 226, 227, 228, 229], neutron/proton ratios [213, 230, 231, 232], π^+/π^- ratios and flows [233, 234, 216], K^+/K^0 [235] and Σ^-/Σ^+ [233] ratios and new experiments are expected to take place during the next few years, in Europe as well as worldwide. From the experimental point of view, three sets of existing FOPI data have been recently analyzed with the aim of providing a first study of the SE behavior at supra-saturation densities. It should be noted that none of the experiments were specifically designed and optimized to provide constraints on the SE. First of all, the double ratio $(K^+/K^0)_{Ru}/(K^+/K^0)_{Zr}$ was measured in $^{96}\text{Ru}+^{96}\text{Ru}$ and $^{96}\text{Zr}+^{96}\text{Zr}$ collisions at 1528 AMeV using the FOPI detector at GSI [236]. The results are consistent with a thermal model prediction and the assumption of a soft SE for infinite nuclear matter. More realistic transport simulations of the collisions show a similar agreement with the data but also exhibit a reduced sensitivity to the symmetry term. However, it has recently been pointed out that more experimental and theoretical work is needed to establish the effectiveness of the K^+/K^0 ratio in probing the SE [209]. Secondly, the single ratio $(\pi^+/\pi^-)_{Au}$ was measured in $^{197}\text{Au}+^{197}\text{Au}$ collisions from 400 to 1500 AMeV using the FOPI detector at GSI [237] and analyzed using the hadronic transport model IBUU04 [216]. The results suggest that the SE

is rather soft at $\rho > 2\rho_0$. Finding a SE that reaches its maximum at a density between ρ_0 and $2\rho_0$ and then starts decreasing at higher densities is not consistent with the density dependence deduced from fragmentation experiments probing nuclear matter near or below saturation [214] and with the slightly softer density dependence resulting from the analysis of the pygmy dipole resonance in heavy nuclei [221]. It is expected that pions are produced during the high-density phase of the reaction [238] but are also subject to considerable in-medium effects which have to be controlled with high precision [239, 240]. It is likely that providing definitive constraints on the SE will require consistent measurements of the several observables proposed; however, some signals appears to be controversial and strongly model dependent; to clarify this points we need a better understanding of Coulomb and surface effects, production and re-absorption of resonances, reaction dynamics, in-medium nucleon-nucleon cross section, splitting of neutron and proton effective masses in momentum dependent iso-vectorial interactions.

When considering influence of the symmetry energy on emission rates of nucleons in nucleus-nucleus collisions, one needs to understand whether and how the medium represented by the equation of state can influence relative probabilities of emission of protons and neutrons. Theoretical investigations of the density-dependence of in-medium nucleon-nucleon cross section were carried out for symmetric nuclear matter [241, 242], and significant influence of nuclear density on resulting in-medium cross sections was observed in their density, angular and energy dependencies. Using momentum-dependent interaction, ratios of in-medium to free nucleon-nucleon cross sections were evaluated via reduced nucleonic masses [243] and used for transport simulations. Still, transport simulation are mostly performed using parameterizations of the free nucleon-nucleon cross sections, eventually scaling them down empirically or using simple prescriptions for density-dependence of the scaling factor [244]. In the present work, a prescription for estimation of the density-dependence of the in-medium nucleon-nucleon cross sections corresponding to the specific form of phenomenological nuclear equation of state will be presented. Such possibility to establish a simple dependence of nucleon-nucleon cross sections on density, temperature and symmetry energy is potentially important for a wide range of problems in nuclear physics and astrophysics.

A new variant of the transport code for simulation of the nucleus-nucleus collisions was introduced in the work [245]. In variance to previous codes, used for the solution of the Boltzmann-Uehling-Uhlenbeck equation (BUU), the nucleon-nucleon cross sections, used for evaluation of the collision term, are estimated directly from the equation of state, used for evaluation of the mean-field potential. The method of estimation of the nucleon-nucleon cross sections is based on the formal transformation of the equation of state into the form of the Van der Waals equation of state and the cross sections is obtained using the proper volume, a parameter of the Van der Waals equation of state. Thus the whole calculation is based on the selected equation of state and there is no need to use free or empirically estimated in-medium cross sections. These simulations will be described using the acronym VdWBUU, while the reference simulations using the free nucleon-nucleon cross sections of Cugnon [104] will be described as fBUU.

Based on the expression for energy per particle, shown in Eq. (2.25), one can construct corresponding thermodynamical equation of the state and the resulting pressure is the weighted average between two terms, which can be expressed as [245]

$$p = \left\langle \frac{f_{5/2}(z)}{f_{3/2}(z)} \right\rangle \rho T + a\rho^2 + b\kappa\rho^{1+\kappa} + \gamma a_s \rho_0 \left(\frac{\rho}{\rho_0} \right)^{1+\gamma} \tau_z I. \quad (4.10)$$

where $\frac{f_{5/2}(z)}{f_{3/2}(z)}$ is the factor, a fraction of the Fermi integrals $f_n(z)$, assuring that Fermi statistics is taken into account. The parameters $z_n = \mu_n/T$, $z_p = \mu_p/T$ are the values of fugacity of neutrons and protons, with μ_n , μ_p being the neutron and proton chemical potential, respectively. These terms can be interpreted as the equation of state of the system of particles with the corresponding single-particle potential, given by the equation (2.25).

In order to find relation between equation of state and nucleon emission rates one can turn attention specifically to the Van der Waals equation of state. It can be written, using particle density ρ ,

$$(p + a'\rho^2)(1 - \rho b') = \left\langle \frac{f_{5/2}(z)}{f_{3/2}(z)} \right\rangle \rho T, \quad (4.11)$$

where the parameter a' is related to attractive interaction among particles and b' represents the proper volume of the constituent particles. In geometrical picture the proper volume of the particle can be directly related to its cross section for interaction with other particles. It is possible to formally transform the above equations of state for neutrons and protons (4.10) (and practically any other equation of state) into the form analogous to the Van der Waals equation. Then, by comparison, one obtains values of coefficients

$$a' = -a, \quad (4.12)$$

and

$$b' = \frac{b\kappa\rho^\kappa + \gamma a_s \left(\frac{\rho}{\rho_0}\right)^\gamma \tau_z I}{\left\langle \frac{f_{5/2}(z)}{f_{3/2}(z)} \right\rangle \rho T + b\kappa\rho^{1+\kappa} + 2\gamma\rho_0 a_s \left(\frac{\rho}{\rho_0}\right)^{1+\gamma} \tau_z I}, \quad (4.13)$$

where the latter provides a measure of the proper volume of the constituents, nucleons in this case, as a measure of deviation from the behavior of the ideal gas. The proper volume of nucleon can be used to estimate its cross section within the nucleonic medium

$$\sigma = \left(\frac{9\pi}{16}\right)^{1/3} b'^{2/3}, \quad (4.14)$$

which can be implemented into the collision term of the Boltzmann equation.

Concerning the physical meaning of this procedure, for each point in the ρ - T plane the Van der Waals equation of state is found which behaves identically to the nuclear equation of state (4.10) in the vicinity of that point. Thus the dynamics of the system can be described using the two parameters of the Van der Waals EoS, of which one provides a measure of the effective volume of the constituent at a given density and temperature. The variation of the constituent volume reflects the interplay of the long-range attractive interaction, leading to its apparent increase, with the short-range repulsive interaction, leading to its apparent decrease.

The trend of the estimated values of nucleus-nucleus cross sections, obtained using the soft parameterization of symmetry energy with $\rho^{2/3}$ -dependence is shown in the Figure 4.8 for the temperature 20 MeV. The extracted values of the cross sections are surprisingly close to the expected value of geometric cross sections. With increasing isoscalar density the values of cross

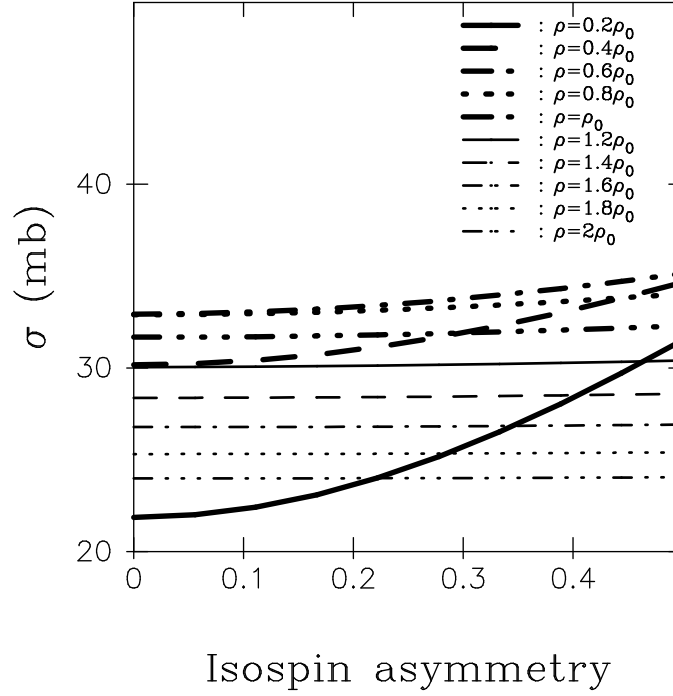


Fig. 4.8. Extracted isospin dependencies of nucleon-nucleon cross sections for temperature 20 MeV and various densities.

sections initially grow until they reach maximum values in the region around half of saturation density and then monotonously decrease. The increase at low densities possibly describes gradual deviation from the equation of state of ideal gas due to increasing attractive potential while at higher densities the decreasing trend may indeed represent the properties of short-range repulsive interaction. At high densities, with increasing isoscalar density the sensitivity to symmetry energy tends to decrease and around the density $2\rho_0$ it is practically lost, which however can be preserved using harder parameterizations of the symmetry energy. It is worth mentioning that a similar rise and fall of nucleon-nucleon cross sections was observed by the Alm, Ropke and Schmidt [242] and it was explained as a precursor effect of super-fluid phase-transition. Also in the present case this effect can be related to the phase transition in the nuclear matter, since it is caused by the same interplay of attractive and repulsive interaction which influences also the proper volume and thus extracted cross sections.

While the Boltzmann equation (2.24) is formulated in terms of density, it does not explicitly consider temperature. Therefore temperature T needs to be estimated independently. It is possible to estimate temperature using the Maxwellian momentum distribution of nucleons

$$f(\vec{p}) = \frac{1}{(2\pi mT)^{3/2}} e^{-\frac{p_x^2 + p_y^2 + p_z^2}{2mT}}, \quad (4.15)$$

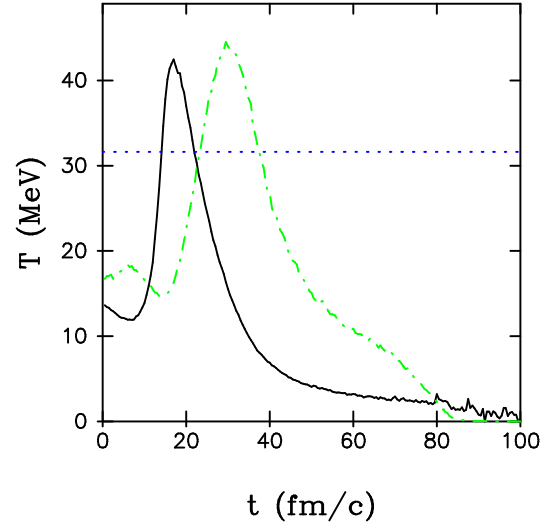


Fig. 4.9. Evolution of average temperature of the fireball (solid line) with the time. The total volume of the fireball is shown in arbitrary scale as dash-dotted line. The results were obtained using the BUU in reaction $^{48}\text{Ca}+^{48}\text{Ca}$ at 400 AMeV using the impact parameter 1 fm. Dotted straight line shows the fireball temperature estimate for a given beam energy obtained from the systematics of pre-equilibrium spectra [58].

where m is the nucleon mass. Using this formula, local temperature can be estimated from momentum distribution in the c.m. frame by evaluating the momentum variance. At early stages of collision this can be done primarily for transverse momentum since it provides a measure of mutual thermalization of particles from the projectile and target, which proceeds by distant elastic collisions generating the transverse momentum. More violent collisions would lead to emission of colliding nucleons and thus would not contribute to thermalization of the source. This temperature estimate can be done without requiring stopping and formation of the source equilibrated in all three dimensions, closer analogue would be the friction of two dilute gas clouds passing through each other.

Evolution of average temperature of the fireball with the time is shown in Fig. 4.9. The results were obtained using the Boltzmann-Uehling-Uhlenbeck equation (BUU) [101, 102] in reaction $^{48}\text{Ca}+^{48}\text{Ca}$ at 400 AMeV using the impact parameter 1 fm. Temperature was evaluated for each time step in the cubic cells with the side of 1 fm. Average temperature was determined as a mean value of temperature over all cells where number of nucleons was sufficient (corresponding to density of $\rho_0/10$) and temperature thus could be evaluated. The total volume of this fireball is shown in Fig. 4.9 in arbitrary scale as dash-dotted line. Dotted line shows the estimate of fireball temperature for a given beam energy obtained from the systematics of pre-equilibrium spectra [58]. One can see that the average temperature over the fireball at its peak value exceeds the estimate from the systematics, while the value averaged over the lifetime of the hot fireball (between 10 – 30 fm/c) appears to correspond to the value from the systematics. Thus it appears that the procedure introduced here leads to reasonable estimate of local temperature.

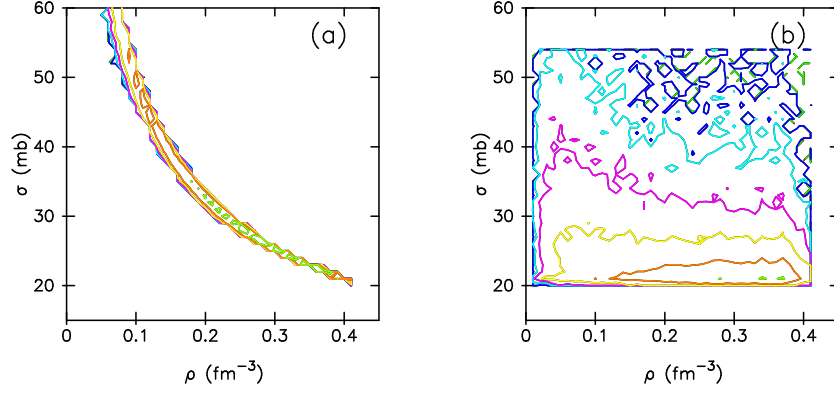


Fig. 4.10. Comparison of the nucleon-nucleon cross sections in two variants of the BUU calculations. On the left panel are the isospin-dependent nucleon-nucleon cross sections, obtained as the proper volume of the Van der Waals form of the equation of state, as a function of density, while on the right panel are shown the corresponding nucleon-nucleon cross sections, obtained using standard energy dependent parameterization, used in BUU calculation. The results were obtained using the BUU in reaction $^{48}\text{Ca}+^{48}\text{Ca}$ at 400 A MeV using the impact parameter 1 fm.

Since the temperature, determined using the assumption of Maxwellian distribution represents the classical Boltzmann statistics, it can be corrected in order to reflect the Fermi statistics, which fermions like nucleons obey. To achieve this, one needs to multiply the classical temperature T_{Boltz} , corresponding to the Boltzmann statistics, by a factor $\left\langle \frac{f_{5/2}(z)}{f_{3/2}(z)} \right\rangle^{-1}$ and thus the formula (4.13) will turn into

$$b' = \frac{b\kappa\rho^\kappa + \gamma a_s \left(\frac{\rho}{\rho_0}\right)^\gamma \tau_z I}{\rho T_{Boltz} + b\kappa\rho^{1+\kappa} + \gamma\rho_0 a_s \left(\frac{\rho}{\rho_0}\right)^{1+\gamma} \tau_z I}, \quad (4.16)$$

which corresponds to classical case of Boltzmann statistics. Thus, remarkably, this classical expression can be used also for Fermionic (or even bosonic) particles, obeying their corresponding statistics. From practical point of view, in this way the non-trivial determination of the Fermionic temperature, depending of fugacity, can be avoided.

The behavior of the in-medium nucleon-nucleon cross sections was investigated using the already mentioned reaction $^{48}\text{Ca}+^{48}\text{Ca}$ at 400 A MeV using the impact parameter 1 fm. The soft equation of state was used, leading to incompressibility coefficient $K = 200$ MeV. For the isospin asymmetric part the "asystiff" parameterization was used with two symmetry energy terms, the kinetic term with the parameters $a_{s1} = 12.5$ MeV and $\gamma_1 = 2/3$, resulting from the Pauli principle, and the potential term with the parameters $a_{s2} = 17.5$ MeV and $\gamma_2 = 2$, respectively.

Fig. 4.10 shows a comparison of the nucleon-nucleon cross sections in two variants of the Boltzmann-Uehling-Uhlenbeck simulations. On the left panel are shown, as a function of density, the isospin-dependent nucleon-nucleon cross sections, obtained using the proper volume

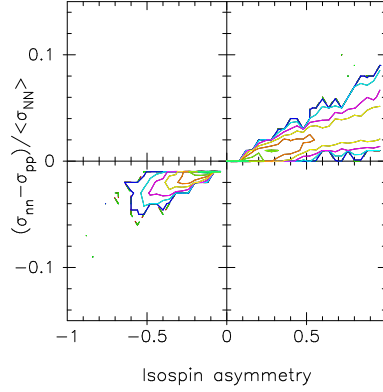


Fig. 4.11. Relative difference of the isospin-dependent neutron-neutron and proton-proton cross sections as a function of isospin asymmetry of the volume cell. The results were obtained using the BUU in reaction $^{48}\text{Ca}+^{48}\text{Ca}$ at 400 AMeV using the impact parameter 1 fm.

of the Van der Waals-like equation of state. On the right panel are shown the corresponding free nucleon-nucleon cross sections, obtained as energy dependent parameterization of measured nucleon-nucleon cross sections [104]. It is apparent that while the isospin-dependent nucleon-nucleon cross sections essentially follow the $1/\rho^{2/3}$ -dependence, the nucleon-nucleon cross section parameterization of Cugnon et al. leads to much larger spread, mostly due to its explicit energy dependence. Nevertheless, one observes that both parameterization cover essentially the same range of values of the nucleon-nucleon cross sections. Furthermore, from the comparison [246] of the parameterization of Cugnon et al. to in-medium cross sections at saturation density, calculated using the G-matrix theory by Cassing et al. [247], it can be judged that the in-medium cross sections, obtained using the proper volume of the Van der Waals-like equation of state, are in better agreement with somewhat higher values of G-matrix in-medium cross sections of Cassing et al., which reflect properly the Fermionic nature of nucleons.

In general, it is remarkable, that the in-medium nucleon-nucleon cross sections can be possibly directly related to the equation of state of the isospin asymmetric nuclear matter. This offers a more consistent description of the nuclear reactions and various astrophysical objects and processes in term of properties of nucleonic matter, expressed using the corresponding equation of state. However, one has to take into account that the equation of state of the isospin asymmetric nuclear matter describes isotropic medium and thus the extracted in-medium cross sections represent angle-averaged values. These values are used in this work, and compared to the results obtained with angle-averaged free cross sections of Cugnon et al. [104], and thus the effect of the equation of state of the isospin asymmetric nuclear matter on in-medium cross sections is demonstrated. However, one can consider possibility to implement angular dependence, either using the compatible microscopic calculations or from the observed experimental free nucleus-nucleus cross sections. This possibility is beyond the scope of the present work and will be investigated in our future work.

The magnitude of the effect of isospin asymmetry on the nucleon-nucleon cross sections can be judged from Fig. 4.11, which shows the relative difference of the isospin-dependent neutron-

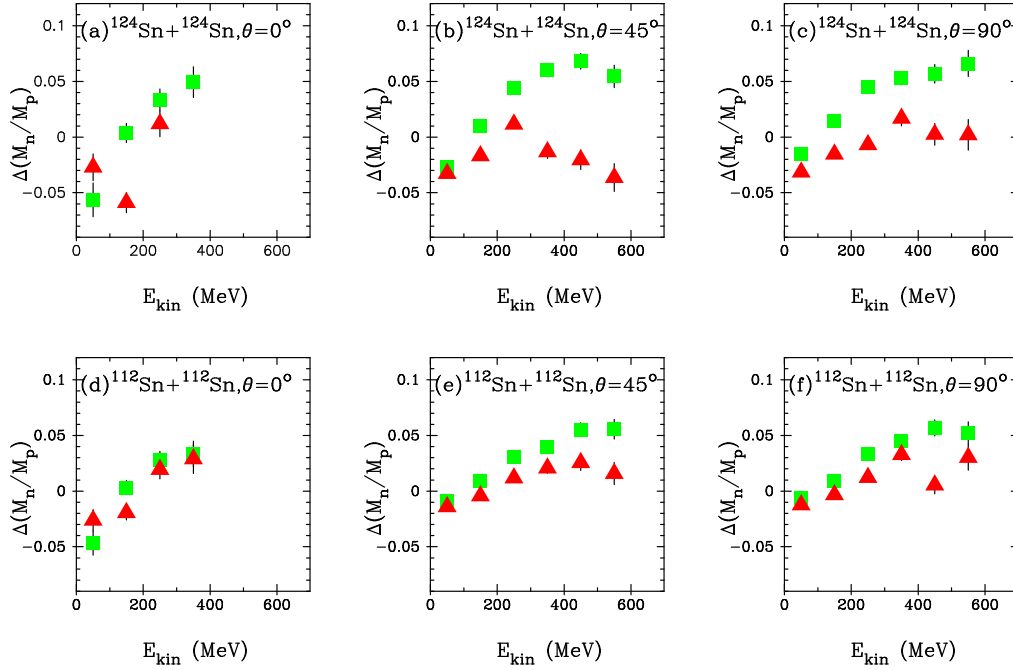


Fig. 4.12. Evolution of the difference of n/p multiplicity ratio between VdWBUU and fBUU calculations for three angular ranges. The results were obtained in reactions $^{124}\text{Sn}+^{124}\text{Sn}$ and $^{112}\text{Sn}+^{112}\text{Sn}$ at 400 AMeV using the impact parameter 1 fm at the time 200 fm/c. Squares show the result with stiff symmetry energy while triangles show results for soft symmetry energy. Soft nuclear equation of state is used.

neutron and proton-proton cross sections as a function of isospin asymmetry of the volume cell. The results were again obtained using the BUU in reaction $^{48}\text{Ca}+^{48}\text{Ca}$ at 400 AMeV using the impact parameter 1 fm. One can see that the relative magnitude does not reach very high values even for most isospin-asymmetric cells, and the sensitivity of the Boltzmann-Uehling-Uhlenbeck simulation to the isospin-dependent nucleon-nucleon cross sections will result from the cumulative effect of large amount of nucleus-nucleus collisions.

Figure 4.12 shows evolution of the difference of n/p multiplicity ratios between Boltzmann-Uehling-Uhlenbeck simulation with both the isospin-dependent mean-field and the nucleon-nucleon cross sections which are correlated to each other by the Eq. 4.14 (based on the analogy with the van der Waals equation of state, thereafter we call this simulation as VdWBUU) and Boltzmann-Uehling-Uhlenbeck simulation with isospin-dependent mean-field and free nucleon-nucleon cross sections (thereafter we call it fBUU), for three angular ranges as a function of the kinetic energy in the center-of-mass system. The results were obtained using the BUU simulation in reactions $^{124}\text{Sn}+^{124}\text{Sn}$ and $^{112}\text{Sn}+^{112}\text{Sn}$ at 400 AMeV using the impact parameter 1 fm at the stopping time 200 fm/c. Squares show the result with stiff symmetry energy parameterization ($a_{s1} = 12.5$ MeV, $\gamma_1 = 2/3$, $a_{s2} = 17.5$ MeV and $\gamma_2 = 2$) while triangles show results for with soft symmetry energy parameterization ($a_{s1} = 12.5$ MeV, $\gamma_1 = 2/3$, $a_{s2} = 17.5$ MeV and $\gamma_2 = 1/2$).

Soft nuclear equation of state ($K = 200$ MeV) is used in this case. Particles are considered as emitted when they are separated in the phase-space from any other particle and separation is large enough to assure that two particles are not part of a cluster (a condition $\Delta\vec{p}\Delta\vec{r} > 2h$ is implemented). One can see that implementation of isospin-dependent nucleon-nucleon cross sections leads to significant variation of n/p multiplicity ratio and this effect appears to evolve with both kinetic energy and polar angle. Variation of n/p multiplicity ratio is more significant for the more neutron-rich system, which offers a strong argument for the use of neutron-rich exotic beams for studies of density dependence of the symmetry energy in the future.

Picture remains analogous also in the case of stiff nuclear equation of state ($K = 380$ MeV), one can see that implementation of isospin-dependent nucleon-nucleon cross sections leads to considerable variation of n/p multiplicity ratio, which again evolves with both kinetic energy and polar angle. Also here the variation of n/p multiplicity ratio is more significant for the more neutron-rich system. It thus appears that variation of n/p multiplicity ratio between VdWBUU calculation and fBUU calculation provides a robust signal of the density dependence of nuclear symmetry energy. Furthermore, the effect of isospin-dependent nucleon-nucleon cross sections persists, with comparable magnitude, even in peripheral collisions. This offers possibility to study such signal of the density-dependence of the symmetry energy in a wide range of centralities and thus eventually to provide a strong signal of the density-dependence of the symmetry energy in a wider range of nuclear density.

The fact, that the isospin-dependent nucleon-nucleon cross sections, obtained using the proper volume of the Van der Waals-like equation of state, need to be introduced in order to fully explore the isospin dependence in the Boltzmann-Uehling-Uhlenbeck simulations, directly affects the applicability of the symmetry energy parameterizations to the study of astrophysical objects such as neutron stars or supernovae. Due to increased sensitivity to isospin due to isospin-dependent nucleon-nucleon cross sections, the symmetry energy parameterizations may change significantly and that will affect the extrapolations toward the nuclear densities, typical for neutron stars and similar objects. On the other hand, increased sensitivity may offer more possibilities for the simulations of reactions of exotic nuclear beams, with the possible observation of stronger isospin-dependent signals.

It is of interest to estimate what effect will the introduction the isospin-dependent nucleon-nucleon cross sections, obtained as the proper volume of the Van der Waals-like equation of state, have on the resulting elliptic flow of neutrons and protons. Figure 4.13 shows calculated values of the elliptic flow of neutrons and protons (determined conventionally as second Fourier coefficient of the invariant triple differential distribution v_2 relative to reaction plane) in reactions $^{124}\text{Sn}+^{124}\text{Sn}$ and $^{112}\text{Sn}+^{112}\text{Sn}$ at 400 AMeV at the impact parameter 6 fm. Solid and open squares show results of VdWBUU calculation and fBUU calculation, respectively, with soft symmetry energy parameterization. Solid and open asterisks show analogous results with stiff symmetry energy parameterization. One can see that introduction of isospin-dependent nucleon-nucleon cross sections, varying the ratio of neutron-neutron and proton-proton collision rates and thus modifying the in-plane/out-of-plane emission ratios, influences the resulting values of the elliptic flow, and since the effect appears to vary between neutrons and protons, it will strongly influence the differential elliptic flow, thus making it a strong signature of the nuclear equation of state, as suggested in the work [217]. However, since the effect of symmetry energy on such differential elliptic flow tends to vary also with isoscalar part of the nuclear equation of state, it appears necessary to study differential elliptic flow in combination with other observables, such

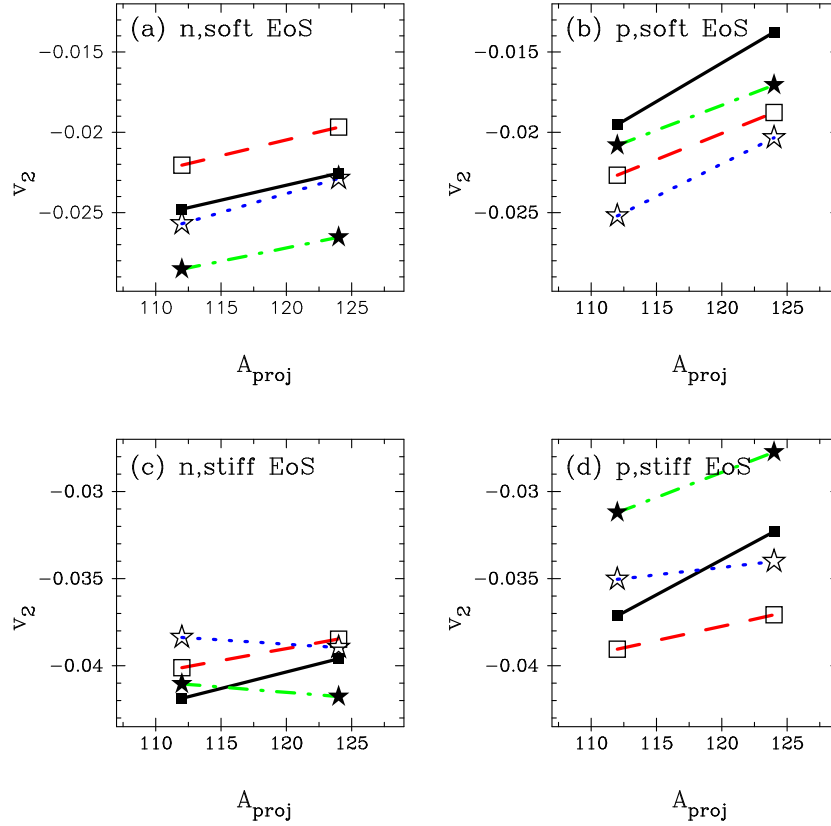


Fig. 4.13. Elliptic flow of neutrons and protons in reactions $^{124}\text{Sn}+^{124}\text{Sn}$ and $^{112}\text{Sn}+^{112}\text{Sn}$ at 400 AMeV at the impact parameter 6 fm. Solid and open squares show results of VdWBUU calculation and fBUU calculation, respectively, with soft symmetry energy. Solid and open asterisks show analogous results with stiff symmetry energy.

as the evolution of n/p multiplicity ratio at different polar angles and kinetic energies. Such a study, carried out on sufficiently neutron-rich system, can provide a good sensitivity to both isoscalar and isovector part of the nuclear equation of state.

As already mentioned, the flow observables were introduced primarily as observables directly related to the equation of the state of nuclear matter. The specific flow observables can be identified with the coefficients of the Fourier expansion of the azimuthal angular distribution relative to the reaction plane. Flow observable, related to the first Fourier coefficient v_1 is usually called as directed transverse flow. It can be alternatively expressed in terms of a slope of the momentum p_x (in the reaction plane) at zero rapidity. The systematics of this observable for protons observed in the collisions of Au+Au at various beam energies was published in [248]. The elliptic flow is characterized by the value of the second Fourier coefficient v_2 and its systematics for the protons observed in the collisions of Au+Au at mid-rapidity was published in the

work [249]. When combined, these two systematics provide a good set of experimental data for testing of the transport codes and for determination of the parameters of the equation of the state of nuclear matter.

In order to evaluate flow observables in the BUU simulations, it is necessary to implement a method for selection of the free nucleons. Like in the work [245], in a standard variant, particles are considered as emitted when they are separated in the phase-space from any other particle and separation is large enough to assure that two particles are not part of a cluster (a condition $\Delta\vec{p}\Delta\vec{r} > 2h$ is implemented). Since the work [101], the equations of state used in simulations usually represent two extremes of the mean field, the soft EoS with the compressibility K_0 of 200 MeV ($\kappa = 7/6$), and the hard EoS with K_0 of 380 MeV ($\kappa = 2$). The symmetry energy is usually parameterized in two ways, either as a stiff symmetry energy parameterization ($a_{s1} = 12.5$ MeV, $\gamma_1 = 2/3$, $a_{s2} = 17.5$ MeV and $\gamma_2 = 2$) or soft symmetry energy parameterization ($a_{s1} = 12.5$ MeV, $\gamma_1 = 2/3$, $a_{s2} = 17.5$ MeV and $\gamma_2 = 1/2$). However, in order to perform a detailed analysis, also testing of intermediate equations of state and density dependences of symmetry energy is desirable, and such equations of state, fulfilling the usual saturation conditions, were introduced.

As a best variant of the calculations appears to be the VdWBUU simulation (with in-medium nucleon-nucleon cross sections) using the EoS with compressibility K_0 of 272 MeV ($\kappa = 1.5$) and the symmetry energy parameterization ($a_{s1} = 12.5$ MeV, $\gamma_1 = 2/3$, $a_{s2} = 17.5$ MeV and $\gamma_2 = 1.5$). Besides the selection criterion mentioned above, the low energy cutoff was implemented at transverse momentum 0.4 GeV/c, since such low-energy particles carry essentially their initial randomly generated transverse momenta, and also the effect of Coulomb interaction, which would affect primarily these particles, is not taken into account in the BUU. The results are shown in the Figure 4.14. From the other simulations, the one with the same EoS and the soft symmetry energy parameterization fails most dramatically in particular case of the elliptic flow at the lowest beam energy 400 AMeV, which can be a sign of the sensitivity of the elliptic flow at this energy toward density dependence of the symmetry energy. The simulations with the soft EoS fail to reproduce both the directed transverse flow and elliptic flow and thus the soft EoS appears to be excluded by the experimental directed transverse flow and elliptic flow systematics in the Au+Au collisions at the impact parameters $b = 5.5\text{--}7.5$ fm.

From the fBUU simulations using the free nucleon-nucleon cross sections, none can reproduce all the experimental observables. The better results were obtained using the using the stiff EoS, where stiff symmetry energy parameterization appears to give slightly better results for elliptic flow than the soft symmetry energy parameterization, especially at the lowest beam energy 400 AMeV. The results for the stiff EoS and the stiff symmetry energy parameterization, using again the selection criterion mentioned above and the low energy cutoff at transverse momentum 0.4 GeV/c fail to describe the elliptic flow, and, moreover, especially interesting appears the failure to describe the directed flow at 10 AGeV. In comparison with the conclusions of the work [245], it appears that the implementation of the EoS-dependent in-medium nucleon-nucleon cross sections results in more realistic dependence of the results of simulations on the parameterization of the density-dependence of symmetry energy. The simulation with the free nucleon-nucleon cross sections (fBUU) appears to hint at the correct trend of the density dependence of the symmetry energy, it however appears to be inconclusive in this respect. Similarly to VdWBUU simulations, the fBUU simulations with the soft EoS again fail to reproduce both the directed side flow and elliptic flow and thus the soft EoS appears to be excluded.

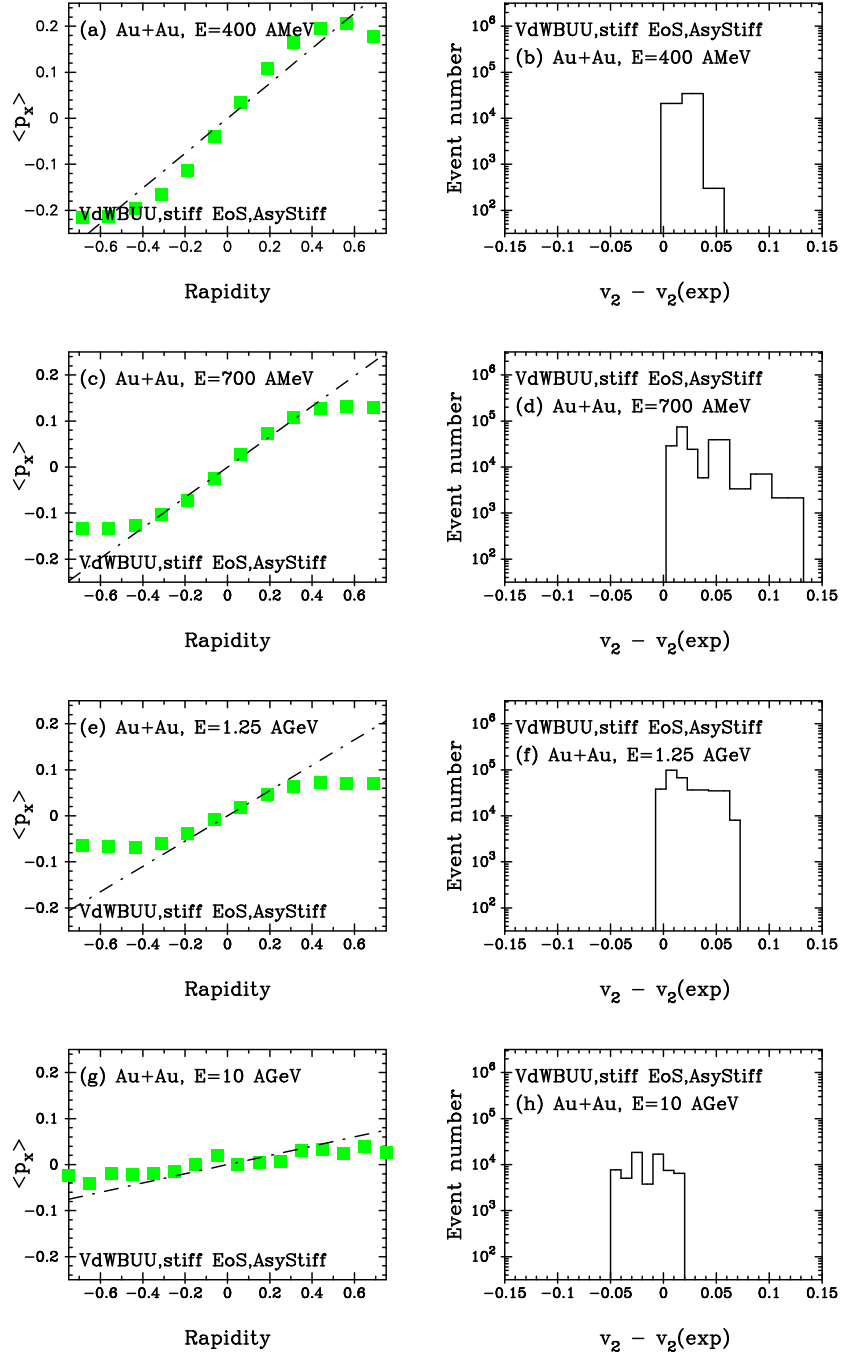


Fig. 4.14. Systematics of the proton directed transverse flow (right panels, lines show experimentally observed slopes) and the difference of calculated and experimental proton elliptic flow at mid-rapidity (left panels) in the collisions of Au+Au at various beam energies. Results were obtained using the VdWBUU simulation using the EoS with compressibility K_0 of 272 MeV and the symmetry energy parameterization with $\gamma_2 = 1.5$.

The new implementation of the BUU, the VdWBUU simulation (with in-medium nucleon-nucleon cross sections) thus appears to reproduce the flow observables in the Au+Au collisions in the energy range from 400 AMeV to 10 AGeV using the stiff EoS and the stiff symmetry energy parameterization. The implementation of the BUU, using the free nucleon-nucleon cross sections, can not describe correctly the global trends of flow observables. The model thus provides an environment for testing of equations of state, used for various applications in nuclear physics and astrophysics. The possible implications for nuclear astrophysics will be discussed later.

4.5 Quark deconfinement phase transition

As shown earlier, nucleus-nucleus collisions at ultra-relativistic energies lead to conditions suitable for the release of quarks and gluons from the confinement in hadrons. Quantum Chromodynamics (QCD), the theory of strong interactions (see [250] for a recent review), predicts a phase transition from a state of hadronic constituents to a plasma of deconfined quarks and gluons, as the energy density exceeds a critical value. The opposite phase transition, from quarks and gluons to hadronic matter, took place about 10^{-5} s after the Big Bang, which is supposed to be at the origin of our Universe. The ultrarelativistic nucleus-nucleus collisions [251] offer the conditions for study of the properties of strongly interacting matter at high energy density, in particular its phase diagram and the properties of quark-gluon plasma (QGP) [252].

Already in 1951 Pomeranchuk [253] conjectured that a finite hadron size implies a critical density, n_c , above which nuclear matter cannot be in a hadronic state. In 1965, Hagedorn [254] inferred that an exponentially growing mass spectrum of hadronic states (observed up to masses of about 1.5 GeV) implies a critical temperature T_c of the order of 200 MeV ($\approx 2 \cdot 10^{12}$ K). However, the elementary building blocks of QCD, the quarks and gluons (carrying an extra quantum number called "color") have not been directly observed in experiments, although indications of their existence have been clearly identified in deep-inelastic collisions and jet production. A fundamental property of QCD, the asymptotic freedom, first introduced by Gross, Wilczek, and Politzer in 1973 [255], implies that the attractive force (coupling) between quarks increases as a function of their separation. Moreover, the confinement of quarks (and gluons) inside hadrons is another fundamental feature of QCD, although not fully understood yet. The term quark-gluon plasma was first introduced by Shuryak [256].

When the quarks are released from hadrons, two not necessarily related phase transitions can occur. Besides asymptotic freedom, release of quarks also means restoration of chiral symmetry, with the consequence that free quarks lose almost all of their constituent mass inside hadrons and preserve only much smaller current mass. An important (and not yet answered) question is whether the critical temperatures for deconfinement T_c and for chiral symmetry restoration (T_χ) coincide, for which there is no known circumstance which would require that.

It is normally supposed, that the critical point of the phase transition will be located at high values of baryonic chemical potential (at the end of the solid line in Figure 4.15) and thus may not be crossed at heavy-ion colliders such as RHIC and LHC (such crossover phase transition is illustrated by dashed line in Figure 4.15), however recent theoretical results [257] suggest that, at some values of the pion mass (which is a measure of the spontaneous breaking of chiral symmetry), there might appear additional critical point at low values of baryonic chemical potential. Thus possibly an another open question might arise from these recent results.

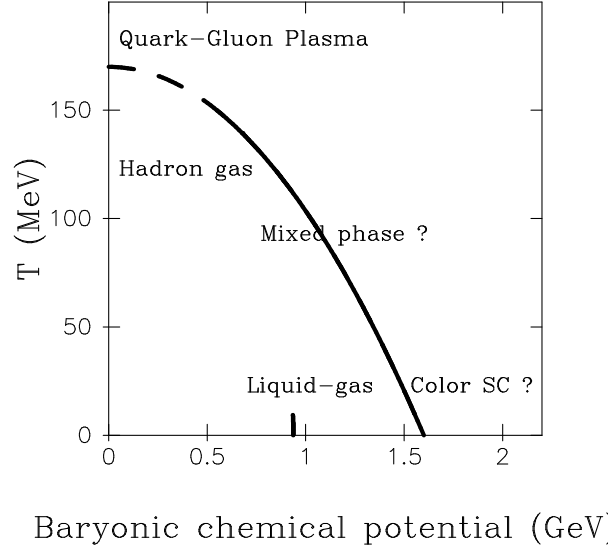


Fig. 4.15. Schematic phase diagram of the quark deconfinement phase transition.

The phase diagram at high values of baryonic chemical potential may exhibit some other exotic forms of nuclear matter, such as quarkyonic matter [258], where quarks are confined but chirally symmetric, or color superconductor [259] (Color SC in Figure 4.15). However, the part of the phase diagram around the expected first-order phase transition (solid line in Figure 4.15) with the possible mixed phase will be possible to investigate at the presently constructed facilities such as FAIR in Darmstadt, Germany, NICA at Dubna, Russia, or at IMP in Lanzhou, China.

The transition to free quarks and gluons is accompanied by the sudden increase of the energy density as a function of temperature. For the 2-flavor case, the transition corresponds to a critical temperature $T_c \simeq 170$ MeV with critical energy density $\varepsilon_c \simeq 0.7$ GeV, while for the 3-flavor case T_c is smaller by about 20 MeV.

Thermodynamical description of quark-gluon plasma starts from grand partition functions for fermions (particles and anti-particles) and bosons

$$(T \ln Z)_f = \frac{g_f V}{12} \left(\frac{7\pi^2}{30} T^4 + \mu^2 T^2 + \frac{1}{2\pi^2} \mu^4 \right), \quad (T \ln Z)_b = \frac{g_b V \pi^2}{90} T^4, \quad (4.17)$$

where g_f and g_b are the respective degeneracies (degrees of freedom). The average energy, particle number and entropy densities and the pressure then become

$$\varepsilon = \frac{T}{V} \frac{\partial(T \ln Z)}{\partial T} + \mu n, \quad n = \frac{1}{V} \frac{\partial(T \ln Z)}{\partial \mu}, \quad P = \frac{\partial(T \ln Z)}{\partial V}, \quad s = \frac{1}{V} \frac{\partial(T \ln Z)}{\partial T}. \quad (4.18)$$

Using the thermodynamic relation: $\varepsilon = -P + Ts + \mu n$ one can establish the equation of state (EoS) of an ideal gas: $P = \varepsilon/3$. Assuming that the hadronic world is composed of pions, $g_h = 3$. For three colors and two spin values, for quarks and gluons one has $g_q = 12N_f$ and

$g_g = 16$, respectively. N_f is the number of flavors (the lighter quarks u , d and s are the only ones relevant). Consequently, at vanishing the chemical potential, the energy densities for the hadronic stage and for a gas of free quarks and gluons are, respectively:

$$\varepsilon_h/T^4 = \frac{\pi^2}{10}, \quad \varepsilon_{qg}/T^4 = (32 + 21N_f)\frac{\pi^2}{60}. \quad (4.19)$$

For $N_f = 3$, $\varepsilon_{qg}/T^4 = 15.6$, denoted as the Stefan-Boltzmann limit, ε_{SB} . It is interesting to note that the calculated values are well below the values for non-interacting gases, indicating that the QGP is far from an ideal gas at temperatures as high as several times T_c .

A simple way to incorporate the two basic properties of QCD, asymptotic freedom and confinement, is achieved in the so-called (MIT) bag model [260]. It prohibits quarks and gluons from existing outside the bag (which can be any finite volume) by adding a shift from the physical vacuum into the QCD vacuum by an extra term in the partition function of the plasma phase: $(T \ln Z)_{vac} = -BV$, where B is the bag constant. It is easy to show that the EoS in this case becomes: $P = (\varepsilon - 4B)/3$. The phase transition trajectory in the $T - \mu$ plane can be constructed by applying the Gibbs criteria for the phase transition:

$$P_h = P_{qg}, \quad \mu_h = \mu_{qg} (= 3\mu_q), \quad T_h = T_{qg} = T_c. \quad (4.20)$$

which leads to the quadratic dependence analogous to the one shown in Fig. 4.15.

Clearly, given the short timescales of a nucleus-nucleus collision and the small volume involved (typical lattice QCD calculations are performed for the bulk properties) the reconstruction of the various stages of the collision is a difficult task. It is consequently of great importance to find experimental observables which carry information (preferentially) from one particular stage, in particular about the QGP phase. Specific probes of QGP have been proposed [110, 261] and are currently being studied experimentally: i) direct photons [262]; ii) low-mass dileptons [263]; iii) strangeness [264]; iv) charmonium suppression [252]; v) jet-quenching [265]; vi) fluctuations [266, 267].

Of these probes, as the most direct, model independent and most conclusive concerning the existence of strongly interacting deconfined medium such as quark-gluon plasma appears jet-quenching (jet medium modification). Hadronic jets are signatures of scattered high energy partons (quarks and gluons), which due to confinement potential produce a number of correlated hadrons. Such jets are usually produced in pairs. In the quark-gluon plasma, the quarks may lose part of their energy and the jet may be strongly modified or disappear at all. The nuclear modification factor R_{AA} is obtained from comparison of yields of inclusive charged hadrons in the nucleus-nucleus collision to the same quantity in proton-proton collisions, with appropriate normalization factor. First evidence of parton energy loss has been observed at the Relativistic Heavy Ion Collider (RHIC) from the suppression of high- p_t particles studying the nuclear modification factor R_{AA} [268] and the suppression of back-to-back correlations [269]. At RHIC, the observed magnitude of the medium modification was sufficient to counterbalance the R_{AA} enhancement due to multiple scattering (the so-called Cronin effect), while in ultra-relativistic heavy-ion collisions at center-of-mass energy of 2.76 TeV at the Large Hadron Collider (LHC), the direct observation of jet quenching [270] already leads to the values of R_{AA} down to 0.2. Also, the preliminary results from LHC indicate expected hierarchy among light and heavy quarks.

Thus it appears that the evidence of the existence of the new state of matter with deconfined quarks and gluons is provided. Based on the data on elliptic flow, this matter was reported [271]

to exhibit properties of the ideal liquid with minimum shear viscosity (close to the theoretical low limit $\eta/s = 1/4\pi$), as it is indicated by comparison to hydrodynamical simulations. The hydrodynamical simulations (for an overview see e.g. [272]) apply ideal fluid dynamics to generate the resulting flow observables, starting from some initial condition, representing the time and temperature at which the system reached thermal equilibrium. Matter which can be characterized as a "perfect liquid" will necessarily differ from weakly coupled quark-gluon plasma (non-interacting ideal quark and gluon gas) since it still appears to exhibit strong interaction and thus it is usually named as strongly coupled quark-gluon plasma (sQGP). However, an alternative explanation, using the two component model, combining the hard (perturbative QCD) and soft (projectile dissociation according to parton distribution function) processes, appears feasible [273]. Thus the essence of the observed matter might be a topic of further discussion.

The initial conditions, mentioned above, are usually estimated using the properties of the hadronic final, as shown earlier. In order to describe such initial condition, several models were developed. One of them is the so-called Color Glass Condensate [274]. According to Einstein's theory of relativity, a high-energy nucleus appears length contracted, or compressed, along its direction of motion. As a result, the gluons inside the nucleus appear to a stationary observer as a "gluonic wall" traveling near the speed of light. At very high energies, the density of the gluons in this wall is seen to increase greatly, and the shadowing and saturation effects may arise, in principle analogous to saturation in nuclear matter. Unlike the quark-gluon plasma produced in the collision of such walls, the color-glass condensate describes the walls themselves, and is an intrinsic property of the particles that can only be observed under high-energy conditions such as those at RHIC and at the LHC. However, the minijet model [275], based on perturbative QCD, appears also to be able to describe experimental initial conditions [273]. Further work will be needed to decide which description is more appropriate.

The observation of jet medium modification open possibility to study mechanism of energy loss in the strongly interacting deconfined medium. The perturbative QCD considers mechanism of energy loss due to gluonic radiation. However, also the energy loss due to scattering can not be excluded. In order to study the properties of the quark-gluon plasma in non-perturbative QCD approach, the gauge gravity duality (conformal field theory in the anti-de Sitter space, AdS/CFT) was introduced from the string theory. This theory is capable to describe qualitatively various aspects of nucleus-nucleus collisions, such as thermodynamics and hydrodynamical description, including e.g. the low limit of shear viscosity (for overview we refer to [276]), and offers also possibility to study mechanism of energy loss. In any case, the availability of theory, capable to describe the parton energy loss, is crucial for understanding the physics of strongly interacting deconfined matter.

As shown above, the study of ultrarelativistic nucleus-nucleus collisions appears to be a very lively and quickly evolving field (much richer than it was possible to show in this article) and further investigations, which are underway both at the LHC and in theory will be needed to construct a consistent global picture and thus achieve a major progress in the study of strongly interacting matter.

4.6 Implications for nuclear astrophysics

Study of the equation of state in nucleus-nucleus collisions can in principle provide information, necessary to describe properties of stellar objects like supernovae and neutron stars and astro-

physical properties such as nucleosynthesis. A review of possible nuclear and particle physics that can be studied with neutron stars can be found e.g. in [161]. Already in 1934 the idea was expressed by Baade and Zwicky that some supernovae are driven by the energy released in collapse of the core of a massive star into a dense compact stellar object [160]. These objects are named neutron stars. Neutron stars are observed as pulsars, rapidly rotating neutron stars emitting radio waves from their magnetic poles. If the star's magnetic axis is not aligned with the rotation axis these emissions are observed as pulse trains. These cosmic lighthouses were first observed by Bell and Hewish in 1967 [277]. Since that time neutron stars/pulsars have been the subject of intensive studies as they serve as a laboratory for study of matter under extreme conditions. Neutron stars appear to have average densities of the order of nuclear matter $\approx 10^{14}$ g/cm³ [160] and magnetic field strengths of between 10^8 and 10^{13} G [278]. Thus neutron stars, besides being suitable systems for investigating theories of gravity and of the interstellar medium, are unique laboratories for studying matter at high densities. In neutron stars, matter ranges from nuclei embedded in a sea of electrons at low densities in the outer crust, to increasingly neutron-rich structures in the inner crust, to the extremely neutron-rich uniform matter in the outer core, and possibly exotic states of matter at high densities in the inner core [279, 280]. The theoretical understanding of nuclear matter and atomic nuclei over such a range of densities and isospin asymmetry is one of the current frontiers in nuclear science. The equation of state (EoS) of dense matter is also a key ingredient in modeling neutron star and black hole formation and, in particular, the gravitational wave signal from mergers of binary neutron stars [281, 282, 283] and neutron star-black hole mergers [284] is sensitive to it.

In order to describe structure of a neutron star, general theory of relativity needs to be applied. The resulting Tolman-Oppenheimer-Volkov (TOV) equation is used to calculate the mass-radius relationship of a neutron star. In natural units the TOV equation is [160]

$$P'(r) = \frac{dP}{dr} = -\frac{\mathcal{G} [\epsilon(r) + P(r)] [M(r) + 4\pi r^3 P(r)]}{r [1 - 2\mathcal{G}M(r)]} \quad (4.21)$$

with

$$M'(r) = \frac{dM(r)}{dr} = 4\pi\epsilon(r)r^2, \quad (4.22)$$

and where

- \mathcal{G} is the gravitational constant,
- $M(r)$ is the enclosed mass of the star,
- $\epsilon(r)$ is the energy density, and
- $P(r)$ is the internal pressure of the star.

Implicit assumption, not fully corresponding to real neutron star but simplifying calculations, is that a neutron star is a static, spherical symmetric relativistic fluid in hydrostatic equilibrium and no rotational effects on the star's interior and metric are considered. Since (4.21) and (4.22) are two coupled differential equations they have to be solved numerically. In order to solve the equations the appropriate equation of the state needs to be chosen, the central density ρ_c needs to be set and the edge of the star is defined by a chosen pressure P_R (in general chosen corresponding

to the density of iron or some other heavy metal.), at which point the value of r is defined to be the radius, R , of the star and mass enclosed by R , $M(R)$, the mass of the star. By solving for a range of ρ_c , using the same equation of state, a series of solutions of the TOV equation are produced. For the canonical neutron star, R is of the order of 10 km and M is about $1.5 M_\odot$ [160].

Neutron stars are thus of particular interest as the object allowing to constrain the nuclear equation of state. Specifically, several aspects of neutron star physics and supernovae collapse rely on the density dependence of the symmetry energy. Among them can be mentioned the nature of various phases coexisting within a neutron star [285], the feasibility of direct URCA cooling processes [286], proto-neutron star cooling rates [208, 287], the composition [285] and the thickness of its inner crust, the frequencies of its crustal vibrations and neutron stars radii [208]. These properties are currently being investigated with ground-based and satellite observatories.

Alternatively to nucleus-nucleus collisions, the density dependence of the symmetry energy in nuclear astrophysics is parameterized using only the linear and quadratic terms in the vicinity of saturation density

$$E_{sym}(\rho) = E_{sym}(\rho_0) + \frac{L}{3} \left(\frac{\rho - \rho_0}{\rho_0} \right) + \frac{K_{sym}}{18} \left(\frac{\rho - \rho_0}{\rho_0} \right)^2 \quad (4.23)$$

where L and K_{sym} are the slope

$$L \equiv 3 \left[\rho_0 \frac{d}{d\rho} \left(\frac{E_{sym}(\rho)}{\rho} \right) \right]_{\rho=\rho_0} \quad (4.24)$$

and curvature parameters

$$K_{sym} \equiv 9 \left[\rho_0^2 \frac{d^2}{d\rho^2} \left(\frac{E_{sym}(\rho)}{\rho} \right) \right]_{\rho=\rho_0} \quad (4.25)$$

and use of such parameterization allowed to establish e.g. linear correlation of the neutron skin thickness of nucleus ^{208}Pb to the slope parameter L [288], which demonstrates a close relation of the properties of finite nuclei to properties of stellar objects. Unfortunately, for now the skin thickness of ^{208}Pb is not known with precision allowing to constrain the parameter L . The results of the PREX experiment were reported recently [289, 290], indicating larger than expected value of the skin thickness, however the experimental uncertainties are still too large to make definite conclusions.

The recent work [291] reports a representative study of constraints on EoS, resulting mainly from the least model dependent property of neutron star which is its maximum mass. Using the above TOV equation and a particular equation of state, it is possible to obtain the mass vs radius correlation, which allows to determine the maximum mass of the neutron star, limits for its radius and for its central density. The family of equations of state was restricted by the representative set of results from nuclear physics, including nucleus-nucleus collisions. As the maximum mass of the neutron star a recently value of $M = 1.97 M_\odot$ [292] is used. The value of the symmetry energy at saturation density was constrained to $E_{sym}(\rho_0) = 30\text{--}33.5$ MeV and the slope parameter was constrained less strictly to a range of values $L = 32\text{--}57$ MeV. This range of values allows the wide range of compressibilities of which the values $K = 210\text{--}260$ MeV were considered, and the restrictions on radii of neutron stars are obtained and compared to available

data, which however is not sufficiently precise at present. The stiffer the equation of state is, the larger the allowed maximum mass of neutron star becomes, while the central density drops and radius of the neutron star increases. For instance, the observation of the heavy neutron star with mass $M = 1.97M_{\odot}$, appears to exclude very high central densities, necessary for the existence of matter with deconfined quarks in the star interior. This restriction may become even tighter in the case that the reported observation of the neutron star with mass $M = 2.4M_{\odot}$ [293] will be confirmed.

In this context it is interesting to consider to what extent is the possible combination of the EoS with $K_0 = 272$ MeV and symmetry energy with $\gamma = 1.5$ in equation (4.9), obtained from flow systematics, compatible with results obtained for neutron stars. The parameterization of symmetry energy, used in [291], differs from eq. (4.9), however, it suggests that EoS is consistent with relatively stiff symmetry energy with $\gamma_2 = 1.5$. The constrained values of $E_{sym}(\rho_0)$ and L depend only weakly on compressibility of EoS and thus even stiffer equations of state appear feasible, even if restrictions due to causality must be considered. Also, the recent re-analysis of the determination of the neutron star radii appears to lead to larger radii with lower limit around 14 km [294] and thus to stiffer equation of the state. Also the reported thick neutron skin of ^{208}Pb , reported by the PREX experiment, appears to favor stiffer equation of state [295]. On the other hand, the equation of state, used in the analysis of flow systematics, did not consider momentum dependence, which might possibly result in softer EoS and symmetry energy. Further investigations are necessary.

In general, nuclear astrophysics appears to be important complement to the study of nucleus-nucleus collisions. It is desirable to perform as many comparisons as possible, ideally using fully compatible parameterizations of the equation of state.

5 Conclusions

As demonstrated in this work, the study of nucleus-nucleus collisions from the low to ultra-relativistic beam energies is a diverse field, allowing to address wide range of fundamental physics. In each region of beam energies, characteristic reaction mechanisms are observed and offer possibility to obtain information on the properties of nuclear matter under specific conditions, what allows to determine a global equation of the state and construct a global phase diagram of the strongly interacting nuclear matter. The extracted properties of the nuclear matter can be used for development of theoretical description of the nuclear matter and the underlying theory of the strong interaction, the quantum chromodynamics. The properties of the nuclear matter further allow to make conclusions on various aspects of the nuclear astrophysics and astro-particle physics, from the primordial nucleosynthesis through production of heavy nuclei, properties of neutron stars, supernova explosions, to the physics of the early Universe. The nucleus-nucleus collisions can be also used as a practical tool for production of very exotic neutron-rich nuclei, thus allowing to enter this yet completely unknown domain with the potential for further discoveries of new nuclear phenomena. Further progress in the field will depend on availability of the new experimental facilities with the capabilities greatly exceeding the capabilities of the presently existing experimental facilities. Construction of such facilities and full exploration of their capabilities will be the goal of the nuclear physics community in the upcoming decades.

Acknowledgement: This work was supported in part by the Slovak Scientific Grant Agency under contract 2/0105/11, and by the Slovak Research and Development Agency under contract APVV-0177-11. The author acknowledges fruitful discussions with G.A. Souliotis, Y.G. Ma, S. Kumar, M. Ploskon, K. Safarik, S. Dmitriev, V. Utyonkov, and S. Gmuca.

References

- [1] E. Rutherford, *Philosophical Magazine* **37** (1919) 581.
- [2] G.T. Seaborg and W.D. Loveland, *The elements beyond uranium*, Wiley-Interscience, 1990, ISBN13: 9780471890621.
- [3] V. V. Volkov, *Phys. Rep.* **44**, (1978) 93.
- [4] W. Reisdorf and H.G. Ritter, *Annu. Rev. Nucl. Part. Sci.* **47** (1997) 663; N. Hermann et al., *Annu. Rev. Nucl. Part. Sci.* **49** (1999) 581.
- [5] P. Braun-Munzinger and J. Stachel, *Annu. Rev. Nucl. Part. Sci.* **37** (1987) 97.
- [6] O. Kofoed-Hansen and K.O. Nielsen, *Phys. Rev.* **82** (1951) 96.
- [7] J.F. Liang et al., *Phys. Rev. Lett.* **91** (2003) 152701; Erratum *Phys. Rev. Lett.* **96** (2006) 029903.
- [8] D. Perez-Loureiro et al., *Phys. Lett. B* **703** (2011) 552.
- [9] J. Chadwick, *Nature* **129** (1932) 312; *Proc. Royal Society of London A* **136** (1932) 692.
- [10] J.D. Cockcroft, and E.T.S. Walton, *Proc. R. Soc. London A* **137** (1932) 229.
- [11] N. Bohr, *Nature (London)* **137** (1936) 344.
- [12] E. Fermi, E. Amaldi, O. D'Agostino, F. Rasetti, and E. Segre, *La Ricerca Scientifica* **5** (1934) 452.
- [13] O. Hahn and F. Strassman, *Naturwiss.* **27**, (1939) 1.
- [14] L. Meitner and O. R. Frisch, *Nature (London)* **143**, (1939) 416.
- [15] J.R. Oppenheimer and M. Phillips, *Phys. Rev.* **48** (1935) 500.
- [16] R. Bass, *Phys. Lett. B* **47** (1973) 139.
- [17] G. Wentzel, *Z. Phys.* **38** (1926) 518; H.A. Kramers, *Z. Phys.* **39** (1926) 828; L. Brillouin, *Comptes Rendus de l'Academie des Sciences* **183** (1926) 24.
- [18] Reisdorf, W., *Z. Phys. A* **300** (1981) 227.
- [19] J. Wilczynski, *Nucl. Phys. A* **216** (1973) 386.
- [20] W. Morawek et al., *Z. Phys. A* **341** (1991) 75.
- [21] K. Hagino, N. Rowley, M. Dasgupta, *Phys. Rev. C* **67** (2003) 054603.
- [22] C. Iliadis, *Nuclear Physics of Stars*, (Wiley-VCH, Weinheim, 2007) 666 pages, ISBN: 3527406026.
- [23] H. Bethe, *Phys. Rev.* **50** (1936) 332.
- [24] A.V. Ignatyuk, G.N. Smirenkin, and A.S. Tishin, *Yadernaya Fizika* **21** (1975) 485.
- [25] M. Veselsky et al., *Proc of 2nd international workshop on nuclear fission and fission-product spectroscopy*, Seyssins (France), 22-25 Apr 1998, *AIP Conference Proceedings* **447** (1998) 291.
- [26] S Cohen, F. Plasil, and W.J. Swiatecki, *Ann. Phys. (N.Y.)* **82** (1974) 557.
- [27] W.D. Myers and W.J. Swiatecki, *Ark. Fys.* **36** (1967) 343.
- [28] A.H. Wapstra, G. Audi, and R. Hoekstra, *Atomic Data and Nuclear Data Tables*, **39** (1989) 281.
- [29] A.J. Sierk, *Phys. Rev. C* **33** (1986) 2039.
- [30] A.N. Andreyev et al., *Nucl. Phys. A* **620** (1997) 229.
- [31] A.N. Andreyev et al., *Nucl. Phys. A* **626** (1997) 857.
- [32] L. Corradi et al., *Nucl. Phys. A* **701** (2002) 109c.
- [33] M. Veselsky and G.A. Souliotis, *Nucl. Phys. A* **872** (2011) 1.
- [34] L. Tassan-Got, PhD Thesis, 1988, Orsay, France, IPNO-T-89-02, 1989; L. Tassan-Got and C. Stefan, *Nucl. Phys. A* **524** (1991) 121.
- [35] J.P. Bondorf et al., *Phys. Rep.* **257** (1995) 133.
- [36] W. Krolas et al., *Nucl. Phys. A* **724** (2003) 289.

- [37] L. Corradi et al., Nucl. Phys. A **734** (2004) 237.
- [38] A.G. Artukh et al., Nucl. Phys. A **283** (1977) 350.
- [39] V.V. Volkov, Phys. Rep. **44** (1978) 93.
- [40] R. Bock et al., Nucl. Phys. A **388** (1982) 344.
- [41] M. Veselsky, Nucl. Phys. A **705** (2002) 193.
- [42] J. Randrup, Nucl. Phys. A **307** (1978) 319; Nucl. Phys. A **327** (1979) 490; Nucl. Phys. A **383** (1982) 468.
- [43] M. Veselsky et al., Phys. Rev. C **62** (2000) 064613.
- [44] G.A. Souliotis et al., Phys. Lett. B **543** (2002) 163.
- [45] R.E. Tribble, R.H. Burch and C.A. Gagliardi, Nucl. Instr. and Meth. A **285** (1989) 441; R.E. Tribble, C.A. Gagliardi and W. Liu, Nucl. Instr. and Meth. B **56/57** (1991) 956.
- [46] K. Summerer, B. Blank, Phys. Rev. C **61** (2000) 34607.
- [47] M. Veselsky, G.A. Souliotis, Nucl. Phys. A **765** (2006) 252.
- [48] G. Audi and A.H. Wapstra, Nucl. Phys. A **565** (1993) 1.
- [49] W.D. Myers and W.J. Swiatecki, Nucl. Phys. A **81** (1966) 1.
- [50] R. Charity et al., Nucl. Phys. A **483** (1988) 371.
- [51] G.A. Souliotis et al., Phys. Rev. Lett. **91** (2003) 022701.
- [52] G.A. Souliotis et al., Phys. Rev. C **84** (2011) 064607.
- [53] J.J. Griffin, Phys. Rev. Lett. **17** (1966) 478.
- [54] J. Randrup and R. Vandenbosch, Nucl. Phys. A **474** (1987) 219.
- [55] M. Veselsky et al., Z. Phys. A **356** (1997) 403.
- [56] M. Böhning, Nucl. Phys. A **152** (1970) 529.
- [57] H. Fuchs and K. Möhring, Rep. Prog. Phys. **57** (1994) 231.
- [58] C.K. Gelbke and D.H. Boal, Prog. Part. Nucl. Phys. **19** (1987) 33.
- [59] J. Gosset et al., Phys. Rev. C **16** (1977) 629.
- [60] R. Dayras et al., Nucl. Phys. A **460** (1986) 299.
- [61] A.Y. Abul-Magd, Z. Phys. A **298** (1980) 143.
- [62] B.G. Harvey and M.J. Murphy, Phys. Lett. B **130** (1983) 373.
- [63] W.A. Friedman, Phys. Rev. C **27** (1983) 569.
- [64] J.-J. Gaimard and K.-H. Schmidt, Nucl. Phys. A **531** (1991) 709.
- [65] N. Matsuoka et al., Nucl. Phys. A **311** (1978) 173.
- [66] W. Hauser and H. Feshbach, Phys. Rev. **87** (1952) 366.
- [67] L.G. Moretto, Nucl. Phys. A **247** (1975) 211.
- [68] M. Veselsky et al., Nucl. Phys. A **724** (2003) 431.
- [69] K.A. Hanold et al., Phys. Rev. C **52** (1995) 1462.
- [70] B.M. Sherill et al., Nucl. Instr. and Meth. B **56/57** (1991) 1106.
- [71] M. Veselsky and G.A. Souliotis, Nucl. Phys. A **781** (2007) 521.
- [72] G. Casini et al., Phys. Rev. Lett. **71** (1993) 2567; C.P. Montoya et al., Phys. Rev. Lett. **73** (1994) 3070.
- [73] U. Brosa et al., Phys. Rep. **197** (1990) 167.
- [74] M. Veselsky et al., Nucl. Phys. A **837** (2010) 163.
- [75] R. Pfaff et al., Phys. Rev. C **51** (1995) 1348.
- [76] R. Pfaff et al., Phys. Rev. C **53** (1996) 1753.

- [77] T. Kubo et al., Nucl. Instr. and Meth. B **70** (1992) 309.
- [78] M. Veselsky et al., Phys. Rev. C **62** (2000) 064613.
- [79] M. Di Toro, A. Olmi and R. Roy, Eur. Phys. J. A **30** (2006) 65.
- [80] M. Jandel et al., Journal of Phys. G **31** (2005) 29.
- [81] G.A. Souliotis et al., Nucl. Instr. Meth. B **204** (2003) 166.
- [82] J. Feng et al., Phys. Rev. C **50** (1994) 2420.
- [83] M. Mocko et al., Phys. Rev. C **76** (2007) 014609.
- [84] M. Veselsky and G.A. Souliotis, Nucl. Phys. A **834** (2010) 577c.
- [85] M. Papa et al., Phys. Rev. C **64** (2001) 024612; M. Papa, T. Maruyama and A. Bonasera, J. Comput. Phys. **208** (2005) **403**.
- [86] F. Amorini et al., Phys. Rev. Lett. **102** (2009), 112701.
- [87] G.A. Souliotis, J. Phys. Conf. Series **205** (2010) 012019.
- [88] K.-H. Schmidt et al., Phys. Lett. B **300** (1993) 313.
- [89] A.R. Junghans et al., Nucl. Phys. A **629** (1998) 635.
- [90] J. Benlliure, A. Grewe, M. de Jong, K.-H. Schmidt and S. Zhdanov, Nucl. Phys. A **628** (1998) 458.
- [91] B. Jurado, K.-H. Schmidt and J. Benlliure, Phys. Lett. B **533** (2003) 186.
- [92] K.-H. Schmidt, M. V. Ricciardi, A. Botvina and T. Enqvist, Nucl. Phys. A **710** (2002) 157.
- [93] A. Kelic, M.V. Ricciardi and K.-H. Schmidt, Proceedings of the Joint ICTP-IAEA Advanced Workshop on Model Codes for Spallation Reactions, ICTP Trieste, Italy, 4-8 February 2008. Editors: D. Filges, S. Leray, Y. Yariv, A. Mengoni, A. Stanculescu and G. Mank, IAEA INDC(NDS)-530, pag. 181-221, Vienna, August 2008; arXiv:nucl-th/0906.4193 and references therein.
- [94] K. Helariutta, J. Benlliure, M. V. Ricciardi and K.-H. Schmidt, Eur. Phys. J. A **17** (2003) 181.
- [95] Y. Yariv and Z. Fraenkel, Phys. Rev. C **24** (1981) 488.
- [96] M.P. Guthrie, R.G. Alsmiller and H.W. Bertini, Nucl. Instrum. Meth. **66** (1968) 29; H.W. Bertini and M.P. Guthrie, Nucl. Phys. A **169** (1971) 670.
- [97] C. Donzaud et al., Nucl. Phys. A **593** (1995) 503.
- [98] S. Agostinelli et al., Geant4 - a simulation toolkit, Nucl. Instrum. Meth. A **506** (2003) 250.
- [99] MARS Code System, <http://www-ap.fnl.gov/MARS>.
- [100] MCNP Code, <http://mcnp.lanl.gov/>.
- [101] G.F. Bertsch, H. Kruse and S. Das Gupta, Phys. Rev. C **29** (1984) 673.
- [102] H. Kruse, B. V. Jacak and H. Stöcker, Phys. Rev. Lett. **54** (1985) 289.
- [103] C.Y. Wong, Phys. Rev. C **25** (1982) 1461.
- [104] J. Cugnon, T. Mizutani and J. Vandermeulen, Nucl. Phys. A **352** (1981) 505.
- [105] W. Reisdorf et al., Phys. Rev. Lett. **92** (2004) 232301.
- [106] P. Salabura et al., Nucl. Phys. B **44** (1995) 701.
- [107] U. Heinz, arXiv:hep-ph/0407360.
- [108] A. Andronic and P. Braun-Munzinger, arXiv:hep-ph/0402291.
- [109] P. Braun-Munzinger and J. Stachel, Nature **448** (2007) 302.
- [110] J.D. Bjorken, Phys. Rev. D **27** (1983) 140.
- [111] B. Muller, J. Schukraft and B. Wyslouch, arXiv:1202.3233 [hep-ex].
- [112] F. Karsch, Lect. Notes Phys. **583** (2002) 209 [hep-lat/0106019]; F. Karsch and E. Laermann, hep-lat/0305025; E. Laermann and O. Philipsen, hep-ph/0303042.
- [113] B.I. Abelev et al. (The STAR Collaboration), Nature **473** (2011) 353.

- [114] B.I. Abelev et al. (The STAR Collaboration), *Science* **328** (2010) 58.
- [115] K. Safarik, private communication.
- [116] H.H. Heckman, D.E. Greiner, P.J. Lindstrom and F.S. Bieser, *Phys. Rev. Lett.* **28** (1972) 926.
- [117] C. Villagrasa-Canton, PhD thesis (Universite de Paris XI, France, December 2003).
- [118] P. Napolitani et al., *Phys. Rev. C* **70** (2004) 054607.
- [119] P. Napolitani, PhD thesis (Universite de Paris XI, France, September 2004)
- [120] J. Taieb et al., *Nucl. Phys. A* **724** (2003) 413.
- [121] M. Bernas et al., *Nucl. Phys. A* **725** (2003) 213.
- [122] M.V. Ricciardi et al., *Phys. Rev. C* **73** (2006) 014607.
- [123] P. Armbruster et al., *Phys. Rev. Lett.* **93** (2004) 212701.
- [124] M. Bernas et al., *Nucl. Phys. A* **725** (2003) 213.
- [125] K.-H. Schmidt, A. Keli, S. Luki, M. V. Ricciardi and M. Veselsky, *Phys. Rev. ST Accel. Beams* **10** (2007) 014701.
- [126] EURISOL Feasibility Study RTD, [http : //www.ganil.fr/eurisol/Final_Report.html](http://www.ganil.fr/eurisol/Final_Report.html).
- [127] [http : //www - w2k.gsi.de/charms/amadeus.htm](http://www-w2k.gsi.de/charms/amadeus.htm).
- [128] A. Stolz et al., *Nucl. Phys. A* **746** (2004) 54c.
- [129] O.V. Lozhkin and W. Trautmann, *Phys. Rev. C* **46** (1992) 1996.
- [130] A.S. Botvina et al., *Phys. Rev. C* **65** (2002) 044610.
- [131] M.B. Tsang et al., *Phys. Rev. Lett.* **86** (2001) 5023.
- [132] G.A. Souliotis et al., *Phys. Rev. C* **68** (2003) 024605.
- [133] M. Veselsky, G.A. Souliotis and M. Jandel, *Phys. Rev. C* **69** (2004) 044607.
- [134] G. Savard et al., *Nucl. Instr. Meth. B* **204** (2003) 582.
- [135] G. Bollen et al., *Nucl. Instr. Meth. A* **550** (2005) 27.
- [136] G.A. Souliotis et al., *Nucl. Instr. Meth. B* **266** (2008) 4692.
- [137] S. Hofmann and G. Munzenberg, *Reviews of Modern Physics* **72** (2000) 733.
- [138] P. Armbruster, *Annual Review of Nuclear and Particle Science* **50** (2000) 411.
- [139] A.N. Andreyev et al., *Z. Phys. A* **344** (1992) 225; A.N. Andreyev et al., *Z. Phys. A* **345** (1993) 389; Yu.A. Lazarev et al., *Phys. Rev. Lett.* **75** (1995) 1903; Yu.A. Lazarev et al., *Phys. Rev. C* **54** (1996) 620.
- [140] M. Veselsky, *Acta Physica Slovaca* **49** (1999) 101.
- [141] W. Reisdorf, *Z. Phys. A* **300** (1981) 227.
- [142] P. Moller, J. R. Nix, W. D. Myers and W. J. Swiatecki, *At. Data and Nucl. Data Tab.* **59** (1995) 185.
- [143] R. Bass, *Lect. Notes on Phys.* **117** (1980) 281.
- [144] W. Reisdorf et al., *Nucl. Phys. A* **444** (1985) 154.
- [145] H.-W. Gaggeler et al., *Nucl. Phys. A* **502** (1989) 561c; S. Hofmann, GSI-Preprint-98-16, GSI Darmstadt, 1998.
- [146] D.Vermeulen et al., *Z. Phys. A* **318** (1984) 157.
- [147] S.M. Lukyanov et al., *Proc. Int. School of Heavy Ion Phys., Dubna, 3-12 Oct 1989, JINR Dubna, 1990, p.225*; D. Hilscher et al., *Phys. of At. Nucl.* **57** (1994) 1187.
- [148] M.G. Itkis et al., *Yad. Fiz.* **66** (2003) 1154; *Phys. Atomic Nuclei* **66** (2003) 1118.
- [149] M. Veselsky, *Phys. Atom. Nucl.* **66** (2003) 1086; *Yad. Fiz.* **66** (2003) 1122.
- [150] M. Samyn, S. Goriely and J.M. Pearson, *Nucl. Phys. A* **718** (2003) 653; M. Samyn et al., *Phys. Rev. C* **70** (2004) 044309.

- [151] Yu.Ts. Oganessian et al., Phys. Rev. C **70** (2004) 064609; Erratum Phys. Rev. C **71** (2005) 029902.
- [152] Yu.Ts. Oganessian et al., Phys. Rev. C **69** (2004) 054607.
- [153] Yu.Ts. Oganessian et al., Phys. Rev. C **74** (2006) 044602.
- [154] Yu.Ts. Oganessian et al., Phys. Rev. C **76** (2007) 011601.
- [155] Yu.Ts. Oganessian et al., Phys. Rev. C **87** (2013) 014302.
- [156] Yu.Ts. Oganessian et al., Phys. Rev. Lett. **109** (2012) 162501.
- [157] Yu.Ts. Oganessian et al., Phys. Rev. C **87** (2013) 054621.
- [158] G.G. Adamian, N.V. Antonenko and W. Scheid, Nucl. Phys. A **618** (1997) 176; G.G. Adamian, N.V. Antonenko, W. Scheid and V.V. Volkov, Nucl. Phys. A **627** (1997) 361; Nucl. Phys. A **633** (1998) 409.
- [159] V. Zagrebaev and W. Greiner, J. Phys. G **31** (2005) 825; J. Phys. G **34** (2007) 1; J. Phys. G **34** (2007) 2265.
- [160] N.K. Glendenning, *Compact stars*, 2nd edition, Springer-Verlag, (2000).
- [161] F. Weber, *Pulsars as Astrophysical Laboratories for Nuclear and Particle Physics*, IOP Publishing (1999).
- [162] J.D. Walecka, *Theoretical Nuclear and Subnuclear Physics*, Oxford University Press (1995).
- [163] J.M. Lattimer and M. Prakash, Phys. Rep. **442** (2007) 109.
- [164] P. Danielewicz, R. Lacey and W.G. Lynch, Science **298** (2002) 1592.
- [165] D.H. Youngblood, H.L. Clark and Y.-W. Lui, Phys. Rev. Lett. **82** (1999) 691.
- [166] A. Andronic et al., Eur. Phys. J. A **30** (2006) 31.
- [167] C. Sturm et al. Phys. Rev. Lett. **86** (2001) 39.
- [168] C. Fuchs, Prog. Part. Nucl. Phys. **56** (2006) 1.
- [169] G. Colo et al., Phys. Rev. C **70** (2004) 024307.
- [170] J. Piekarewicz, Phys. Rev. C **69** (2004) 041301.
- [171] S. Albergo et al., Nuovo Cimento **89** (1995) 1.
- [172] J. Randrup and S.E. Koonin, Nucl. Phys. A **356** (1981) 223.
- [173] M. Veselsky, G.A. Souliotis and S.J. Yennello, Proc. 5th Int. Conf. DANF-2001, Casta-Papiernicka, Slovakia, 2001, World Scientific, 2002, p. 461; E-print: arXiv.org:nucl-ex/0112007.
- [174] A. Schuttauf et al., Nucl. Phys. A **607** (1996) 457.
- [175] J.A. Hauger et al., Phys. Rev. Lett. **77** (1995) 235; H. Xi et al., Z. Phys. A **359** (1997) 397; A. Ruangma et al., Phys. Rev. C **66** (2002) 044603.
- [176] M. Veselsky et al., Phys. Lett. B **497** (2001) 1.
- [177] M. Veselsky et al., Phys. Rev. C **62** (2000) 041605(R).
- [178] M.A. McMahan et al., Phys. Rev. Lett. **54** (1985) 1995.
- [179] M. Veselsky et al., Nucl. Phys. A **724** (2003) 431.
- [180] J.A. Lopez and J. Randrup, Nucl. Phys. A **503** (1989) 183.
- [181] P. Kreutz et al., Nucl. Phys. A **556** (1993) 672.
- [182] D.H.E. Gross, Phys. Rep. **279** (1997) 119.
- [183] Terrell L. Hill, Thermodynamics of small systems, W.A. Benjamin Publishers, New York, Amsterdam, 1963.
- [184] J.W. Negele, Rev. Mod. Phys. **54** (1992) 913.
- [185] H. Kruse, B.V. Jacak and H. Stoecker, Phys. Rev. Lett. **54** (1985) 289; J. Molitoris and H. Stoecker, Phys. Rev. C **32** (1985) 346; J. Molitoris, H. Stoecker and B. Winer, Phys. Rev. C **36** (1987) 220.
- [186] G. Bertsch and S. Gupta, Phys. Rep. **160** (1988) 189; W. Cassing et al., Phys. Rep. **188** (1990) 363.

- [187] C. Gregoire et al., Nucl. Phys. A **465** (1987) 317; Nucl. Phys. A **471** (1987) 399c; P. Schuck et al., Prog. Part. Nucl. Phys. **22** (1990) 181.
- [188] A. Bonasera et al., Phys. Rep. **243** (1994) 1.
- [189] J. Aichelin, Phys. Rep. **202** (1991) 233.
- [190] G. Sauer, H. Chandra and U. Mosel, Nucl. Phys. A **264** (1976) 221.
- [191] H. Müller and B.D. Serot, Phys. Rev. C **52** (1995) 2072.
- [192] P.J. Siemens, Nature **305** (1983) 410.
- [193] V.M. Kolomietz et al., Phys. Rev. C **64** (2001) 024315.
- [194] B.-A. Li and C. Ko, Nucl. Phys. A **618** (1997) 498; V. Baran et al., Phys. Rev. Lett. **86** (2001) 4492; M. Colonna et al., Phys. Rev. Lett. **88** (2002) 122701; J. Marqueron and P. Chomaz, Phys. Rev. C **67** (2003) 41602(R).
- [195] M.E. Fisher, Physics **3** (1967) 255.
- [196] J. Richert, P. Wagner, Phys. Rep. **350** (2001) 1.
- [197] K.A. Bugaev et al., Phys. Rev. C **62** (2000) 044320; Phys. Lett. B **498** (2001) 144; P.T. Reuter and K.A. Bugaev, Phys. Lett. B **517** (2001) 233.
- [198] J.M. Hammersley, Proc. of 87th Intern. Colloq. CNRS, Paris, 1957. P.17.
- [199] M. Veselsky, G.A. Souliotis and S.J. Yennello, Phys. Rev. C **69** (2004) 031602(R).
- [200] M. Veselsky and S.J. Yennello, Nucl. Phys. A **749** (2005) 114c.
- [201] M. D'Agostino et al., Nucl. Phys. A **650** (1999) 329.
- [202] B. Borderie et al., Phys. Rev. Lett. **86** (2001) 3252.
- [203] Y.G. Ma et al., Physical Review C **69** (2004) 064610.
- [204] M. Jandel et al., Phys. Rev. C **74** (2006) 054608.
- [205] M. Veselsky, Int. Journal of Modern Physics E **17** (2008) 1883, E-print: arXiv.org:nucl-th/0703077.
- [206] J.M. Lattimer and M. Prakash, Phys. Rep. **333** (2000) 121.
- [207] J.M. Lattimer and M. Prakash, Ap. J. **550** (2001) 426.
- [208] J.M. Lattimer and M. Prakash, Science **304** (2004) 536.
- [209] B.-A. Li et al., Phys. Rep. **464** (2008) 113.
- [210] J.B. Natowitz *et al.*, Phys. Rev. Lett. **89** (2002) 212701.
- [211] W. Reisdorf *et al.*, Nucl. Phys. A **876** (2012) 1.
- [212] M.B. Tsang *et al.*, Phys. Rev. Lett. **92** (2004) 062701.
- [213] M.A. Famiano *et al.*, Phys. Rev. Lett. **97** (2006) 052701.
- [214] M.B. Tsang *et al.*, Phys. Rev. Lett. **102** (2009) 122701.
- [215] S. Kumar *et al.*, Phys. Rev. C **84** (2011) 044620.
- [216] Z. Xiao, B.-A. Li, L.-W. Chen, G.-C. Yong and M. Zhang, Phys. Rev. Lett. **102** (2009) 062502.
- [217] P. Russotto *et al.*, Phys. Lett. B **697** (2011) 471.
- [218] M.D. Cozma, Phys. Lett. B **700** (2011) 139.
- [219] S. Gautam *et al.*, Phys. Rev. C **83** (2011) 034606.
- [220] T. Li et al., Phys. Rev. Lett. **99** (2007) 162503.
- [221] A. Klimkiewicz et al, Phys. Rev. C **76** (2007) 051603.
- [222] F. Amorini et al., Phys. Rev. Lett. **102** (2009) 112701.
- [223] M.B. Tsang et al., Phys. Rev. Lett. **86** (2001) 5023.
- [224] J. Iglio et al., Phys. Rev. C **74** (2006) 024605.

- [225] B.-A. Li, Phys. Rev. Lett. **85** (2000) 4221.
- [226] B.-A. Li et al., Phys. Rev. C **64** (2001) 054604.
- [227] B.-A. Li, Phys. Rev. Lett. **88** (2002) 192701.
- [228] G.-C. Yong et al., Phys. Rev. C **74** (2006) 064617.
- [229] V. Greco et al., Phys. Lett. B **562** (2003) 215.
- [230] B.-A. Li et al., Phys. Rev. Lett. **78** (1997) 1644.
- [231] B.-A. Li et al., Phys. Lett. B **634** (2006) 378.
- [232] Q. Li et al., Phys. Rev. C **73**, 051601(R) (2006) .
- [233] Q. Li et al., Phys. Rev. C **71** (2005) 054907.
- [234] G.-C. Yong et al., Phys. Rev. C **73** (2006) 034603.
- [235] G. Ferini, et al., Phys. Rev. Lett. **97** (2006) 202301.
- [236] X. Lopez, et al., Phys. Rev. C **75** (2007) 011901.
- [237] W. Reisdorf et al., Nucl. Phys. A **781** (2007) 459.
- [238] M. Zhang et al., Phys. Rev. C **80** (2009) 034616.
- [239] V. Greco et al., arXiv:0911.4610.
- [240] Jun Xu, Che Ming Ko and Yongseok Oh, arXiv:0906.1602.
- [241] G.Q. Li and R. Machleidt, Phys. Rev. C **48** (1993) 1702; Phys. Rev. C **49** (1994) 566.
- [242] T. Alm, G. Ropke and M. Schmidt, Phys. Rev. C **50** (1994) 31; T. Alm, G. Ropke, W. Bauer, F. Daffin and M. Schmidt, Nucl. Phys. A **587** (1995) 815.
- [243] B.A. Li and L. W. Chen, Phys. Rev. C **72** (2005) 064611.
- [244] D. Klakow, G. Welke and W. Bauer, Phys. Rev. C **48** (1993) 1982.
- [245] M. Veselsky and Y.G. Ma, Phys. Rev. C **87** (2013) 034615.
- [246] W. Cassing and U. Mosel, Prog. Part. Nucl. Phys. **25** (1990) 235.
- [247] W. Cassing, K. Niita and S.J. Wang, Z. Phys. A **331** (1988) 439.
- [248] N. Herrmann, J. P. Wessels and T. Wienold, Ann. Rev. Nucl. Part. Sci. **49** (1999) 581.
- [249] A. Andronic, J. Lukasik, W. Reisdorf and W. Trautmann, Eur. Phys. J. **30** (2006) 31.
- [250] F. Wilczek, hep-ph/0003183; D.E. Kharzeev and J. Raufeisen, nucl-th/0206073.
- [251] See e.g. H. Satz, Nucl. Phys. A **715** (2003) 3 [hep-ph/0209181] and ref. therein.
- [252] H. Satz, Rep. Prog. Phys. **63** (2000) 1511 [hep-ph/0007069].
- [253] I.Ya. Pomeranchuk, Dokl. Akad. Nauk. SSSR **78** (1951) 889.
- [254] R. Hagedorn, Nuovo Cim. Suppl. **3** (1965) 147; see also: T. Ericson and J. Rafelski, CERN Courier **43**, Nr.7 (2003) 30.
- [255] D.J. Gross and F. Wilczek, Phys. Rev. Lett. **30** (1973) 1343; H.D. Politzer, Phys. Rev. Lett. **30** (1973) 1346.
- [256] E.V. Shuryak, Phys. Lett. B **78** (1978) 150.
- [257] E.S. Bowman and J.I. Kapusta, Physical Review C **79** (2009) 015202.
- [258] L. McLerran and R.D. Pisarski, Nucl. Phys. A **796** (2007) 83.
- [259] M. Alford, K. Rajagopal, T. Schafer and A. Schmitt, Reviews of Modern Physics **80** (2008) 1455; arXiv:0709.4635.
- [260] J. Cleymans, R.V. Gavai and E. Suhonen, Phys. Rep. **130** (1986) 217.
- [261] K. Kajantie and L. McLerran, Annu. Rev. Nucl. Part. Sci. **37** (1987) 293; J.W. Harris and B. Müller, Annu. Rev. Nucl. Part. Sci. **46** (1996) 71 [hep-ph/9602235]; S.A. Bass, M. Gyulassy, H. Stöcker and W. Greiner, J. Phys. G **25** (1999) R1 [hep-ph/9810281].

- [262] T. Peitzmann and M.H. Thoma, Phys. Rep. **364** (2002) 175 [hep-ph/0111114].
- [263] R. Rapp and J. Wambach, Adv. Nucl. Phys. **25** (2000) 1 [hep-ph/9909229]; J.P. Wessels et al. (CERES), Nucl. Phys. A **715** (2003) 262c [nucl-ex/0212015] and ref. therein.
- [264] J. Rafelski and J. Letessier, J. Phys. G **30** (2004) S1 [hep-ph/0305284]; R. Stock, hep-ph/0312039.
- [265] S.S. Adler et al. (PHENIX), Phys. Rev. Lett. **91** (2003) 072301 [nucl-ex/0304022], Phys. Rev. Lett. **91** (2003) 072303 [nucl-ex/0306021], nucl-ex/0308006; J. Adams et al. (STAR), Phys. Rev. Lett. **91** (2003) 172302 [nucl-ex/0305015], Phys. Rev. Lett. **91** (2003) 072304 [nucl-ex/0306024]; B.B. Back et al. (PHOBOS), Phys. Rev. Lett. **91** (2003) 072302 [nucl-ex/0306025]; I. Arsene et al. (BRAHMS), Phys. Rev. Lett. **91** (2003) 072305 [nucl-ex/0307003]; G. Agakichiev et al. (CERES), Phys. Rev. Lett. **92** (2004) 032301 [nucl-ex/0303014].
- [266] D. Adamova et al. (CERES), Nucl. Phys. A **727** (2003) 97 [nucl-ex/0305002] and ref. therein.
- [267] M. Asakawa, U. Heinz and B. Müller, Phys. Rev. Lett. **85** (2000) 2072 [hep-ph/0003169]; S. Jeon and V. Koch, Phys. Rev. Lett. **85** (2000) 2076 [hep-ph/0003168]; for a review, see: S. Jeon and V. Koch, hep-ph/0304012.
- [268] K. Adcox et al. (PHENIX Collaboration), Phys. Rev. Lett. **88** (2002) 022301.
- [269] C. Adler et al. (STAR Collaboration), Phys. Rev. Lett. **90** (2002) 082302.
- [270] G. Aad et al., Phys. Rev. Lett. **105** (2010) 252303.
- [271] K.H. Ackermann et al. (STAR Collaboration), Phys. Rev. Lett. **86** (2001) 402.
- [272] P. Huovinen, in R. C. Hwa and X.-N. Wang (eds.), Quark-Gluon Plasma 3, (World Scientific, Singapore, 2003), 600; arXiv:nucl-th/0305064.
- [273] T.A. Trainor, arXiv:1303.4774v1 [hep-ph].
- [274] L. McLerran, Lect. Notes Phys. **583** (2002) 291.
- [275] D. Kharzeev and M. Nardi, Phys. Lett. B **507** (2001) 121.
- [276] E. Shuryak, arXiv:1112.2573 [hep-ph].
- [277] A. Hewish, S. J. Bell, J. D. H. Pilkington and R. A. Collins, Nature, **217** (1968) 709.
- [278] V.M. Kaspi, Proc. Nat. Acad. Sci. USA **107** (2010) 7147.
- [279] P. Haensel, A.Y. Potekhin and D.G. Yakovlev, Neutron Stars 1: Equation of State and Structure, Springer, 2006.
- [280] J.M. Lattimer, Annu. Rev. Nucl. Part. Sci. **62** (2012) 485.
- [281] N. Andersson et al. Gen. Rel. Grav. **43** (2011) 409.
- [282] A. Bauswein, H.-T. Janka, Phys. Rev. Lett. **108** (2012) 011101.
- [283] A. Bauswein, H.-T. Janka, K. Hebeler and A. Schwenk, Phys. Rev. D **86** (2012) 063001.
- [284] B.D. Lackey, K. Kyutoku, M. Shibata, P.R. Brady and J.L. Friedman, Phys. Rev. D **85** (2012) 044061.
- [285] A.W. Steiner, Phys. Rev. C **77** (2008) 035805.
- [286] B.G. Todd-Rutel and J. Piekarewicz, Phys. Rev. Lett. **95** (2005) 122501.
- [287] A.W. Steiner et al., Phys. Rep. **411** (2005) 325.
- [288] C.J. Horowitz and J. Piekarewicz, Phys. Rev. Lett. **86** (2001) 5647.
- [289] S. Abrahamyan et al., Phys. Rev. Lett. **108** (2012) 112502.
- [290] C. Horowitz et al., Phys. Rev. C **85** (2012) 032501.
- [291] K. Hebeler, J.M. Lattimer, C.J. Pethick and A. Schwenk, arXiv:1303.4662 [astro-ph.SR].
- [292] P.B. Demorest et al., Nature **467** (2010) 1081.
- [293] M.H. van Kerkwijk et al., Astrophys. J. **728** (2011) 95.
- [294] V. Suleimanov, J. Poutanen, M. Revnivtsev and K. Werner, Astrophys. J. **742** (2011) 122.
- [295] F.J. Fattoyev and J. Piekarewicz, arXiv:1306.6034 [nucl-th].



Martin Veselský, born in Bratislava, Slovakia, in 1966, received his PhD from Comenius University in Bratislava in 1997. During his PhD studies he spent one year at each the Flerov Laboratory of Nuclear Reactions in Dubna, Russia, and the Gesellschaft für Schwerionenforschung (GSI) in Darmstadt, Germany. Since 1996 he proceeded with his scientific work at the Institute of Physics of Slovak Academy of Sciences in Bratislava. Between 1999 and 2002 he spent three years as a post-doctoral fellow at the Cyclotron Institute of the Texas A&M University. In 2012 he stayed as a visiting professor at the Shanghai Institute of Applied Physics in Shanghai, China. His research has concentrated on various aspects of nuclear reactions, such as production of exotic and super-heavy nuclei via complete fusion reactions, production of neutron-rich nuclei using reactions of nucleon exchange, study of reaction mechanisms in the Fermi energy domain, study of multifragmentation and liquid-gas phase transition in nuclear matter, and study of nuclear equation of state and symmetry energy in relativistic nucleus-nucleus collisions.